THESIS

CONSTRAINING MARINE ICE NUCLEATING PARTICLE PARAMETERIZATIONS IN ATMOSPHERIC MODELS USING OBSERVATIONS FROM THE SOUTHERN OCEAN

Submitted by

Kathryn A. Moore

Department of Atmospheric Science

In partial fulfillment of the requirements

For the Degree of Master of Science

Colorado State University

Fort Collins, Colorado

Spring 2020

Master's Committee:

Advisor: Sonia Kreidenweis
Co-Advisor: Paul DeMott

Delphine Farmer
Jeffrey Pierce

Copyright by Kathryn A. Moore 2020

All Rights Reserved

ABSTRACT

CONSTRAINING MARINE ICE NUCLEATING PARTICLE PARAMETERIZATIONS IN ATMOSPHERIC MODELS USING OBSERVATIONS FROM THE SOUTHERN OCEAN

The limited anthropogenic and terrestrial aerosol sources impacting the Southern Ocean (SO) make it a unique site to study the production of primary sea spray aerosols (SSA) and their role in modifying cloud properties. Previous observations of low ice nucleating particle (INP) concentrations and recent modeling work support the idea that the SO INP population is dominated by SSA. These marine INPs are hypothesized to strongly influence the lifetime, formation, and optical properties of the supercooled and mixed phase clouds that are common in the region, though direct observational evidence for this is lacking. This study focuses on improving our understanding of INP emissions in the marine boundary layer over the SO, with applicability to other ocean regions, and to provide in situ measurements with which to validate and improve INP parameterizations in global and cloud resolving models. Measurements of INPs and aerosols in the marine boundary layer were made during the Clouds, Aerosols, Precipitation Radiation and atmospherIc Composition Over the southeRN ocean 2 (CAPRICORN-2) study on the R/V Investigator during Jan. - March 2018. An initial focus of this thesis was on increasing speed and reproducibility of processing online INP measurements, as well as improving the determination of statistical significance and uncertainty bounds. Different approaches to parameterizing INPs in models are explored for SO aerosols, including the use of aerosol surface area and number concentrations. With an eye towards augmenting global datasets of INPs, a comparison of particle surface area measurements from four different techniques is presented, for use in developing and testing INP parameterizations for different sources and atmospheric conditions. Surface area concentrations derived from Wideband Integrated Bioaerosol Sensor (WIBS) and nephelometer observations are strongly correlated with direct particle size distribution measurements, and can be used in their stead. Uncertainty bounds for both techniques

and a scaling factor for WIBS measurements are provided to aid in these estimates. INP concentrations observed during CAPRICORN-2 are very low across the entire temperature range measured (to -30 °C), even compared to previous measurements of marine-dominated airmasses. Unlike INPs from other sources, Southern Ocean marine INPs appear most correlated with accumulation, rather than coarse mode, particles, and are dominated by submicron particles. Commonly used relationships between coarse mode particle number and total aerosol surface area show no significant correlation with SO INP concentrations, indicating a different functional form or different independent variable may be needed to accurately parameterize marine INPs in models.

ACKNOWLEDGEMENTS

I would like to thank Drs. Sonia Kreidenweis and Paul DeMott for their patience, guidance, and support throughout my M.S., and to all the members of our lab for scientific discussions and emergency field assistance at all hours of the day. This research was supported through an NSF Graduate Research Fellowship, and under NSF award 1660486 (SOCRATES and CAPRICORN-2) and DOE contracts DE-SC0018929 and DOE-ARM Battelle Memorial Institute Contract #339591 (MICRE and MARCUS).

TABLE OF CONTENTS

LIST OF TABLES

LIST OF FIGURES

1. Introduction

1.1 SOUTHERN OCEAN CLOUDS AND CLIMATE

The Southern Ocean (SO) is a remote and stormy region that encircles the Antarctic continent, with highly productive ecosystems in Austral summer. Strong surface westerlies occur at all seasons, and the resulting wind stress is important for driving the Antarctic Circumpolar Current (ACC) and upwelling of warm and nutrient-rich Circumpolar Deep Water along the Antarctic Polar Front, supporting the Southern Ocean food chain (Rintoul 2007). Deep water formation in the Weddell Sea, Ross Sea, and Mertz Polynya contributes to the ventilation of the deep ocean, as well as being an integral part of the global ocean thermohaline circulation (Rintoul 2007). This circulation is the dominant mechanism responsible for oceanic heat transport, and therefore influences climate and atmospheric circulation on a global scale. Its remoteness from continental and anthropogenic aerosol sources means the Southern Ocean is a unique site to study aerosol-cloud interactions in a region dominated by marine aerosols.

Factors that influence the cloud-forming properties of aerosols in marine environments such as the SO are still not well understood (Carslaw et al. 2010; Quinn and Bates 2011). Aerosols contribute the largest uncertainty to global radiative forcing estimates, with natural aerosols responsible for a significant portion of this (Carslaw et al. 2013; Andreae 2007). As the natural aerosol burden and its effects are largely unknown, our ability to constrain and predict the influence of anthropogenic aerosols on climate sensitivity (Kiehl 2007), radiative forcing, and cloud processes (Andreae 2007) has been hindered (Carslaw et al. 2013). Climate models suggest only weak influences of anthropogenic aerosols on the SO region, so it may serve as a proxy for preindustrial aerosol conditions (Hamilton et al. 2014), and a good location to test aerosol-cloud interactions in models.

Satellite observations suggest low level clouds with tops below 3 km dominate over the SO, and are rarely glaciated at cloud top, even down to temperatures of -25 °C (Morrison et al. 2011;

Huang et al. 2012). Multiple cloud layers are often observed, and assignment of cloud phase below cloud top is highly uncertain (Mace 2010), though satellite retrievals suggest a greater occurrence of mixed phase clouds containing supercooled liquid water (SLW) over the SO than at equivalent latitudes in the Northern Hemisphere (Morrison et al. 2011; Chubb et al. 2013). Limited *in situ* observations also indicate more frequent drizzle and less ice in the Southern Ocean compared to Arctic supercooled and mixed-phase clouds (Chubb et al. 2013). Despite these and other observed differences between SO and Northern Hemisphere clouds, almost all model parameterizations have been developed with Northern Hemisphere data due to the lack of direct observations over the SO (Bromwich et al. 2012).

Global climate model (GCM) simulations and satellite observations of SO clouds show poor agreement, including a systematic positive bias in model estimates of absorbed shortwave radiation poleward of 55 °S (Figure 1.1), particularly during Austral summer (Trenberth and Fasullo 2010). Underestimation in the number and lifetime of supercooled clouds, particularly low and midlevel clouds in the cold sector of cyclonic storms, appears to account for the bulk of this overestimation (Bodas-Salcedo et al. 2013). This radiation bias subsequently induces warm biases in sea surface temperature (SST) year-round, and leads to associated errors and uncertainties in predicting other model outcomes, such as the position of the Southern Hemisphere jet (Ceppi et al. 2012; 2014) and climate sensitivity (Trenberth and Fasullo 2010; Tan et al. 2016). The SO influences oceanic and atmospheric circulation on both local and global scales, and the poor representation of SO atmospheric processes in GCM simulations is a major limitation on our ability to accurately predict responses to future climate change.

Several hypotheses have been proposed to contribute to the large radiation biases observed in climate models of the SO region, which include (Marchand et al. 2014):

1. Deficiencies in model turbulent transport
2. Interaction between parameterized cumulus and stratiform clouds
3. Microphysical deficiencies in models

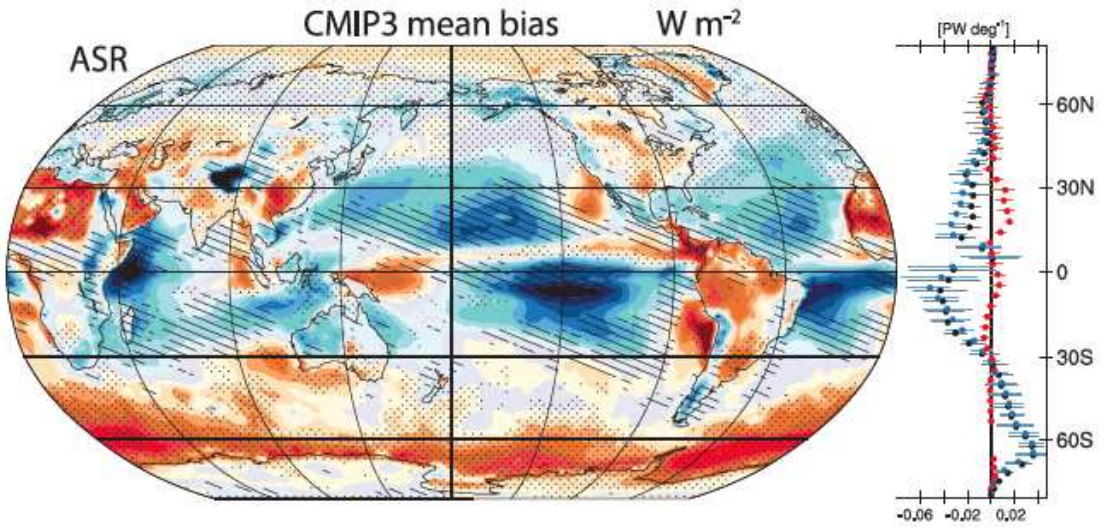

Figure 1.1: Mean CMIP3 biases in modeled absorbed shortwave radiation relative to satellite observations (Trenberth and Fasullo 2010).

4. Low resolution of circulation systems

Only item 3 will be considered in this thesis, although improving all of these processes is important for reconciling model results with observations. Four major field campaigns were undertaken between 2017-2018 in the Southern Ocean- SOCRATES, CAPRICORN-2, MARCUS, and MICRE (see Section 2.1 and Section 7 for details on the different campaigns). CAPRICORN-2 and MARCUS collected ship-board measurements during Austral summer, SOCRATES was a concurrent aircraft campaign, and MICRE had limited but continuous measurements at Macquarie Island for a full year. The main motivation for all these studies was to provide observations to improve climate model simulations of boundary layer processes, shallow convection, clouds, and aerosols over the Southern Ocean (Marchand et al. 2014). Our group's focus was on making measurements of ice nucleating entities (INEs) in seawater and ice nucleating particles (INPs) and aerosols in the marine boundary layer (MBL), to understand the role primary ice nucleation (see Section 1.2) plays in controlling the phase and lifetime of SO clouds, as well as the source of INPs to the Southern Ocean marine boundary layer.

1.2 ATMOSPHERIC ICE NUCLEATION AND MARINE INPS

Ice nucleation occurs through two main pathways in the atmosphere: homogeneous freezing of cloud drops below ~-36°C, and heterogeneous ice nucleation, which occurs when a suitable particle is present that can lower the activation energy required to form a critical ice embryo (Kanji et al. 2017). Heterogeneous ice nucleation can occur at temperatures <-36°C, though here we will consider only heterogeneous nucleation at temperatures warmer than -35°C, which is relevant for glaciation of mixed phase clouds. Multiple pathways are possible for heterogeneous ice nucleation, with immersion freezing (freezing initiated by a particle immersed in a liquid drop) the most important for mixed phase clouds (Kanji et al. 2017), such as are ubiquitous in the Southern Ocean. On a global scale, most precipitation in clouds is initiated from the ice, rather than the liquid, phase, which influences the hydrological cycle and cloud lifetime (Rogers 1988). Cloud glaciation also affects atmospheric radiative transfer due to the differences in optical properties between liquid droplets and ice crystals.

Historically, INPs have been proposed to be insoluble particles with surface structures that provide sites for freezing to occur (Pruppacher and Klett 2010), with the number of such active sites scaling with particle surface area (see Kanji and Abbatt 2010). On a global scale, mineral dusts dominate INP numbers due to their effective ice nucleating ability (Hoose and Möhler 2012) and their large emission rates (Ginoux et al. 2012). Dust can influence cloud phase locally or following long-range transport (Kanji et al. 2017). At temperatures warmer than -10°C, biological ice nucleators (pollen, fungal spores, bacteria) become important (Garcia et al. 2012; Pummer et al. 2015). INP concentrations generally exhibit an exponential increase with decreasing temperature, with a range of concentrations of several orders of magnitude at any one temperature even for airmasses with similar particle composition (Kanji et al. 2017).

More limited measurements of marine aerosol from *in situ* and mesocosm studies have shown sea spray aerosol (SSA) INPs include marine diatoms and their exudates (Wilson et al. 2015; Rosinski et al. 1987), as well as marine macromolecules (McCluskey et al. 2018b). Correlations between INP concentrations in aerosol (Rosinski et al. 1987; DeMott et al. 2016; Mc-

Cluskey et al. 2018b; Schnell and Vali 1976) or ice nucleating entities (INEs) in seawater and sea surface microlayer samples (Irish et al. 2017; Wilson et al. 2015; McCluskey et al. 2018b) with marine biological activity have also been shown. The sea surface microlayer (SML) is a thin layer (<1 mm) at the interface between the ocean and the atmosphere, with very different physical and chemical properties than bulk seawater (Engel et al. 2017). It is often enriched in organic material relative to the bulk, which can be transferred to sea spray aerosols upon bubble bursting at the ocean surface (see van Pinxteren et al. 2017; Engel et al. 2017). Conflicting results regarding enrichment of INEs in SML over bulk seawater have been reported for North Atlantic and Arctic measurements, as well as for correlations between INEs and measures of microbial activity (Irish et al. 2017; Wilson et al. 2015). Mesocosm studies indicate the correlation between INP concentration and biological activity is strongest during the death phase of phytoplankon blooms (McCluskey et al. 2018b), coincident with enhanced organic aerosol production (O'Dowd et al. 2015; Wang et al. 2015), although this has yet to be verified with *in situ* measurements. Limited compositional and size measurements of marine INPs and INEs have been reported, but ambient results suggest heat-labile biological particles <0.2 μm (Irish et al. 2017; Wilson et al. 2015) are responsible for ice nucleation activity in marine aerosol. McCluskey et al. (2018b) identified two main types of marine INPs from mesocosm studies: (1) thermally-labile, particulate organic carbon that is larger than 0.2 μm, which may be associated with cells and cellular debris, and (2) refractory dissolved organic carbon that is smaller than 0.2 μm and which is not affected by heating. Category (2) from McCluskey et al. (2018b) is most similar to ambient observations (Irish et al. 2017; Wilson et al. 2015), although differences in heat stability of these INEs between laboratory and *in situ* measurements should be noted.

Ice nucleating particles exhibit very different immersion freezing temperature spectra depending on their source- both in shape and cumulative number concentrations (DeMott et al. 2016; Petters and Wright 2015). As a result, not only INP concentrations, but also their chemical and physical characteristics, affect the consequent aerosol-cloud interactions. Marine INP temperature spectra are generally 1-2 orders of magnitude or more lower than continental mea-

surements (DeMott et al. 2016), with SO measurements (McCluskey et al. 2018c; Schmale et al. 2019) at the lower bound of those reported from other ocean regions (DeMott et al. 2016). Observed low INP numbers, its remote location, and recent modeling work (Burrows et al. 2013; Vergara-Temprado et al. 2017) support the idea that the SO INP population is dominated by marine SSA and distinct from that found in the northern hemisphere, though direct field confirmation is still needed. Recent observations that mineral dust dominates over locally-sourced marine INPs in the Canadian Arctic (Irish et al. 2019) means measurements of pristine marine aerosols (Hamilton et al. 2014) from the Southern Ocean are invaluable in understanding the role of marine INPs in cold cloud processes. The unusually high proportion of supercooled liquid water in SO clouds (Morrison et al. 2011; Chubb et al. 2013) is consistent with low numbers of INPs in this region and indicates that INP concentrations and composition may strongly control cloud phase and precipitation formation over the SO (Vergara-Temprado et al. 2018). Modern INP observations in the Southern Ocean are limited in extent (McCluskey et al. 2018c; Schmale et al. 2019) and data from recent campaigns will greatly enhance our ability to understand the role they play in SO clouds.

1.3 REPRESENTING ICE NUCLEATION IN MODELS

Representing cloud microphysical processes in global models is difficult because fundamental details are poorly understood, and the spatial and temporal scales they occur on are small, requiring parameterization. Theoretical frameworks describing ice nucleation generally fall into two categories (Kanji et al. 2017): time-dependent approaches such as classical nucleation theory (Pruppacher and Klett 2010) and time dependent freezing rate models (Vali 1994), or time-independent techniques which describe freezing due to ice nucleation active surface sites on a particle as a function only of temperature (Vali 1971). The time-independent methods have the advantage of being simple to implement in models, since only particle surface area or number is required, but assume the same normalization method can be used to characterize INPs of different types, which may not be true for internally mixed particles (Kanji et al. 2017).

Field and laboratory studies can and have been used to characterize INPs based on ice nucleation active surface site density (see Section 2.5.5) or particle number concentration in specific size ranges, usually >0.5 μm. These have been developed for dust (see Niemand et al. 2012; Ullrich et al. 2017; DeMott et al. 2015), mixed continental aerosols (DeMott et al. 2010), marine aerosols (McCluskey et al. 2018a), fossil fuel black carbon (Schill et al. 2016), and multiple INP types (Phillips et al. 2008; 2012). Relationships between INP concentration and particle surface area or number concentration for certain particle sizes have been recognized since at least the 1960s, and follow linear or power law relations (Berezinski et al. 1988; DeMott et al. 2003; Richardson et al. 2007; Georgii and Kleinjung 1967). The dominant role of dust in atmospheric ice nucleation corroborates the relationships found between INP concentrations and particles >0.5 μm, as mineral and soil dust are characterized by a dominant supermicron mode (Maring et al. 2003). These types of parameterizations are often only valid for the temperature range in which they were derived (Hoose and Möhler 2012), and ambient and laboratory measurements may need to be combined to cover the entire range of heterogeneous ice nucleation temperatures (Kanji et al. 2017). One drawback with this approach is that each class of INPs can require dramatically different parameterization constants, and even functional forms (discussed in Section 5). Additionally, it assumes that either ice nucleating efficiency is independent of particle size or INP size is uniform for a specific source (Kanji et al. 2017). If particle composition varies with size, then ice nucleating efficiency will also with size, and normalization by surface area or particle number may not predict INP concentrations accurately.

Observations of aerosol-cloud interactions, and especially of ice formation processes, are rare in the Southern Ocean. The results presented here will mainly cover ship-board measurements collected during CAPRICORN-2 (Section 2.1). These, along with results from the related MICRE, MARCUS, and SOCRATES campaigns are adding greatly to the number and spatial distribution of modern measurements (Figure 3.5) of primary ice nucleation. An overview of the spatial and temporal variability of aerosols and INPs during CAPRICORN-2 will be presented in Section 3. Methods used to estimate aerosol surface area and number concentrations, for

use in INP parameterization, are shown in Section 4. Parameterizations of INP concentrations using aerosol surface area and number concentrations will be discussed and compared to previously reported relationships in Section 5. Finally, preliminary results from the NSF/NCAR G-V research aircraft during the SOCRATES campaign will be shown in Section 7. These represent the first Southern Ocean measurements of INPs from below cloud base in the marine boundary layer (MBL), of cloud residuals inside clouds, and above clouds in the mid-troposphere, and will be invaluable in understanding the vertical structure of INPs.

2. Data and Methods

2.1 SOCRATES AND CAPRICORN-2 FIELD CAMPAIGNS

Two simultaneous field campaigns were undertaken in Jan.-March 2018 in the Southern Ocean region south of Tasmania with the goal of providing in-situ measurements with which to improve and validate climate model simulations of marine boundary layer (MBL) processes, clouds, and aerosols over the Southern Ocean. The Southern Ocean Cloud Radiation Aerosol

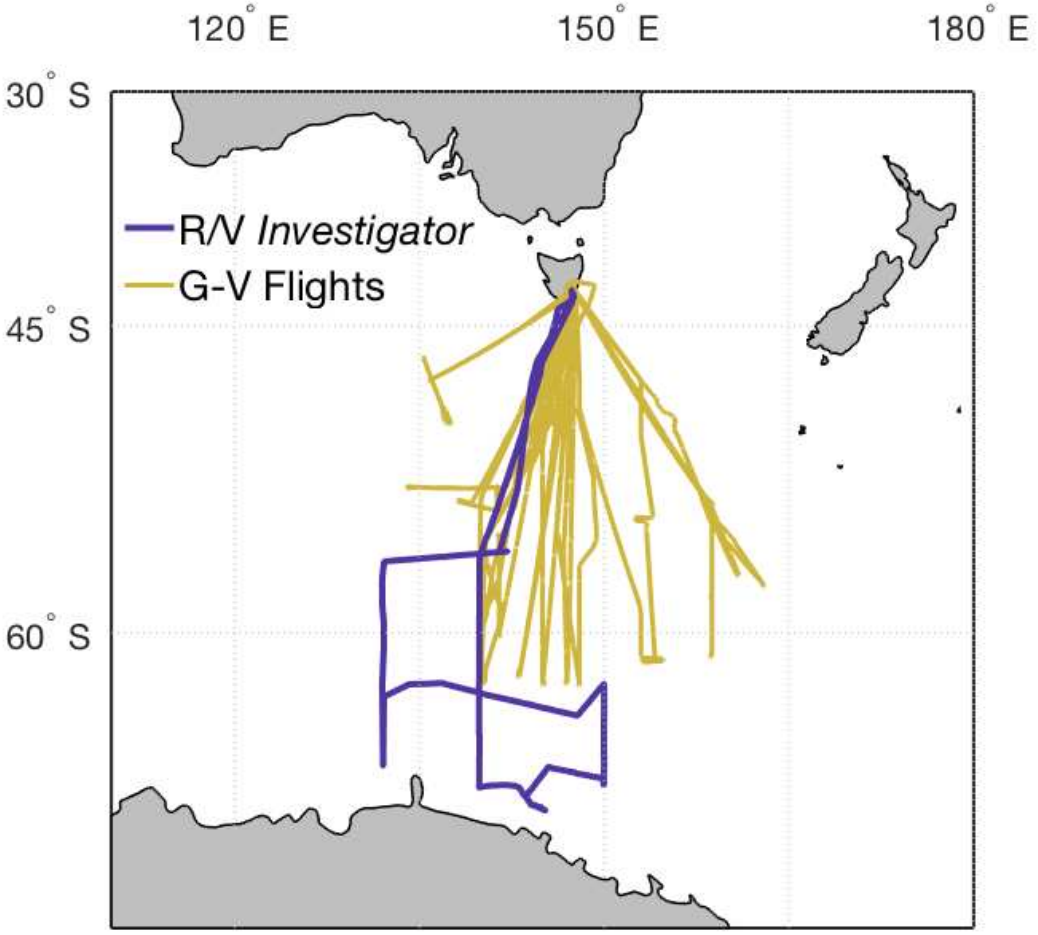

Figure 2.1: Flight tracks for all 15 SOCRATES research flights, and the voyage track for CAPRICORN-2.

Transport Experimental Study (SOCRATES) used the NSF/NCAR G-V aircraft to make measurements of cloud and aerosol properties in the MBL, in clouds, and above clouds in the

region. Complementary MBL measurements were conducted during the associated Clouds, Aerosols, Precipitation, Radiation and atmospherIc Composition Over the southeRN ocean (CAPRICORN-2) study on the R/V *Investigator* (IN2018_V01), an Australian Government research platform operated by the Commonwealth Science and Industrial Research Organisation (CSIRO). Flight tracks for all 15 SOCRATES flights and the ship track for CAPRICORN-2 are shown in Figure 2.1. These measurements were made during late Austral Summer into early Austral Autumn.

2.2 INSTRUMENTATION

2.2.1 Continuous Flow Diffusion Chamber

The Continuous Flow Diffusion Chamber (CFDC) is an online instrument used to measure primary ice nucleating particle concentrations in an aerosol stream (Rogers et al. 2001; DeMott et al. 2016). A schematic of the operating principles of the CFDC is shown in Figure 2.2. Two concentric, cylindrical walls are coated with ice and thermally controlled to establish a temperature gradient between the walls in the upper "growth" region of the chamber. Nearly steady-state RH and temperature profiles are established in this region, where aerosol particles can activate into ice and grow. In the lower, "evaporation", section of the chamber, the temperature gradient between the walls is eliminated, creating a region of water subsaturation that allows for evaporation of water droplets and wet aerosols, but retention of ice crystals. An optical particle counter (OPC) is located directly below the CFDC chamber and is used for optical detection of particles as they exit the chamber. Ice crystals are distinguished from smaller aerosols and any remaining water droplets by their larger size. Aerosol is drawn into the CFDC at the top of the chamber and flows vertically downwards between the concentric chamber walls in a lamina between particle-free sheath air streams. Prior to entering the chamber, the aerosol stream is dried using silica gel and molecular sieve diffusion driers to below the frost point, and supermicron aerosols that might interfere with optical detection of ice crystals are removed by passing the aerosol stream through two identical single-jet impactors in series, each with a cutpoint of 1.5

or 2.4 μm aerodynamic diameter. The aerosol lamina flow is 1.5 L min^{-1}, giving a several-second residence time of aerosols in the growth and evaporation regions of the CFDC chamber. During this study, the CFDC was operated at water-supersaturated conditions of 104-106% RH in the growth region and temperatures in the aerosol lamina between -25 and -33 °C. This method forces activation of aerosols into cloud droplets prior to ice nucleation, giving results similar to offline immersion freezing techniques (DeMott et al. 2016).

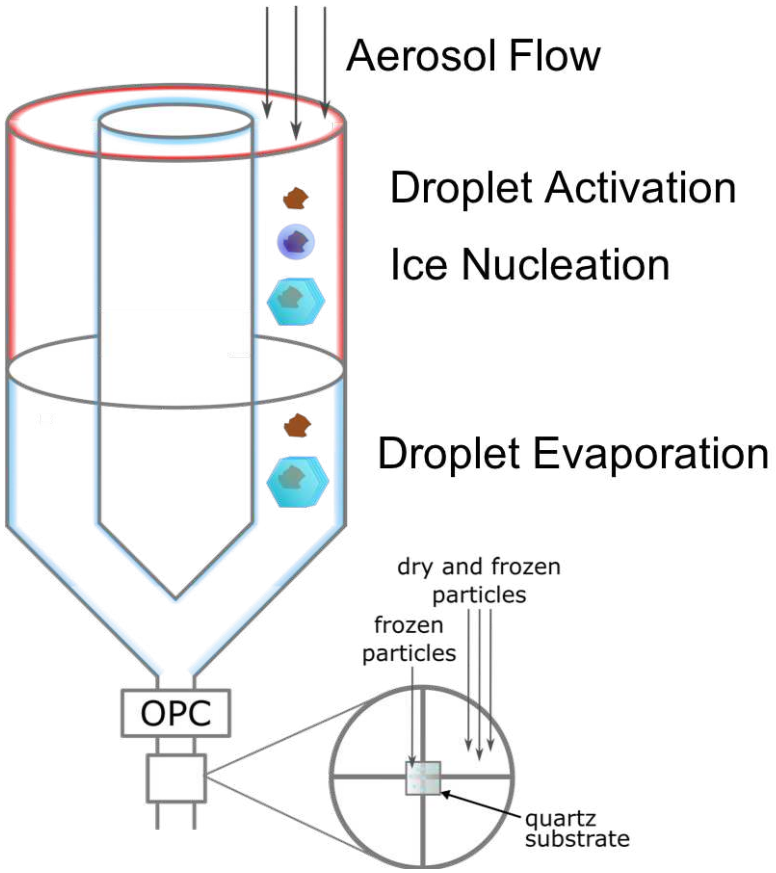

Figure 2.2: Schematic of CFDC operation.

On the R/V *Investigator*, the CFDC sampled from a custom-designed aerosol sampling inlet located approximately 18.4 m above sea level at the bow of the ship. Ambient air containing particles was pulled into a 16 cm diameter stainless steel tube at approximately 1800 L min^{-1}, and transmitted to a sampling manifold in the aerosol laboratory, where the CFDC and other aerosol instruments subsampled from the main flow. The total distance between the sample

inlet and sampling manifold is approximately 9 m, and a further 0.6 m to the CFDC inlet. Particle transmission efficiency through the aerosol sampling inlet, including dependence on wind speed and ship motion, has not been fully characterized. However, preliminary modeling results suggest greater than 90% transmission efficiency of particles <2.5 μm aerodynamic diameter (see Section 2.3 for a discussion of the calculations), and so no corrections were applied to measured INP concentrations from the CFDC.

On the G-V, the CFDC sampled from both the HIAPER modular inlet (HIMIL inlet; Stith et al. 2009) in clear air regions above and below clouds, and from a counterflow virtual impactor (CVI) inlet within clouds (Noone et al. 1988; Twohy et al. 2010) to detect INPs within cloud-residuals. Particle transmission efficiencies for the HIMIL inlet have been previously characterized as >94% for submicron particles (Stith et al. 2009), and no corrections were applied to the CFDC data, which has an upper limit of 2.5 μm aerodynamic diameter. CVI transmission efficiencies have been modeled using computational fluid dynamics software and applied based on Twohy et al. (2010).

2.2.1.1 Chemical Composition of INPs Activated in the CFDC

Following the OPC at the outlet of the CFDC chamber is a single-jet impactor with a cutsize of 4 μm aerodynamic diameter (Figure 2.2), which can be used to collect ice crystals that activate inside the CFDC chamber (see McCluskey et al. 2014). The impactor is fitted with 3-mm diameter Cu grids (coated with formvar and C) for offline electron microscopy (TEM) analysis of single-particle ice crystal residuals, and allows for classification of the collected INPs into carbonaceous, mineral, and salt categories (see McCluskey et al. 2014). Si-nitride substrates were also used to collect INP residuals for STXM/NEXAFS (Scanning Transmission X-ray Microscopy with Near-Edge X-ray Absorption Fine Structure) analysis, which gives insight into the presence and functional groups of organic components of INPs (Russell et al. 2002; 2010; Takahama et al. 2007).

2.2.2 *Aerosol Concentrator*

Due to the low expected number concentrations of INPs over the Southern Ocean, an aerosol concentrator was employed on the R/V *Investigator* (MSP Corporation Model 4240), as has been done in previous ground-based (Tobo et al. 2013) and ship-board studies (McCluskey et al. 2018c). The aerosol concentrator effectively concentrates aerosols >0.5 μm aerodynamic diameter (Figure 2.3), which are then fed into the inlet of the CFDC. The concentration factor achieved depends on the size of the particles that nucleate into ice crystals in a given environment, and has been measured to be in the range of 80-100 in past campaigns (see DeMott et al. 2017). Increasing the concentration of >0.5 μm particles improves measurement statistics and lowers the CFDC detection limit, assuming the mode size of INPs is larger than 0.5 μm. This allows for collection of CFDC measurements at warmer temperatures, where the INP concentration is lower, and provides for better overlap with offline INP measurement techniques (see Section 2.2.3). The aerosol concentrator sampled from within the aerosol laboratory using a dedicated 1-inch diameter stainless steel sampling line due to its large flowrate of 250 L min^{-1}, which was located next to the main aerosol sampling inlet.

2.2.3 *Ice Spectrometer*

In addition to real-time INP measurements using the CFDC, aerosol filters were collected and analyzed offline via immersion freezing using the CSU Ice Spectrometer (IS). Aerosols were collected onto pre-sterilized 0.2 μm, 47 mm track-etched polycarbonate membrane filters (Whatman Nucleopore^{TM} filters, GE Healthcare Life Sciences) in either pre-sterilized stainless steel filter housings on the G-V, or disposable, sterile, open-faced filter units (Nalgene sterile analytical filter units, Thermo Fisher Scientific) on the R/V *Investigator*. Sampling flow rates were targeted to be ~15 L min^{-1}, to give high collection efficiencies of both submicron and supermicron aerosols. Filters were pre-cleaned by soaking in 10% H_2O_2 for 10 minutes, followed by three rinses in 0.1 μm filtered deionized (DI) water, and dried on aluminum foil inside a UV-sterilized laminar flow hood.

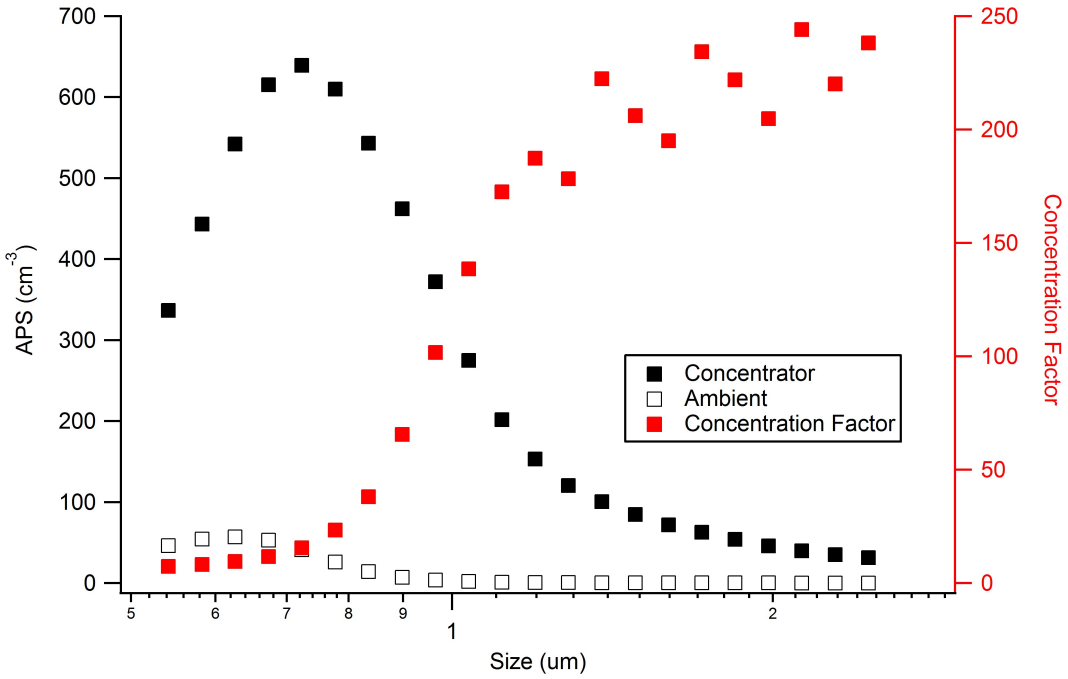

Figure 2.3: Aerosol concentration factor as a function of size when using the aerosol pre-concentrator. The data shown were collected in May 2016, in association with reported results in DeMott et al. (2017).

For the R/V *Investigator* samples, the filters were immediately loaded into sterile disposable filter units and re-sealed in plastic bags until use. Filter units were opened on deck and mounted beneath a rain hat for alternating 24-48 hr periods at approximately 23 m above sea level. In order to limit ship exhaust contamination, the filter pump was powered with a sector sampler, which provided power to the pump only when the wind speed relative to the ship was between 10 and 80 kn, the ship-relative wind direction was from the forward 90° (relative wind directions greater than 45° and less than 315°), and the total particle concentrations measured by a CPC were stable and less than 2000 cm^{-3}.

For the G-V samples, the pre-cleaned filters were wrapped in aluminum foil and sealed in plastic bags for transport to Tasmania. The stainless steel filter holders were cleaned with 10% H_2O_2 and allowed to dry after each flight prior to being re-loaded with pre-cleaned filters. During flights, filters were mounted in the CFDC rack and ambient air from the HIMIL was pulled through them for up to an hour during times above or below cloud levels. Different filters were

collected in the marine boundary layer versus above cloud, in order to assess the differences in INP populations present in different regions of the atmosphere.

In both cases, following aerosol collection, filters were removed from the holders using clean plastic tweezers and stored frozen (-20 °C) in sterile petri dishes sealed with parafilm. On the R/V *Investigator* the samples were removed from the holders inside a laminar flow hood, which was not available for the G-V samples. Blank filters were collected throughout the voyage and during the research flights and processed identically to the samples to provide an estimate of instrument background. After the campaigns, the filters were pooled and shipped back to CSU frozen using a dry nitrogen shipper (Cryoport Incorporated), then stored frozen (-20 °C) until analysis.

Measurement of the immersion freezing temperature spectrum of an aerosol sample is accomplished by placing liquid aliquots containing re-suspended particles into temperature-controlled aluminum blocks and recording the number of wells that freeze as the temperature is lowered (Hiranuma et al. 2015; Hill et al. 2014; 2016). Filters are first transferred to pre-cleaned 50 mL polypropylene tubes (Corning) and then immersed in 7-10 mL of 0.1 μm filtered (DI) water before they are shaken using a Roto-Torque for 20 min to release particles from the filters. The suspension is then distributed into 32 aliquots of 50 uL in sterile 96 well PCR trays (μCycler), and the trays are placed into the aluminum blocks of the IS. The temperature of the blocks is lowered by 0.33 °C min^{-1} and the number of wells frozen is optically detected using a camera at ~0.6 °C intervals between 0 to -29 °C. Calculation of INP concentrations in the liquid suspension follows Vali (1971):

$$n_{INP} = \frac{-\ln(f)}{V}, \tag{2.1}$$

where n_{INP} is the concentration of INPs in the liquid sample, f is the fraction of unfrozen wells and V is the volume of each well. These are then converted to ambient atmospheric concentrations using the total air collection volume for each filter, as measured by a mass flowmeter (TSI 4043) in line with the filter and pump. Uncertainties are reported as binomial sampling confidence intervals (95%) as in Agresti and Coull (1998).

2.2.3.1 Chemical Composition of INPs in the Ice Spectrometer

Inferences about the composition of INPs (Section 2.2.1.1) are also possible using the Ice Spectrometer. Ice nucleating particles produced by bacteria and fungi are often proteins (Pummer et al. 2015), and heating the sample is a simple way to denature these proteins and infer the contribution of biological INPs to a sample (Hill et al. 2016; Suski et al. 2018). A 2 mL aliquot of re-suspended sample is placed into a pre-cleaned polypropylene tube (Corning), then immersed in boiling water (~95 °C in Ft. Collins, CO) for 20 minutes before cooling to room temperature and analyzing on the IS with our standard protocols. The difference between the immersion freezing temperature spectra with and without heat treatment is used to assess the contribution of biological INPs to an overall sample.

Oxidation experiments are used to selectively destroy organic materials, leaving behind refractory (typically mineral) INPs (Hill et al. 2016; McCluskey et al. 2018a). Aliquots from aerosol filter suspensions are digested with 10% hydrogen peroxide while immersed in 95 °C water and illuminated with UV for 20 min. The residual hydrogen peroxide is removed via the addition of catalase once the solution has cooled to room temperature, to prevent freezing point depression from affecting IS measurements. The treated solution is then aliquoted into PCR trays and analyzed as usual. The INP temperature spectra remaining after oxidation is inferred to be the mineral component, and the difference between pre-and post-oxidation spectra corresponds to organic INPs.

2.2.4 Aerosol Size Distribution and Surface Area Measurements

The aerosol laboratory on the R/V *Investigator* contains a suite of instruments for measuring aerosol properties. These included sub- and supermicron aerosol size distributions, aerosol scattering, aerosol chemical composition, cloud condensation nuclei number concentration, fluorescent biological particles, and total aerosol number concentration (Figure 2.4). For the purposes of this study, I will focus on the measurement of aerosol size distributions, as these provide normalization of INP concentrations by aerosol surface area, a commonly used metric

to parameterize INPs in climate models (see DeMott et al. 2016; Ullrich et al. 2017; Niemand et al. 2012; McCluskey et al. 2018a). The utility of this metric in the Southern Ocean region will be discussed in Section 5, and a comparison of the different methods used to estimate aerosol surface area are given in Section 4. Results of aerosol measurements on the G-V are not available yet, and will not be discussed in this work. Future publications will compare MBL measurements of aerosol surface area between the G-V and R/V *Investigator* for periods when the aircraft flew over or near the ship.

2.2.4.1 SMPS and APS Measurements

Submicron and supermicron aerosol size distributions were measured directly using a TSI Scanning Mobility Particle Sizer (TSI SMPS 3080) for aerosols in the range 15-660 nm and a TSI Aerodynamic Particle Sizer (TSI APS 3320) for aerosols between 500 nm and 20 μm. Both the SMPS and APS sampled from the same sampling manifold as the CFDC and other aerosol instruments in the R/V *Investigator* aerosol laboratory. The APS was located approximately 1 m from the sampling manifold, and care was taken to minimize losses of supermicron particles. Both aerosol streams were dried with silica gel diffusion driers before measurement.

The SMPS separates submicron aerosols by their electrical mobility diameter, and then counts particles in each bin using a condensation particle counter (TSI CPC 3010). Aerosols are introduced into a chamber between 2 vertically oriented concentric cylindrical conductors, where a constant electric field is generated. The force balance between the electric field acting on charged particles and the drag experienced by the particle determines which sizes of particles are transmitted to the CPC (DeCarlo et al. 2004). The electric field strength inside the chamber is varied by changing the voltage applied to the central conductor, transmitting particles of increasing size to the CPC and generating a submicron aerosol size distribution over the course of one to several minutes. Electrical mobility diameter is not dependent on particle density, but does depend on particle dynamic shape factor or asphericity (χ). Particles with $\chi = 1$ are spherical, in which case electrical mobility diameter (d_m) is equivalent to physical diameter (d_p) (DeCarlo et al. 2004). The SMPS size measurements were calibrated before, after, and at

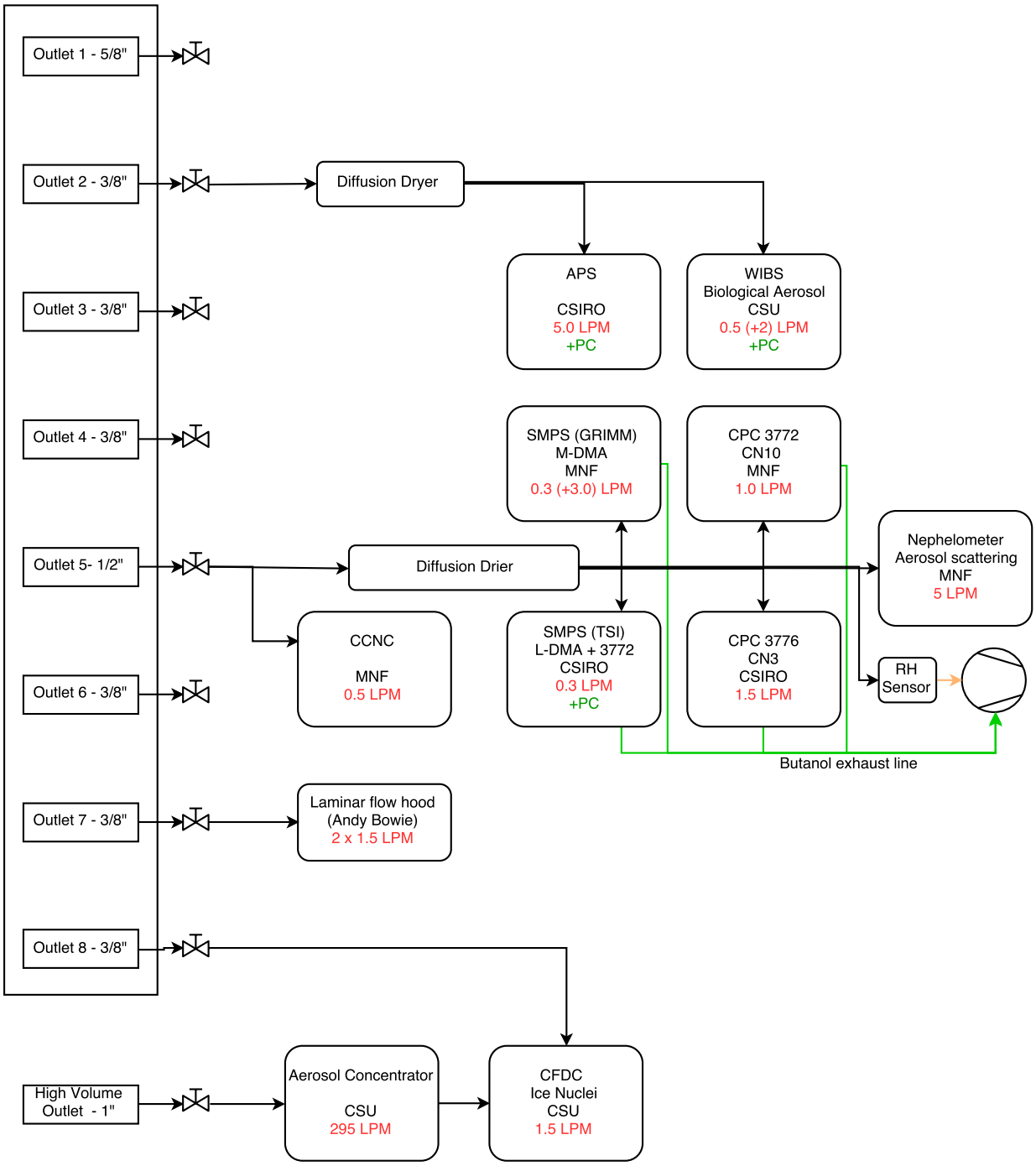

Figure 2.4: Flow diagram for aerosol instruments during CAPRICORN-2.

two-week intervals during the voyage against polystyrene latex spheres (PSLs) of known sizes. No adjustments were made to the measured electrical mobility sizes, as they agreed with the known PSL sizes to within ± 5 nm during each calibration.

An Aerodynamic Particle Sizer (APS) measures the aerodynamic diameter of supermicron aerosols by timing how long individual particles take to pass between two laser beams oriented perpendicular to the aerosol flow path. Particles are detected by measurement of side-scattered light onto a solid-state photodetector, and binned by particle size between 0.5-20μm (TSI APS manual). Aerodynamic diameter (d_a) is the diameter of a standard density (ρ_0) sphere with the same terminal settling velocity as the particle being measured, and depends on particle density (ρ_p) as well as shape factor:

$$d_a = d_{ve}\sqrt{\left(\frac{\rho_p}{\rho_0 \chi}\right)} \tag{2.2}$$

where d_{ve} is the volume-equivalent diameter of a particle (DeCarlo et al. 2004). Eq. (2.2) can be rearranged to solve for d_{ve} given the measured aerodynamic diameters and assumed particle density and shape factor. The APS aerodynamic size measurements were calibrated against PSLs of known size and ρ_0=1.05 g cm^{-3} at weekly intervals during the voyage, as well as before and after the campaign. Reported d_a were scaled based on an orthogonal distance regression (ODR) fit on the pooled calibration data (Figure 2.5).

After correcting SMPS and APS data for particle density, RH, and shape factor (see Section 2.2.4.5), both distributions were converted into d_p. Corrections were applied to the APS number concentrations to account for estimated losses in the aerosol inlet (see Section 2.3). The APS size distribution was cut off at 7.5 μm, as the calculated inlet transmission efficiency dropped below 10% above this size. Inlet transmission efficiency for submicron particles was estimated at >95% for all sizes, so no further corrections were applied to the SMPS number concentrations. The SMPS and APS distributions were merged at a diameter of 0.42 μm to give a single particle size distribution. Particle surface area distributions and integrated surface areas were then calculated assuming all particles were spherical (see Section 2.2.4.5).

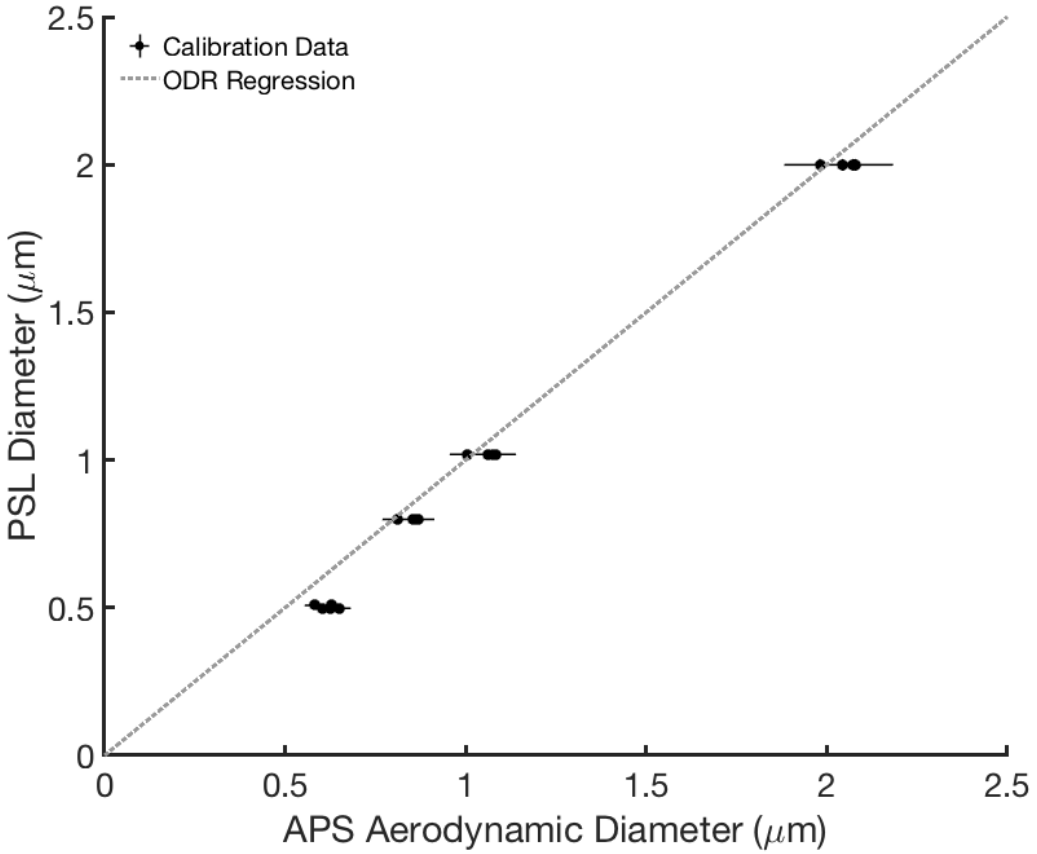

Figure 2.5: ODR regression used to correct APS aerodynamic diameters during CAPRICORN-2.

2.2.4.2 WIBS Measurements

Fluorescent bioaerosol particles (FBAPs) were measured on both the R/V *Investigator* and G-V using identical Wideband Integrated Bioaerosol Spectrometer (WIBS-4A, Droplet Measurement Technologies) instruments. On the R/V *Investigator*, the WIBS co-sampled with the APS from the main aerosol inlet. On the G-V, the WIBS sampled from the CVI inlet, as described in Twohy et al. (2016). The WIBS measures both particle size (optical diameter) and fluorescence in spectral regions that target the amino acid tryptophan and the coenzyme NADH (nicotinamide adenine dinucleotide). Biological particles are expected to contain these compounds, and to fluoresce strongly in the WIBS, while non-biological particles are expected to fluoresce weakly or in different spectral regions (Pöhlker et al. 2012).

Particle-laden air is drawn into the inlet of the WIBS, and particles are first sized using scattered light from a 635 nm diode laser. Two filtered Xenon flashlamps (280 nm and 370 nm) are triggered in sequence by the scattering signal, and fluorescence is monitored using two PMTs (310-400 nm and 420-650 nm). Flashlamp timing was optimized prior to the campaign using size-selected 2 wt% quinine (in isopropanol) aerosols generated using a nebulizer. Because the 370 nm Xe flashlamp is in the detection range of one of the PMTs, this combination yields three useful fluorescence channels, and seven combinations of fluorescence responses (Perring et al. 2015). The flashlamps have a maximum firing rate of 125 Hz due to needed recharging time, so reported particle concentrations have been corrected for particles missed during recharge periods using the ratio of total particles with scattering signal to particles for which the flashlamps fired (see Perring et al. 2015). Background fluorescence values in each channel in the absence of particles were measured daily. Only particles with fluorescence values greater than 2.5 standard deviations above the daily mean background value are reported here (Twohy et al. 2016).

For this study, only the R/V *Investigator* WIBS data will be considered, as they can be directly compared to other aerosol surface area measurements. WIBS particle size measurements were calibrated weekly during the campaign using PSLs of known sizes. Following Perring et al. (2015), scattering values from the PSL calibrations were used in conjunction with Mie theory

(PSL refractive index of 1.593 at 635 nm; Reed et al. 2016) to obtain optical particle sizes for ambient SSA. These optical sizes are assumed to be equivalent to physical diameter (see Section 2.2.4.5). Particles below 0.8 μm were removed from the dataset, as particles smaller than this are at or below the limit of detection for the WIBS PMTs with their current gain setting (Perring et al. 2015). As for the APS, the WIBS particle concentrations were corrected to account for estimated aerosol transmission efficiency in the inlet (see Section 2.3), and particles above 10 μm were also removed from the dataset due to low inlet transmission efficiency. Finally, the reported WIBS sizes were converted to dry diameter (see Section 2.2.4.5) using the assumed growth factor ($g_e(RH)$ ~1.5) at 55% RH (Zieger et al. 2017). Particle surface area distributions and integrated surface area estimated from the WIBS were then calculated assuming spherical particles (see Section 2.2.4.5).

2.2.4.3 Nephelometer Measurements

A third estimate of aerosol surface area was made using a nephelometer on the R/V *Investigator* (Polar Nephelometer, Ecotech Aurora 4000), following DeMott et al. (2016). A nephelometer measures light scattering in an air sample due to the presence of particulates. The Aurora 4000 cycles through different shutter angles over several minutes to provide angular scattering information for a sample at three different wavelengths: 450 nm, 525 nm, and 635 nm. When estimating aerosol surface area, only periods when the shutter was set to 10° are used, which corresponds to measurements of integrated total light scattering from 10-170°. Estimates of aerosol surface area requires aerosol scattering coefficients (b_{sp}), aerosol Ångstrom exponents (å), and RH at which the scattering measurements were made. The (b_{sp}) and RH are measured and reported by the nephelometer directly. Ångstrom exponents were calculated from the reported scattering coefficients using:

$$\text{å} = \frac{-\log(b_{sp}^{\lambda_1}/b_{sp}^{\lambda_2})}{\log(\lambda_1/\lambda_2)}, \tag{2.3}$$

where λ_1 and λ_2 refer to different measured wavelengths (Seinfeld and Pandis 2016). Following DeMott et al. (2016), 450 nm was used for λ_1 and 635 nm for λ_2 in (2.3).

The calculated Ångstrom exponents were then used to estimate the average aerosol scattering efficiency (Q). If the Ångstrom exponent was larger than 1, Q was assumed to be 3 (submicron particles dominate scattering), and if the Ångstrom exponent is smaller than 1, Q was assumed to be 2 (supermicron particles dominate scattering) (DeMott et al. 2016; Mulcahy et al. 2009). The integrated aerosol surface area can then be estimated from the measured scattering coefficient at 450 nm and the calculated scattering efficiency (DeMott et al. 2016):

$$SA_{tot} = 4\left(\frac{b_{sp}^{450nm}}{Q}\right), \tag{2.4}$$

The nephelometer has an inlet heater, which lowered the relative humidity inside the instrument to below 40% for all measurements, so the aerosols were assumed to be dry and no corrections were applied to the calculated surface area to account for particle hygroscopic growth. Deriving aerosol surface area from nephelometer measurements requires the assumptions that particles are spherical, and they can be characterized by having a single effective scattering size. Unlike for the APS and WIBS, (Section 2.3), the aerosol surface area estimated using the nephelometer was not able to be corrected for inlet transmission efficiency, as transmission efficiency is highly size dependent, and the measured aerosol scattering coefficients are a bulk property.

2.2.4.4 LIDAR Measurements

The final technique used to retrieve aerosol surface area makes use of the mini-Raman LIDAR on the R/V *Investigator* (Leosphere RMAN-510 Raman UV polarization LIDAR, 355 nm), which provided profiles of height-resolved backscatter along the voyage track (see Alexander and Protat 2019). The LIDAR was located on deck near the IS filter samples, approximately 23 m above sea level, and was oriented towards the ship local vertical. Simon Alexander at the Australian Antarctic Division estimated vertical profiles of aerosol surface area following Mamouri

and Ansmann (2016). This technique uses the measured height profiles of aerosol backscatter coefficient and linear depolarization ratio to determine the contribution of different aerosol types (desert, marine, and continental) to the observed signal. Vertical profiles of aerosol extinction coefficient are then derived using LIDAR ratios based on previous measurements in different regions, which can be converted to particle surface area using conversion parameters derived from comparison of AERONET and LIDAR data.

LIDAR particle linear depolarization ratios were consistently less than 5% throughout CAPRICORN-2, indicating marine aerosols were the primary aerosol type observed (Alexander and Protat 2019). Profiles close to Tasmania occasionally had contributions from continental aerosols, and so data north of 46°S are excluded from this analysis. The near-surface mixed layer mean LIDAR ratio (S = 20 sr) observed during CAPRICORN-2 and the preceding CAPRICORN-1 voyage (similar region) was used for all profiles to estimate height-resolved aerosol extinction coefficients from the backscatter measurements (Alexander and Protat 2019). Vertical profiles of aerosol surface area were then estimated from the aerosol extinction coefficients using the marine aerosol conversion factor from Mamouri and Ansmann (2016). Calculated surface areas were corrected for hygroscopic growth assuming a marine boundary layer RH of ~80% and a corresponding hygroscopic growth factor $g_e(RH)$ ~2 (Mamouri and Ansmann 2016). LIDAR-retrieved aerosol surface area values at 300 m were compared with the other estimates of MBL aerosol surface area, as below this level the LIDAR overlap function gives large uncertainties in backscatter and derived parameters. The retrievals of aerosol surface area are valid during periods of clear-sky conditions up to 3km, which was the reference height for particle backscatter used when solving the LIDAR equation for these profiles, and was chosen because aerosol backscatter was negligible above this level in all CAPRICORN-2 profiles (Alexander and Protat 2019). Profiles with cloud below 3km were identified using the LIDAR's calibrated attenuated backscatter and not considered in this analysis (Alexander and Protat 2018).

2.2.4.5 *Particle Density, Relative Humidity, and Shape Factor Corrections*

During CAPRICORN-2, aerosols were dried prior to measurement to below the efflorescence RH (ERH) of sea salt, ~45-48% (Tang et al. 1997). For submicron size distribution measurements using the SMPS (Section 2.2.4.1), particles are additionally dried within the instrument due to the introduction of dry sheath air at a 10:1 ratio to the sample flow. Thus, the measured size distributions are assumed to be aerosol dry diameters. However, sea salt particles retain residual water even below the ERH (Tang et al. 1997), and supermicron particles may not evaporate quickly enough in diffusion driers, such that the measured RH will underestimate the particle water content. As a result, for supermicron aerosol measurements (APS-Section 2.2.4.1 and WIBS- Section 2.2.4.2), the effective RH was assumed to be 55%, which corresponds to a hygroscopic growth factor $g_e(RH)$ ~1.5 (Zieger et al. 2017).

No measurements of particle shape factor were made during CAPRICORN-2. Submicron sea spray aerosol have higher organic mass fractions (O'Dowd and de Leeuw 2007) than supermicron SSA, and as a result have shape factors close to 1 (Zelenyuk et al. 2007) even when dried to below the ERH of sea spray aerosol. The supermicron aerosol were assumed to have residual water and thus weren't crystalline during measurement, so all particles are assumed to have $\chi = 1$.

The measured APS particle sizes depend on particle density, as well as $g_e(RH)$, neither of which were measured during these campaigns. Assuming the volumes of solutes and water are additive, particles are spherical ($\chi = 1$), and using a dry density of 2.017 g cm^{-3} for sea salt (Zieger et al. 2017) and 997.0479 kg m^{-3} for water at 298 K (Astle 1980), the density of supermicron aerosol particles was calculated to be $\rho_p = 1.3$ g cm^{-3}. Volume equivalent diameters were calculated for the APS using (2.2), the known density of PSLs ($\rho_0 = 1.05$ g cm^{-3}), and assumed particle shape factor ($\chi = 1$) and density ($\rho_p = 1.3$ g cm^{-3}). The calculated d_{ve} were then converted to dry diameter using the assumed growth factor ($g_e(RH)$ ~1.5) at 55% RH (Zieger et al. 2017). For spherical particles, $d_p = d_{ve} = d_m$ (DeCarlo et al. 2004), so the APS and SMPS size distributions can be directly compared.

The WIBS measures optical particle size (Section 2.2.4.2), which is equivalent to physical diameter assuming the particles are spherical and the particle refractive index matches that of the calibration particles. Making these assumptions, the reported WIBS particle sizes were assumed to be d_p. As for the APS, the reported WIBS sizes were corrected using the assumed growth factor ($g_e(RH)$ ~1.5) at 55% RH (Zieger et al. 2017) to give particle dry diameters.

As mentioned previously, the nephelometer-derived aerosol surface area estimate was not corrected for hygroscopic growth, as all measurements were made at less than 40% RH (Section 2.2.4.3). The LIDAR estimate of aerosol surface area is corrected for aerosol hygroscopic growth assuming an MBL RH of ~80% and a corresponding hygroscopic growth factor for SSA of $g_e(RH)$ ~2 (Section 2.2.4.4).

2.2.5 Chlorophyll a Measurements during CAPRICORN-2

Measurements of chlorophyll *a* (chl) depth profiles were collected at most of the 108 CTD stations along the CAPRICORN-2 voyage track. A Wetlabs FLBBRTD fluorometer measured in-situ chlorophyll *a* fluorescence (excitation 470 nm, emission 695 nm), which was converted into μm L^{-1} chl using a manufacturer-supplied calibration (Rosenberg and Rintoul 2018). Dark profiles were collected during two casts by taping over the fluorometer sensor and were used to correct the reported chl profiles for instrument noise. Surface chl values were estimated by averaging over the upper 30 m of the water column.

2.3 R/V *INVESTIGATOR* AEROSOL INLET PARTICLE LOSS ESTIMATES

The R/V *Investigator* has a custom-designed aerosol sampling inlet, with the intake located approximately 18.4 m above sea level at the bow of the ship. The whole inlet is stainless steel, with an inner diameter of 16 cm. Ambient air is sampled into a conical intake section at ~1800 L min^{-1}, which is oriented horizontally to limit the amount of precipitation entering the inlet, and automatically adjusts to orient into the wind (forward 90° only). The inlet then travels vertically down the foremast into the aerosol lab, which is located directly underneath the inlet at the bow of the ship, so as to minimize particle losses. Inside the aerosol lab, approximately 9 m

from the intake, is a sample manifold with instrument pickoffs for aerosol sampling. All aerosol instruments considered in this study were located inside the aerosol lab and sampled from the aerosol sampling manifold.

Particle transmission efficiency through the aerosol sampling inlet, including dependence on wind speed and ship motion, has not been fully characterized. Preliminary theoretical calculations of transmission efficiency for the CFDC, APS, and WIBS are shown in Figure 2.6, which utilized the von der Weiden et al. (2009) Particle Loss Calculator and Paul Baron's Aerocalc spreadsheet (Brockmann 2011). These calculations assumed a constant aspiration angle of 0°, a wind velocity of 10 m s^{-1}, which is the average for the CAPRICORN-2 campaign, a particle density of 1300 kg m^{-3}, and a shape factor of 1 (see Section 2.2.4.5). The calculated transmission efficiency of particles through the co-located aerosol concentrator inlet is also shown.

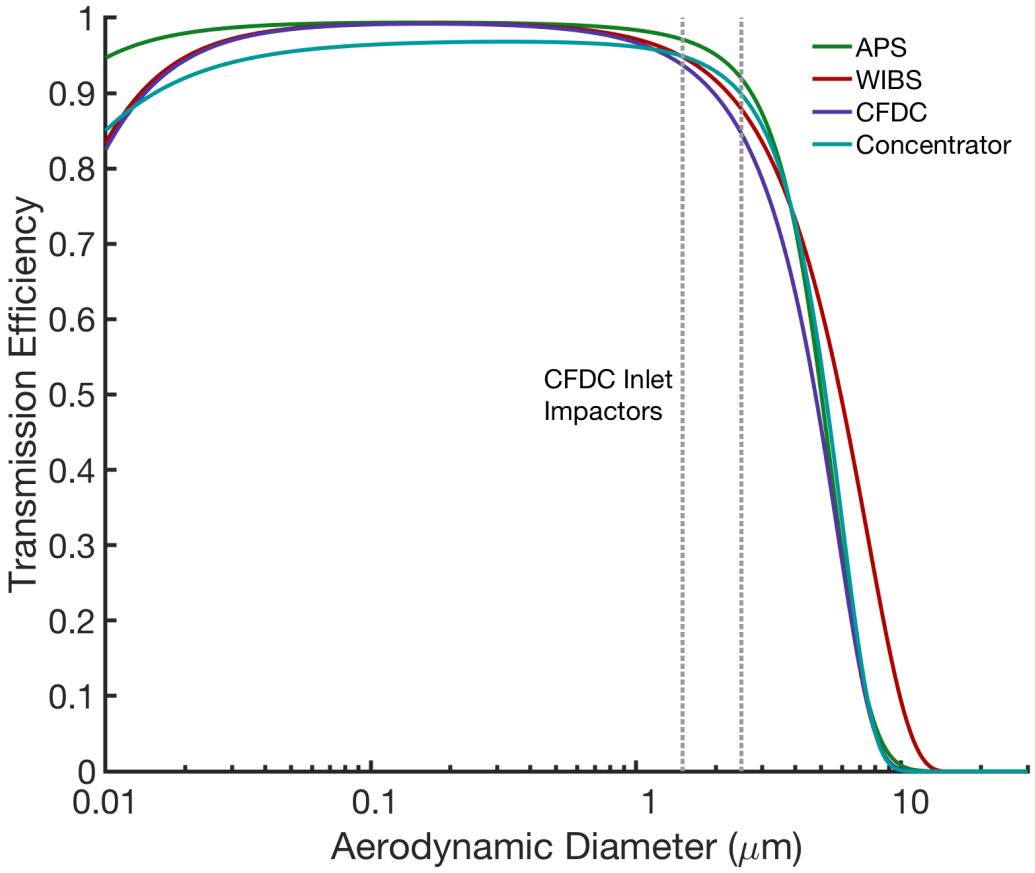

Figure 2.6: Theoretical calculations of particle transmission efficiency during CAPRICORN-2 as a function of particle aerodynamic diameter.

The 50% cut sizes of the two different inlet impactors used for the CFDC (1.5 or 2.4 μm aerodynamic diameter) are shown in Figure 2.6 as dashed gray lines. Particle transmission efficiency is predicted to be greater than 85% for particles <2.5 μm, so no corrections were applied to INP concentrations measured using the CFDC. Similarly, particle transmission is estimated at >95% for submicron particles, so no corrections were applied to the SMPS number concentrations. The WIBS and APS number concentrations were scaled to account for predicted particle transmission for sizes up to 10 μm and 7.5 μm, respectively. Above this, the expected transmission efficiency drops below 10%, making the correction highly uncertain, and so only particles smaller than 10 μm (WIBS) or 7.5 μm (APS) were considered in this study. The nephelometer measures bulk aerosol scattering, and as the particle transmission efficiency is highly size dependent for supermicron aerosols, which are expected to dominate the scattering signal, no corrections were applied to the nephelometer data presented here.

2.4 R/V *INVESTIGATOR* SHIP EXHAUST FILTERING

The largest sources of particle contamination on board the R/V *Investigator* are exhaust from diesel combustion from the engines and waste incineration. These waste streams are emitted from separate but co-located flues approximately 50 m aft of the aerosol intake, and at a similar height as the inlet (Humphries et al. 2019). Following the technique presented in Humphries et al. (2019), Ruhi Humphries (CSIRO) developed a timeseries for the CAPRICORN-2 voyage indicating periods when ship exhaust are predicted to have influenced aerosol measurements. For the CAPRICORN-2 voyage, no black carbon measurements were available, so only carbon monoxide, carbon dioxide, and particle number concentration were used to generate the exhaust timeseries. This timeseries was used to filter the APS, SMPS, WIBS, and nephelometer data to exclude periods when measurements are likely to include ship exhaust. The CFDC data were not filtered, as previous measurements have indicated very low IN efficiency of particles emitted from diesel engines (Schill et al. 2016), and inspection of INP concentrations showed no significant differences between adjacent measurements when one was influenced

by ship exhaust and the other was not (Figure 2.7). This is consistent with previous ship-board measurements for temperatures above -26 °C (McCluskey et al. 2018c; Irish et al. 2019). As mentioned previously, the IS filter pumps were controlled by a sector sampler (Section 2.2.3), which shut off power to the pumps when ship exhaust was expected to influence measurements, so no corrections were made to the INP concentrations measured using the IS either.

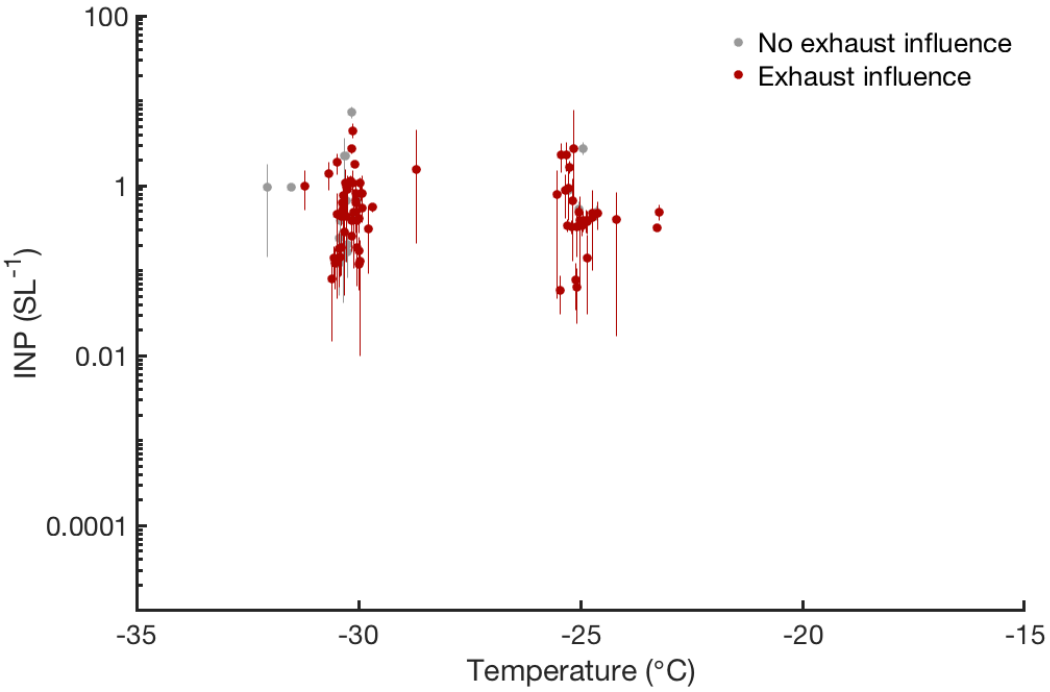

Figure 2.7: CFDC measurements made on the R/V *Investigator*, with and without the influence of ship exhaust.

2.5 REAL-TIME ICE NUCLEATING PARTICLE MEASUREMENTS

The operation of the CFDC was described in Section 2.2.1, but briefly, ambient gas and aerosols are dried, large particles are removed (using single-jet impactors with either a 1.5 or 2.4 μm cutpoint), and the aerosols are then passed into a vertically-oriented chamber between two ice-coated walls. A steady-state RH and temperature are maintained within the chamber, in the range of 104-106% RH and -25 and -33 °C during this study. Operating in the water-supersaturated regime forces cloud-droplet activation prior to freezing, which gives results that

compare well to offline immersion freezing techniques (DeMott et al. 2016). An optical particle counter is used to detect particles as they exit the chamber, and ice crystals are distinguished from aerosols and any remaining water droplets by their larger size. The upstream jet impactors are required for this optical separation, so that large aerosols and cloud droplets are not included in INP concentrations. For CAPRICORN-2, and as a special emphasis for this thesis, a new semi-automated graphical user interface (GUI) has been developed to increase speed and reproducibility of CFDC data analysis (Section 2.5.1). Determination of statistical significance of data has also been improved and will be discussed in Section 2.5.3.

CFDC's are typically operated in alternating 5-20 min periods of ambient or laboratory sampling and sampling filtered air, which is used to estimate instrument frost background. Due to the large thermal and vapor pressure gradients between the two chamber walls, water vapor continuously sublimates from the warmer wall and deposits on the colder wall, eventually leading to frost crystals growing on the cold wall and rough or ice-free regions on the warmer wall (Rogers et al. 2001). Ice fragments from this process can break off the walls and fall into the air stream, and are then detected by the OPC. This occurs at two different frequencies- intermittent, low concentration events that are accounted for by comparing ambient/laboratory measurements with measurements of filtered air (Section 2.5.3), and short, infrequent, high concentration events which are detected and removed prior to any other analysis (Section 2.5.2).

Once data are corrected for frost, their statistical significance is determined (Section 2.5.3), and then any other relevant corrections or calculations are performed. During CAPRICORN-2, the CFDC alternately sampled directly from the R/V *Investigator* aerosol inlet and from an aerosol concentrator (see Section 2.2.2). The aerosol concentrator concentrates particles >0.5 μm aerodynamic diameter (Figure 2.3), which can increase measurement statistics and lower the CFDC detection limit, assuming the mode size of INPs is greater than 0.5 μm (Tobo et al. 2013; McCluskey et al. 2018c). INP concentration measurements collected using the aerosol concentrator were scaled based on adjacent measurements made using the ambient inlet (Section 2.5.4). The last calculation that will be discussed here is the ice nucleation surface active

site density, n_s (Section 2.5.5), which is a common way to parameterize INP concentrations in global models (see Niemand et al. 2012; Ullrich et al. 2017; McCluskey et al. 2018a).

2.5.1 Graphical User Interface for CFDC Analysis

A new GUI to aid in CFDC data analysis was developed in MATLAB (MATLAB 2019) and has been validated using the CAPRICORN-2 data set and laboratory measurements spanning a range of temperatures (-25 to -60 °C) and aerosol types. During measurements, an automated 3-way valve is used to vary the CFDC inlet between closed, open to ambient/lab air, and filtered/background air. The position of this valve is recorded at 1 Hz intervals and used by the GUI to generate a list of times when the CFDC was sampling or measuring background. Any of these periods that are less than 20 s in length are removed from the data set and not considered further. The GUI then sequentially displays integrated particle counts from the OPC (L^{-1}), water supersaturation (SS_w, %), total flow rate ($L\,min^{-1}$), and pressure within the chamber (mb) for each filter and sample period within the dataset (Figure 2.8). For each period, the user will have the option to keep or remove the period from further analysis, select the portion of the period to use in INP concentration calculations, and to set whether an aerosol concentrator was used for this measurement. In the future, this will be expanded to analysis of CFDC aircraft data, where multiple inlet types (HIMIL, SDI, CVI) will be able to be selected by the user, and the relevant corrections for particle transmission efficiency or concentration will be applied automatically.

Once the user has selected all the data they wish to use in further analysis, the OPC particle counts as a function of bin number, which is correlated with particle size, is shown as a histogram for the aggregated sample data (Figure 2.9). The user can then adjust the threshold which will be used to distinguish ice crystals from aerosols when calculating INP concentrations. Optional parameters can be set to remove data points outside of a user-selected range of SS_w and instrument flow rates. This is to allow the user to automatically eliminate data when the instrument isn't operating in the desired immersion freezing mode (outside of SS_w limits), or not at operating conditions (flow rate outside limits). For CAPRICORN-2, the upper and lower

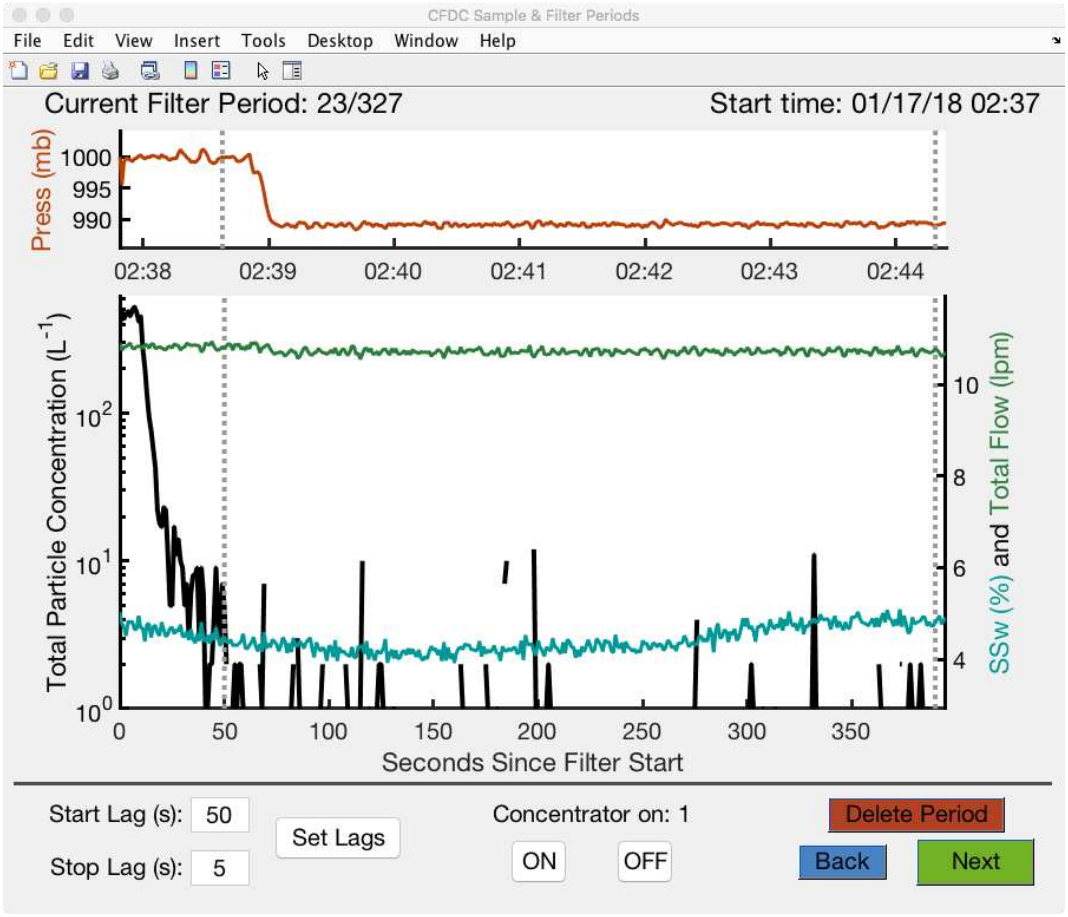

Figure 2.8: Example filter period from the CAPRICORN-2 CFDC dataset demonstrating the newly-developed GUI. The vertical dashed gray lines represent the currently selected bounds for data that will be used in further analysis.

SS_w limits were set to 2% and 9%, respectively, and the minimum allowable flow was set to 2 std L min^{-1}. No data were removed using these automated limits for this study. Bin 165 was used as the threshold for separating ice crystals from aerosols, as has been done in previous studies. The aggregated particle count histogram for the CAPRICORN-2 CFDC dataset is shown in Figure 2.10.

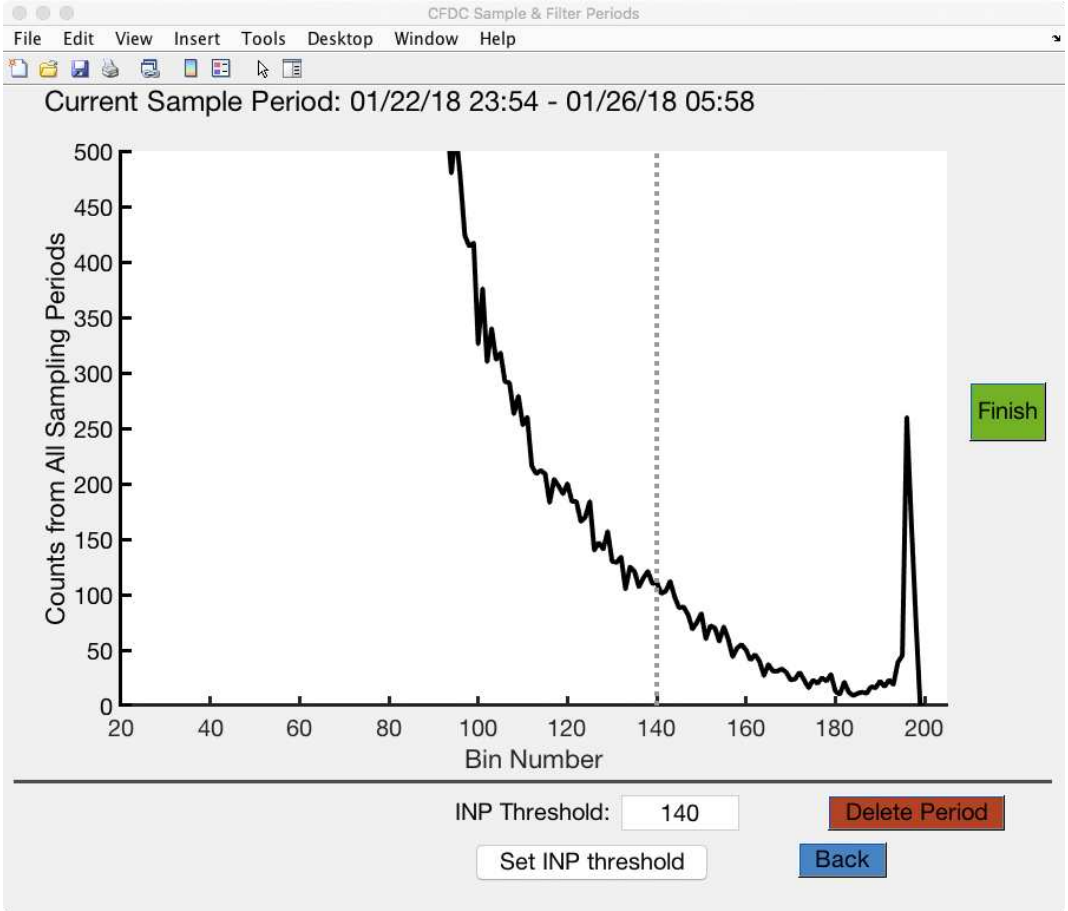

Figure 2.9: Example OPC histogram from the CFDC analysis GUI. The vertical dashed line shows the current threshold for separating ice crystals from aerosols.

2.5.2 Removing Large Frost Spikes from CFDC Data

The detection of infrequent, high intensity frost events is accomplished by using a modified extreme Studentized deviate (ESD) test to find outliers (Martel 2015). The traditional technique applies to data that are approximately normally distributed, so it has been modified to work

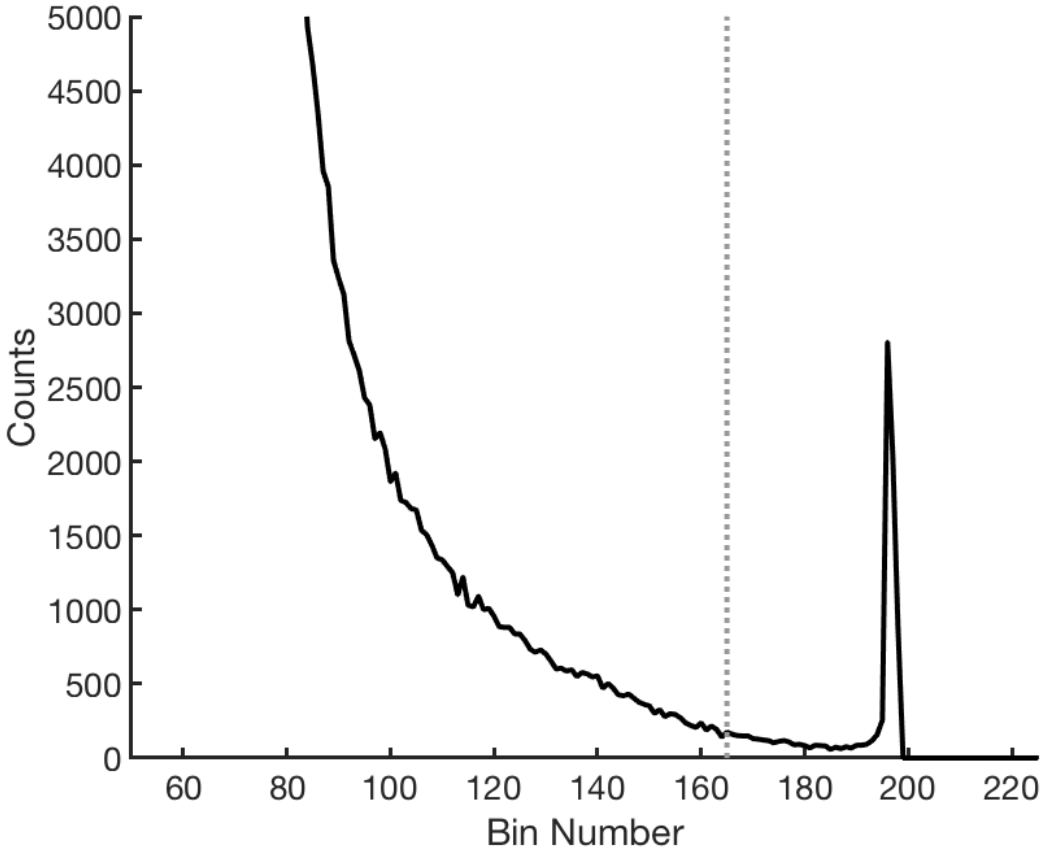

Figure 2.10: Aggregated particle count histogram for the CAPRICORN-2 CFDC dataset. The vertical dashed line represents the threshold used for distinguishing ice crystals from aerosols.

with count data that follow a Poisson distribution. For each filter and sample period in the dataset, an iterative process is used to find points where the ice crystal detection rate (s^{-1}) exceeds a user-selected percentile of the Poisson distribution. Points that exceed this threshold are considered outliers and are removed from the dataset, as well as the 10 second period centered at the outlier.

For each sample or filter period, the overall Poisson rate (ice crystals s^{-1}) is calculated. Then, the percentile used to separate outliers is defined as follows:

$$p = 1 - \frac{\alpha_{frost}}{n - j + 1}, \tag{2.5}$$

where α_{frost} is the user-selected significance level, n is the number of observations in the period, and j is the current iteration number. The rejection threshold for outliers is then determined by inverting the Poisson distribution, using the calculated rate and percentile. If any points in the period exceed the rejection threshold, they are considered outliers and removed from the dataset. The whole process is repeated until no remaining points exceed the rejection threshold, or the rejection threshold is ≤2 ice crystals s^{-1}. If any outliers were detected during this process, any points within ±5 s of each point are also removed. For the CAPRICORN-2 dataset, a significance level of $\alpha_{frost} = 0.001$ was used to find outliers.

2.5.3 Background Correction and Significance Testing for CFDC Data

The low concentration, intermittent frost events are corrected for by comparing ambient or laboratory measurements of aerosols with measurements of filtered air. As this background is sensitive to the RH and temperature within the chamber, as well as the length of time the instrument has been running, background measurements of filtered air are typically collected for 5 minutes of every 15, alternating with measurements of the sample of interest. The background correction and significance testing method developed recently follows Krishnamoorthy and Lee (2013), which improves estimates of significance and confidence intervals for the difference between two Poisson distributions over previous techniques.

For each sample period in the dataset, the closest filter periods (in time) are found that bracket the sample period, and the background data from these periods are combined. First, the total number of ice counts (N_s and N_f) and length in seconds (t_s and t_f) are calculated for the sample and combined filter periods. Next, the Poisson rate parameters corresponding to the sample and background are calculated as:

$$\hat{\lambda_s} = \frac{N_s}{t_s} \qquad \text{and} \qquad \hat{\lambda_f} = \frac{N_f}{t_f} \tag{2.6}$$

The moment-based Z-statistic for the difference between the sample and background Poisson distributions is then given by (Krishnamoorthy and Lee 2013):

$$Z_m = \frac{\hat{\lambda_s} - \hat{\lambda_f}}{\sqrt{\hat{\lambda}\left(\frac{1}{t_s} + \frac{1}{t_f}\right)}} \qquad \text{where} \qquad \hat{\lambda} = \frac{N_s + N_f}{t_s + t_f} \tag{2.7}$$

The sample period is significantly different from the background if Z_m is greater than $Z_{1-\alpha/2}$ for the desired significance level. For this study, $\alpha = 0.1$ and $\alpha = 0.2$ were used to determine significance at 80% and 90% for a 2-tailed Z-test. The background-corrected INP concentration is then given by $\hat{\lambda_s} - \hat{\lambda_f}$. Confidence intervals for the appropriate significance level are calculated using (Krishnamoorthy and Lee 2013):

$$\hat{\lambda_s} - \hat{\lambda_f} + \frac{Z^2_{1-\alpha/2}}{2}\left(\frac{1}{t_s} - \frac{1}{t_f}\right) \pm Z_{1-\alpha/2}\sqrt{\left(\frac{\hat{\lambda_s}}{t_s} + \frac{\hat{\lambda_f}}{t_f}\right) + \frac{Z^2_{1-\alpha/2}}{4}\left(\frac{1}{t_s} - \frac{1}{t_f}\right)^2} \tag{2.8}$$

The INP concentrations and confidence intervals are then converted into std L^{-1} (SL $^{-1}$ from here on out) using the average aerosol flow rate during the sample period.

2.5.4 Scaling INP Concentrations Measured Using the Aerosol Concentrator

As described in Section 2.2.2, an aerosol concentrator was used during CAPRICORN-2 to pre-concentrate particles with diameters >0.5 μm prior to measurement of INPs using the

CFDC. For each measurement made using the concentrator, a concentration factor was calculated by comparison to ambient measurements made within an hour, if available (Figure 2.11). For each day of the campaign, an average INP concentration factor was calculated and applied to all the concentrator measurements. For days where concentration factors were unable to be calculated, the median concentration factor from the campaign, 4.84, was applied. The confidence intervals for these measurements were adjusted so the width represents the same proportion of the corrected value as of the original measurement. INP concentrations measured at

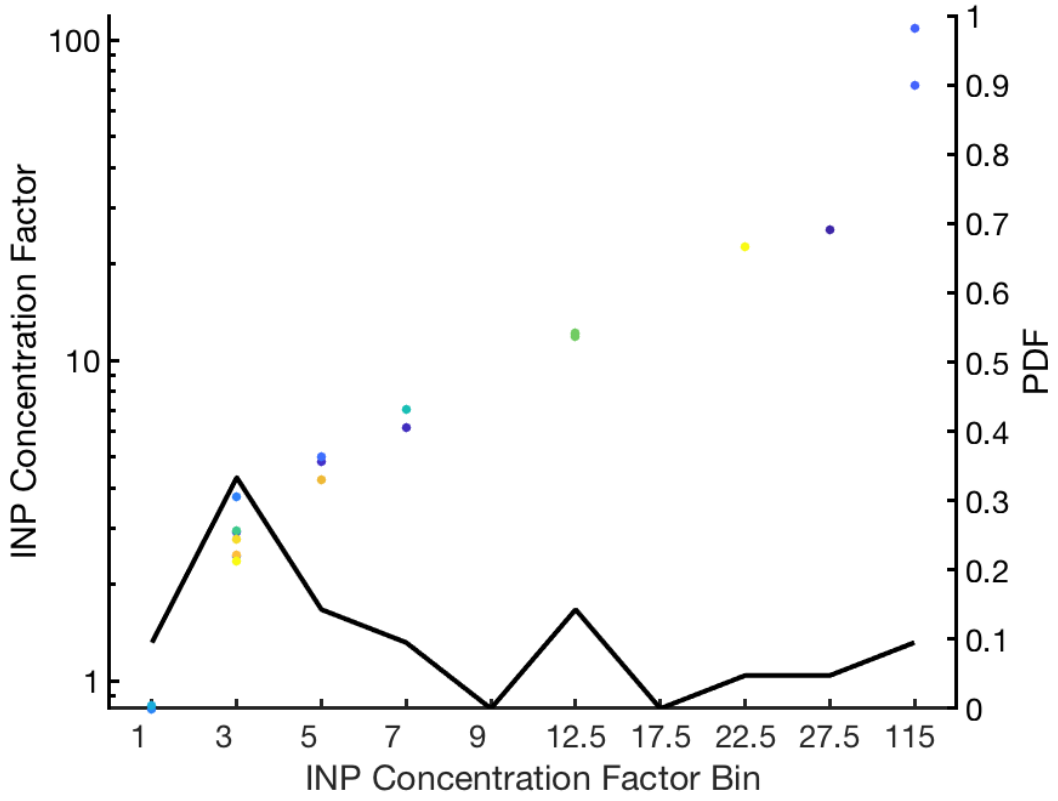

Figure 2.11: Concentration factors of INPs measured with the aerosol concentrator during CAPRICORN-2 are shown as colored dots on the left axis, and the probability distribution function (PDF) of concentration factors is shown in the solid black line on the right axis.

adjacent periods using the aerosol concentrator and the ambient inlet are shown in Figure 2.12 after scaling the aerosol concentrator measurements as described above. Good agreement was found between ambient observations and the scaled aerosol concentrator measurements.

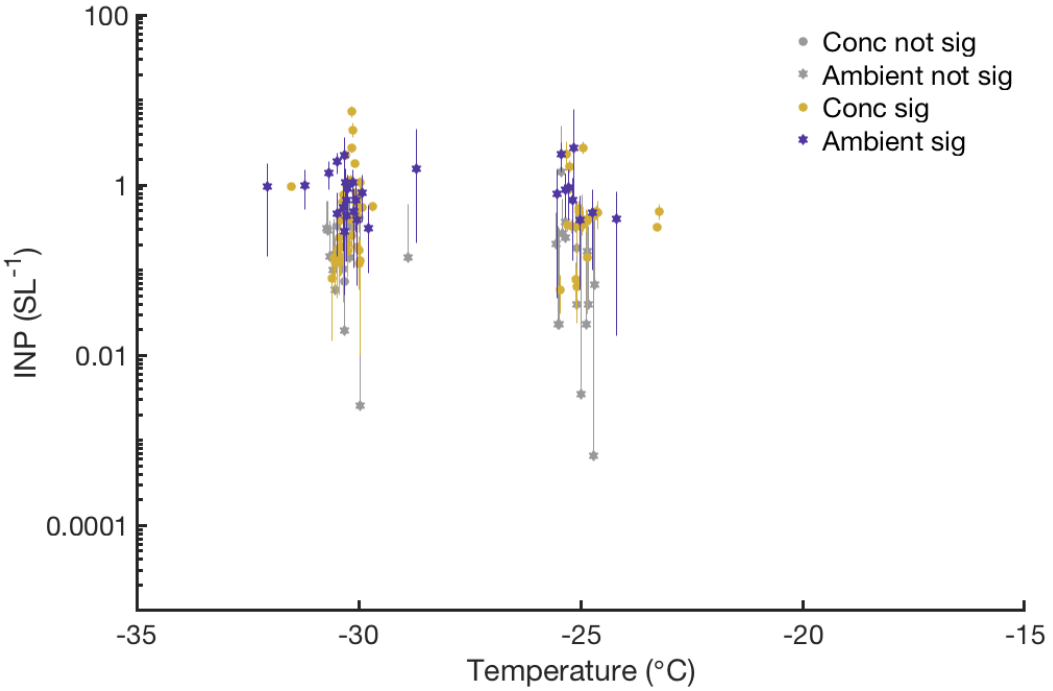

Figure 2.12: Comparison of INP concentrations measured using the aerosol concentrator and ambient inlet. Colored symbols represent data that is statistically significant, and gray symbols represent non-significant data.

2.5.5 INP Surface Active Site Density Calculation

One way in which ice nucleation is represented in global models is through a parameterization known as the surface active site density, n_s, which is the number of ice-active sites per aerosol surface area (Niemand et al. 2012). This metric predicts heterogeneous ice nucleation as a function of temperature using total aerosol surface area as a normalization variable:

$$n_s = \frac{n_{INP}}{SA_{tot}} \tag{2.9}$$

This metric was calculated for the CAPRICORN-2 dataset using the average aerosol surface area measured by the SMPS and APS for the same time periods as CFDC measurements or IS filters. CAPRICORN-2 n_s values will be compared to previous studies (Niemand et al. 2012; Ullrich et al. 2017; McCluskey et al. 2018a), and the utility of this parameter for parameterizing Southern Ocean INPs will be discussed in Section 5.

3. Results: Southern Ocean Marine Boundary Layer Aerosols and Ice Nucleating Particles

3.1 MARINE AEROSOL OBSERVATIONS DURING CAPRICORN-2

Marine boundary layer measurements of clouds and aerosols were conducted during Jan.-March 2018 on the R/V *Investigator* as part of the CAPRICORN-2 field campaign (Figure 2.1). A timeseries of aerosol size distributions from 15 nm to 5 μm is shown in Figure 3.1, which was constructed by merging the APS and SMPS measurements (Section 2.2.4.1). Three modes are

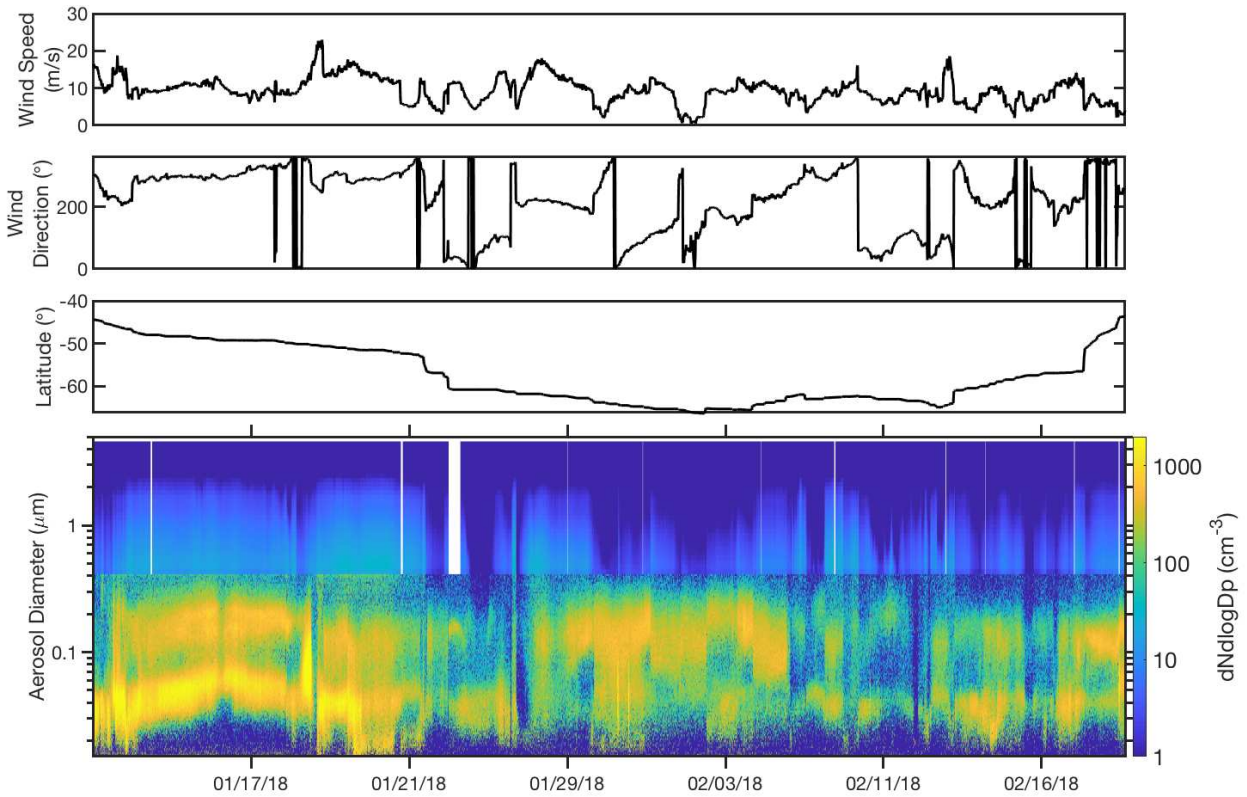

Figure 3.1: Timeseries of wind speed and direction, latitude, and aerosol size distributions during CAPRICORN-2. Periods identified as exhaust have been removed and are not shown.

clearly visible- an Aitken mode centered at ~40 nm, an accumulation mode centered at ~150 nm, and a supermicron coarse mode. A distinct Hoppel minimum (Hoppel et al. 1990; 1994)

at ~70-80 nm is present between the Aitken and accumulation modes, indicating that cloud processing of MBL aerosols is widespread in this region. The aerosol number concentration during CAPRICORN-2 averaged 314 cm^{-3}, and was dominated by the Aitken and accumulation modes. These results are consistent with observations from ACE-SPACE (Schmale et al. 2019) and the trial voyage of the R/V *Investigator* in 2015 (Alroe et al. 2019) during periods identified as originating in the Southern Ocean MBL.

Median aerosol size distributions in 5° latitude bins between -45° and -65° are shown in Figure 3.2. Aitken, accumulation, and coarse modes appear in all distributions, however, the relative contribution of the Aitken mode to total aerosol number decreases with latitude. The

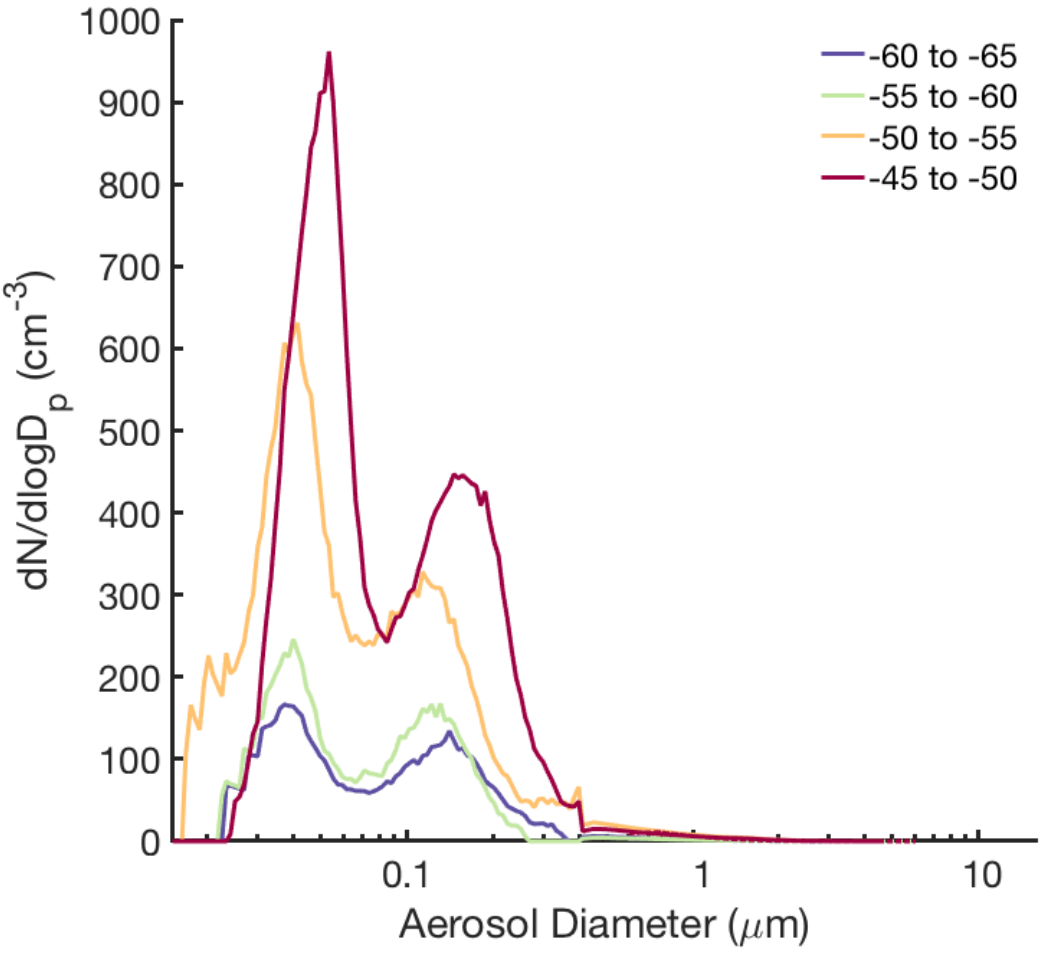

Figure 3.2: Median aerosol size distributions from CAPRICORN-2 in 5° latitude bins between -45° and -65°.

mode size of the Aitken and accumulation modes, as well as the position of the Hoppel minimum is relatively constant poleward of -50°, and slightly larger in the band between -45° and -50°. These differences in aerosol number and size may relate to varying source region productivity, particle composition, wind speed, particle removal rates, and cloud supersaturations in the latitude bands. The contribution of the coarse mode to total particle number is small at all latitudes, though it has a strong correlation with wind speed (Figure 3.3) indicating the coarse mode is dominated by primary SSA, as expected (Lewis and Schwartz 2004). Accumulation mode particle number concentration has a more complicated relationship with wind speed (Figure 3.4), which reflects the multiple sources influencing particle number in this mode, including primary emissions, atmospheric oxidation, condensation, and cloud processes.

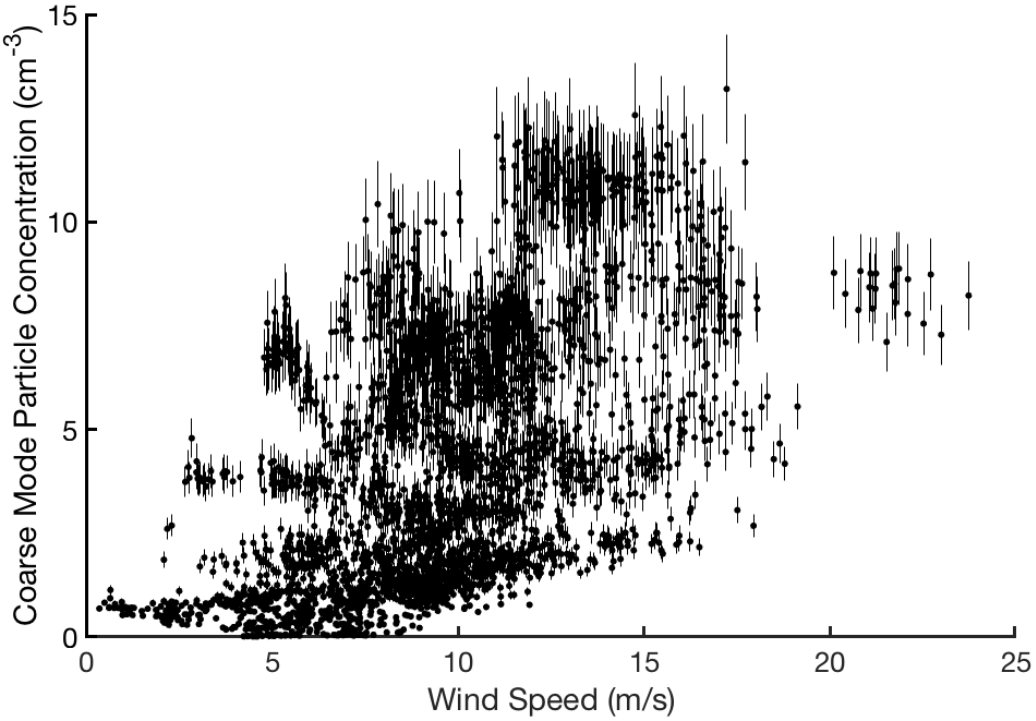

Figure 3.3: Relationship between coarse mode aerosol number and wind speed.

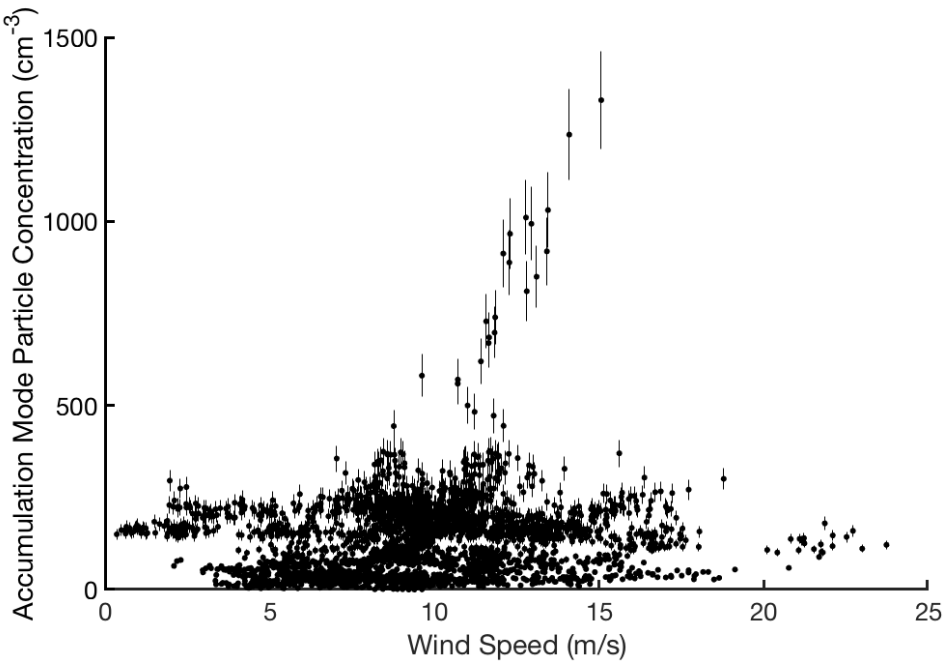

Figure 3.4: Relationship between accumulation mode aerosol number and wind speed.

3.2 ICE NUCLEATING PARTICLE OBSERVATIONS DURING CAPRICORN-2

Until the CAPRICORN-1 cruise in 2016, the only reported INP observations from the Southern Ocean region were those of Bigg (1973) and Bigg (1990). This paucity of information has made it difficult to evaluate modeling studies such as Burrows et al. (2013), which suggested marine organic aerosols dominate the INP number concentration in this region. Recent voyages (CAPRICORN-1, Tangaroa-2015, MARCUS, CAPRICORN-2, Tangaroa-2018, ACE-SPACE) and aircraft campaigns (SOCRATES) have dramatically increased the number of observations of INPs and of cloud ice over the Southern Ocean, and may improve our understanding of cloud-aerosol interactions in this remote marine environment. Marine boundary layer measurements of INPs active at -20 °C from four recent campaigns led by our research team at CSU are shown in Figure 3.5, as well as the measurements made during 1969-1972 voyages by Bigg (1973). The INP number concentrations at -20 °C from CAPRICORN-2 and SOCRATES are consistent with other modern measurements (McCluskey et al. 2018c; Schmale et al. 2019; unpublished results from MARCUS and MICRE campaigns) but are more than two orders of magnitude lower than Bigg (1973). Bigg (1990) reported a dramatic decrease in SO INP concentrations at -15 °C be-

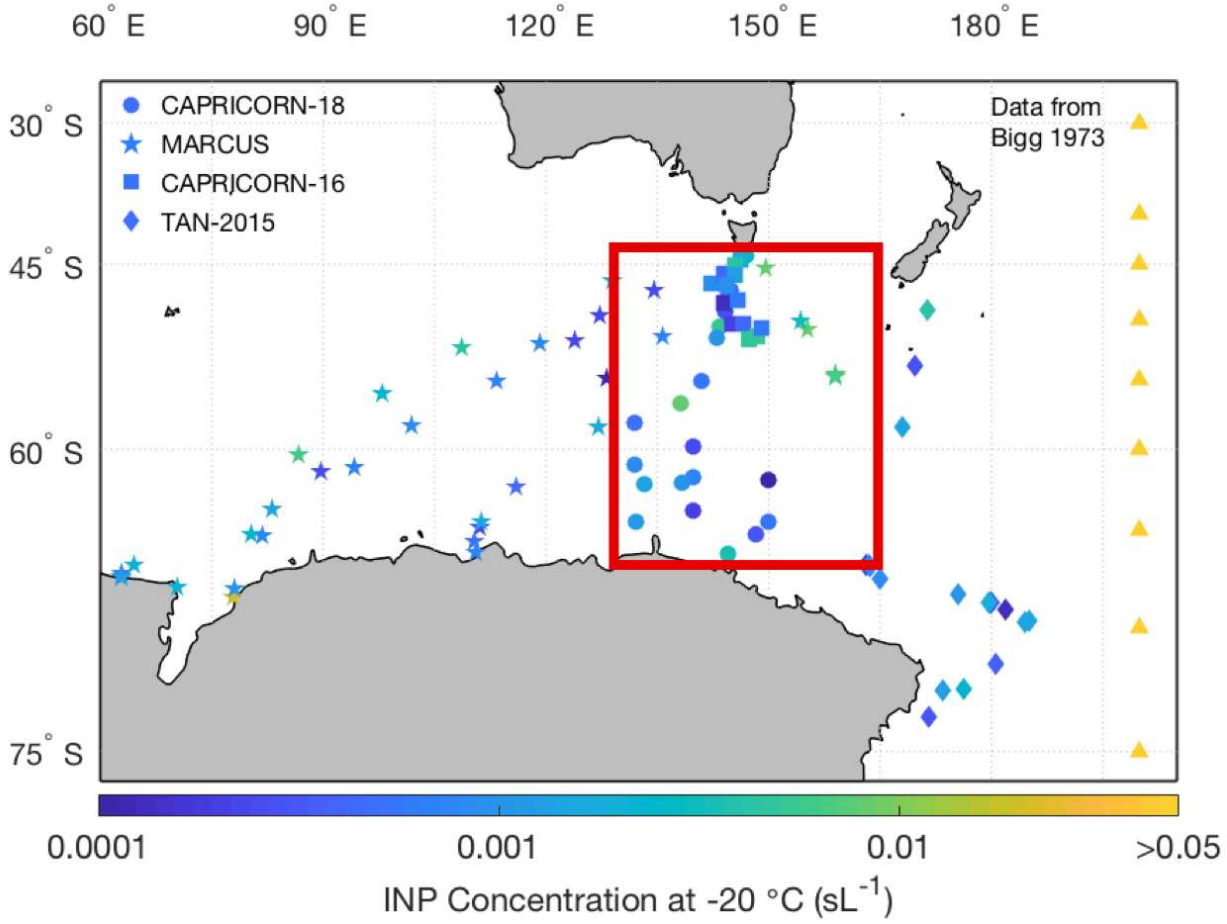

Figure 3.5: Observations of recent measurements of INPs at -20 °C over the SO along with those of Bigg (1973). The red box represents the region covered by CAPRICORN-2 and SOCRATES.

tween the 1969-1972 and 1988 measurements, from 7.5±2.3 m^{-3} to 0.2±0.02 m^{-3}, with the 1988 results in line with recent observations. McCluskey et al. (2018c) re-analyzed Bigg's 1969-1972 results and posited that contamination alone could not explain the differences between the INP concentrations reported in Bigg (1973) and those from 1990 to the present, despite the dramatic improvements in sample collection and handling techniques during that period. The decline in SO INP concentrations is coincident with a step-change decrease in dust emissions from Australia that occurred in the early 1970s (personal communication with P. Ginoux, NOAA GFDL, 2019), which may explain gross differences in INP populations over the SO during the 1960s versus modern day. Dust deposition to the Southern Ocean is generally low and episodic (Jickells et al. 2005), but mineral dust is a highly efficient ice nucleator (Niemand et al. 2012; Ullrich et al. 2017; DeMott et al. 2015), and even low dust levels can significantly enhance INP concentrations if present.

Bigg (1973) noted a strong latitudinal (Figure 3.6a) and seasonal trend in the concentration of INPs , which was more pronounced for INPs that activate at warmer temperatures, especially -10 °C. INP concentrations during CAPRICORN-2 were below detection limit at -10 °C, despite the large volumes of air sampled (10.6 to 63.7 m^3), so only results for -15 °C and colder are shown. No strong latitudinal trend was observed in CAPRICORN-2 at any temperature (Figure 3.6b), although the observations excluded latitudes around -40° and -70°, where Bigg (1973) observed the largest maximum and minimum in INP concentrations, respectively. Smaller sample size, seasonal variation, changes in INP source, or variability in weather systems and atmospheric transport may all contribute to these differences.

Temperature spectra of IS filters from CAPRICORN-2 are shown in Figure 3.7, along with CFDC measurements at their respective temperatures. For reference, the IS filter and CFDC data range from CAPRICORN-1 (McCluskey et al. 2018c), and the ACE-SPACE filter measurement range (Schmale et al. 2019) are also shown. The CAPRICORN-2 measurements agree well with the other recent campaigns, although the mean concentrations are lower for all temperatures above -28 °C, and concentrations extend to much lower values at all temperatures. This

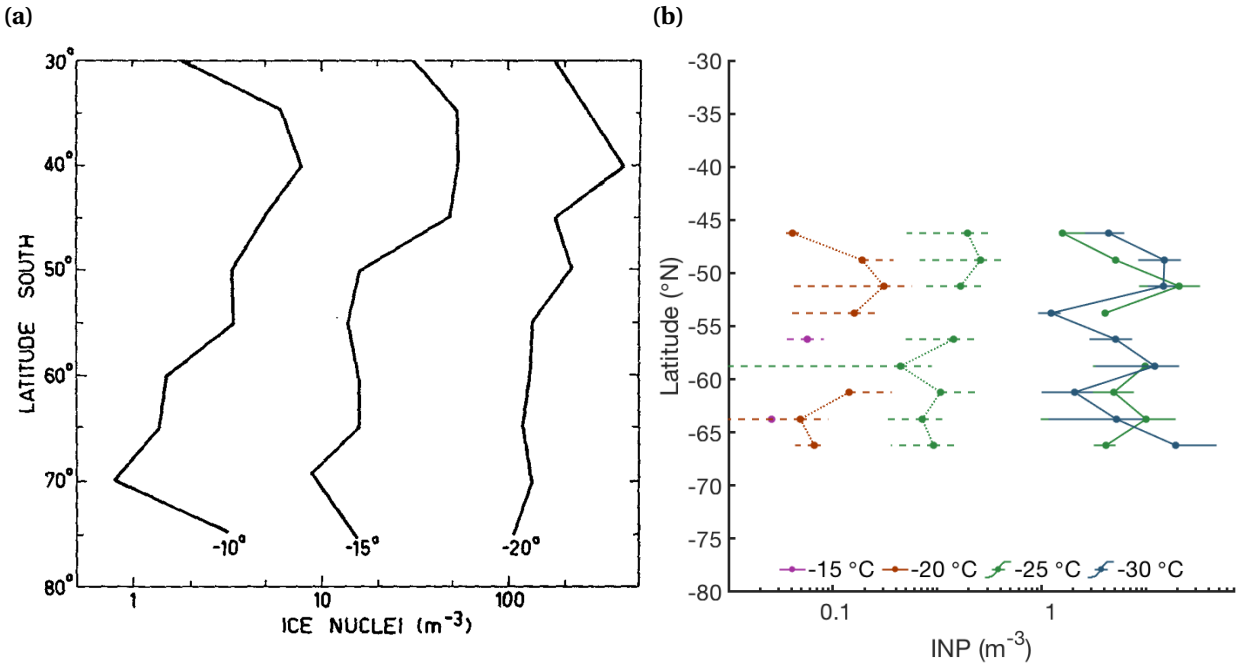

Figure 3.6: Latitudinal dependence of INP concentrations over the Southern Ocean from (a) Bigg (1973) and (b) CAPRICORN-2. In (b), IS filter measurements are represented by dashed lines and CFDC measurements by solid lines. Error bars are one standard deviation of all the measurements.

may represent seasonal or spatial variability between the campaigns, or simply the lower detection limits for CAPRICORN-2 than CAPRICORN-1 or ACE-SPACE. All of the Southern Ocean measurements are at or below the lower bound of concentrations reported for summertime Northern Hemisphere ocean regions (DeMott et al. 2016).

Filter measurements from CAPRICORN-2 included collection of particles up to at least 10 μm, while CFDC measurements only detected INPs smaller than 1.5 or 2.4 μm, depending on which upstream impactor was used (Section 2.2.1). No difference was observed in measured INP concentrations using either size of impactors, so all the CFDC data have been pooled in this analysis. Good alignment and overlap between integrated filter and real-time CFDC measurements suggests efficient transfer of aerosol sizes containing the majority of INPs to the CFDC, despite the relatively small maximum size (see additional discussion in Section 5). CFDC measurements at -25 °C are generally higher than filter measurements at the same temperature, which may be an indication of high-frequency variability in INP concentrations that aren't cap-

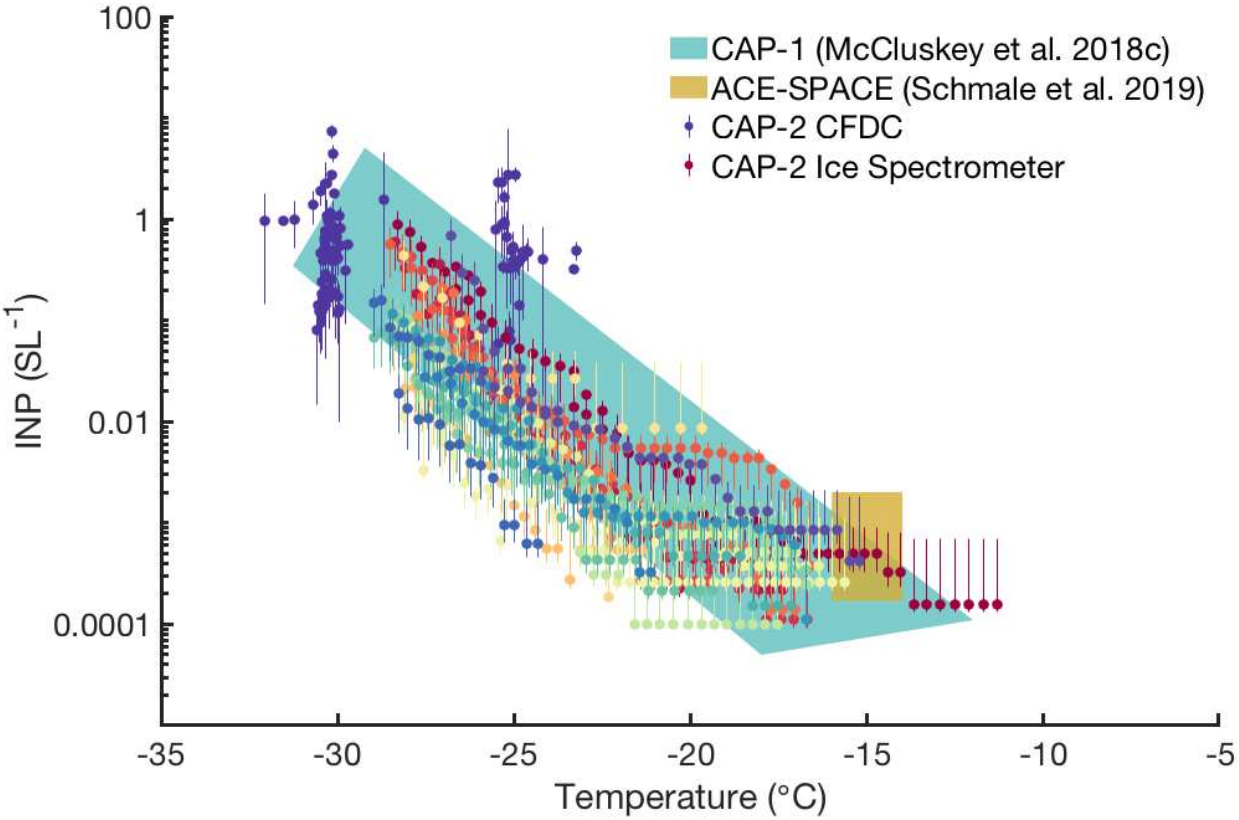

Figure 3.7: Temperature spectra of INP filter measurements and CFDC data from CAPRICORN-2. The range of CAPRICORN-1 CFDC and IS filter measurements are shown by the light blue shading (McCluskey et al. 2018c), and the interquartile range of the ACE-SPACE filter measurements are shown by the gold shading (Schmale et al. 2019).

tured by filter measurements that span 24-48 hours. Only the highest INP concentrations measured by the CFDC at -25 °C are statistically significant, as the frost background increases with temperature (Section 2.5.3), and so the lower concentrations captured by the filter measurements are not detectable by the CFDC. Some evidence of biological INPs can be seen in the filter spectra that deviate from a log-linear relationship at temperatures above -23 °C (Suski et al. 2018), which was not observed during CAPRICORN-1 (McCluskey et al. 2018c). Further compositional inferences will be possible after heat and peroxide treatments of filters (Section 2.2.3.1).

Normalization of INP concentrations using aerosol surface area or number concentration in order to parameterize ice nucleation in models will be discussed further in Section 4 and Section 5, but some preliminary results are shown here and compared to previously published observations. Aerosol surface area estimated from the SMPS and APS on the R/V *Investigator* during CAPRICORN-2 (Section 2.2.4.1) were used to obtain the ice nucleation active site density, n_s (Section 2.5.5) of SO INPs. Figure 3.8 indicates good agreement between CAPRICORN-2 n_s values and the marine aerosol parameterization developed by McCluskey et al. (2018a) in the North Atlantic, but the mean n_s values for CAPRICORN-2 are lower by about a factor of 5. Interestingly, despite the much larger latitude range sampled during CAPRICORN-2 than CAPRICORN-1, the n_s values agree well, although the more recent measurements extend to lower values. Some of these differences may be due to the different techniques used to estimate aerosol surface area for the two campaigns (see Section 4). Similarly to CAPRICORN-1, the n_s values from CAPRICORN-2 are lower than those of mineral dust by 3-5 orders of magnitude (Niemand et al. 2012; Ullrich et al. 2017). As discussed in McCluskey et al. (2018c), differences in average wind speed between the Northern and Southern Hemispheres and the subsequent changes in coarse mode aerosol number and surface area may strongly affect the n_s values. Variable aerosol composition as a result of biological activity may also alter ice nucleation efficiency of aerosols, but is not well understood.

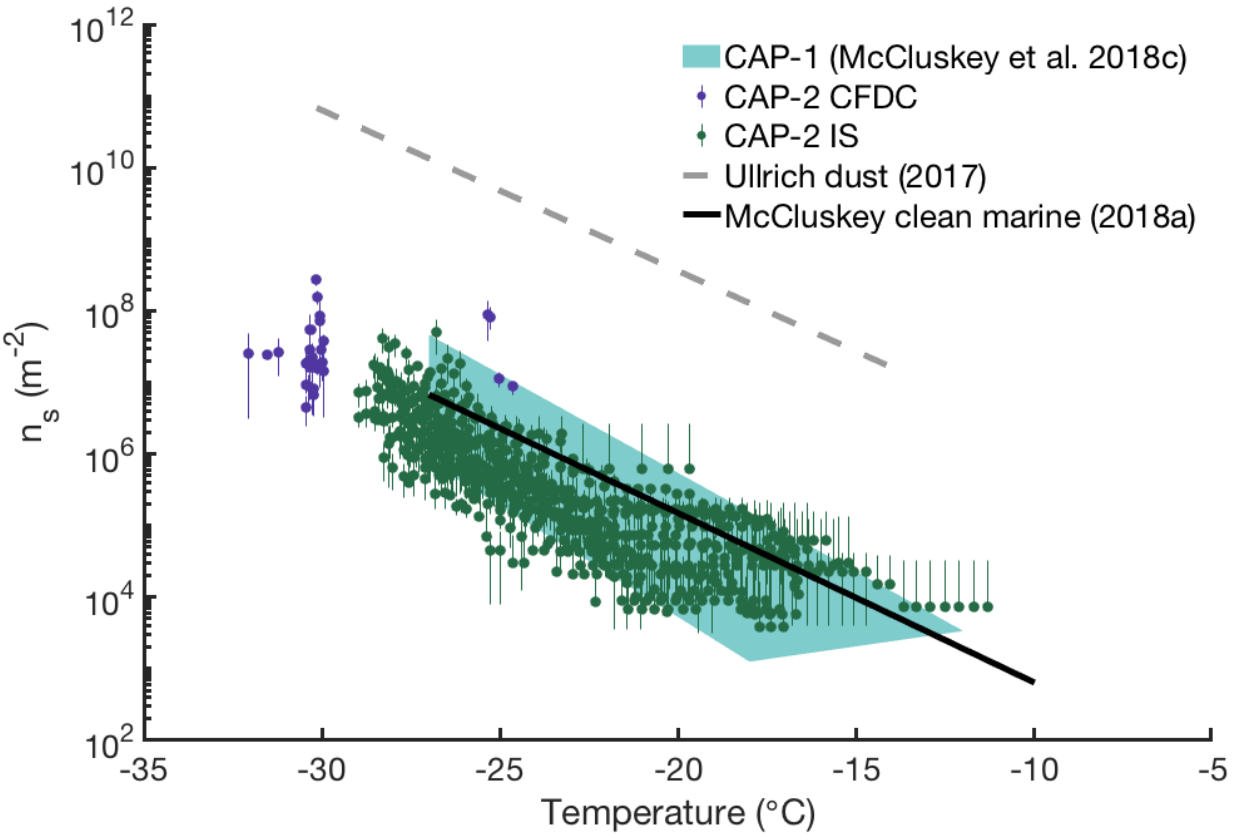

Figure 3.8: Ice nucleation active site density spectra of INP filter measurements and CFDC data from CAPRICORN-2. The range of observations from CAPRICORN-1 are shown by the light blue shading (McCluskey et al. 2018c). Parameterizations for clean marine aerosols (solid black line; McCluskey et al. (2018a)) and mineral dust (gray dashed line; Ullrich et al. (2017)) are shown for reference.

4. Results: Aerosol Surface Area Comparison

Estimates of aerosol surface area can be derived from a variety of measurements, including aerosol size distributions and particle scattering. All surface area estimates require different assumptions, such as particle density, hygroscopicity, and shape factor (see Section 2.2.4), and have different associated uncertainties. For cases where direct size distribution measurements are unavailable, scattering-derived surface area concentrations from a nephelometer may be used, as in DeMott et al. (2016) and McCluskey et al. (2018c). LIDAR-derived estimates, such as those presented in Mamouri and Ansmann (2016) are appealing because of their autonomous operation and the availability of measurements, although they are challenging to make in the Southern Ocean due to the requirements of clear-sky profiles and the possible lack of co-located direct aerosol measurements to validate conversion methods. In this chapter, aerosol surface area estimates from an SMPS and APS, WIBS, nephelometer, and LIDAR during CAPRICORN-2 are presented and compared. Surface area estimates from the SMPS and APS will then be used in Section 5 to compare parameterization schemes for ice nucleation in models. This comparison of different methods is presented here since comparability of these techniques would increase the ability to normalize INP data for many more places and times globally, for use in improving and validating models.

4.1 AEROSOL SURFACE AREA MEASUREMENTS FROM SMPS, APS, AND WIBS

Estimates of aerosol surface area were made during CAPRICORN-2 from aerosol size distribution measurements (Section 2.2.4.1 and Section 2.2.4.2), bulk aerosol scattering (Section 2.2.4.3), and particle backscatter coefficients (Section 2.2.4.4). The most direct measurements are from aerosol size distributions, using an SMPS, APS, and WIBS, although assumptions about particle sphericity, density, and hygroscopicity are required to convert aerosol number distributions into surface area distributions. Median aerosol number and surface area dis-

tributions in 5° latitude bins between -45° and -65° are shown in Figure 4.1, with logarithmic concentration scales to enhance the coarse mode values. The same Aitken and accumulation modes from Figure 3.2 are visible here, along with a coarse mode that extends from ~400 nm to supermicron sizes. Although the Aitken and accumulation modes dominate the total particle number concentration, the coarse mode dominates the surface area, with a significant contribution from the accumulation mode. The mode size (~1.5 μm) of the coarse mode is similar for all latitude bands, although the number of coarse mode particles peaks in the -50° to -55° range. The coarse mode is primarily SSA (Figure 3.3), and this enhancement of coarse mode aerosol is likely driven by the sustained high wind speeds observed between 1/15/18 and 1/19/18 (Figure 3.1). The WIBS undercounts coarse mode particles compared to the APS, particularly for particles ≥3 μm, possibly as a result of its low sample flow rate (0.5 L min^{-1}), which may result in increased coarse mode particle losses. As a result of undercounting, and its more limited size range, aerosol surface areas estimated from the WIBS data are lower than those calculated using the SMPS and APS size distributions.

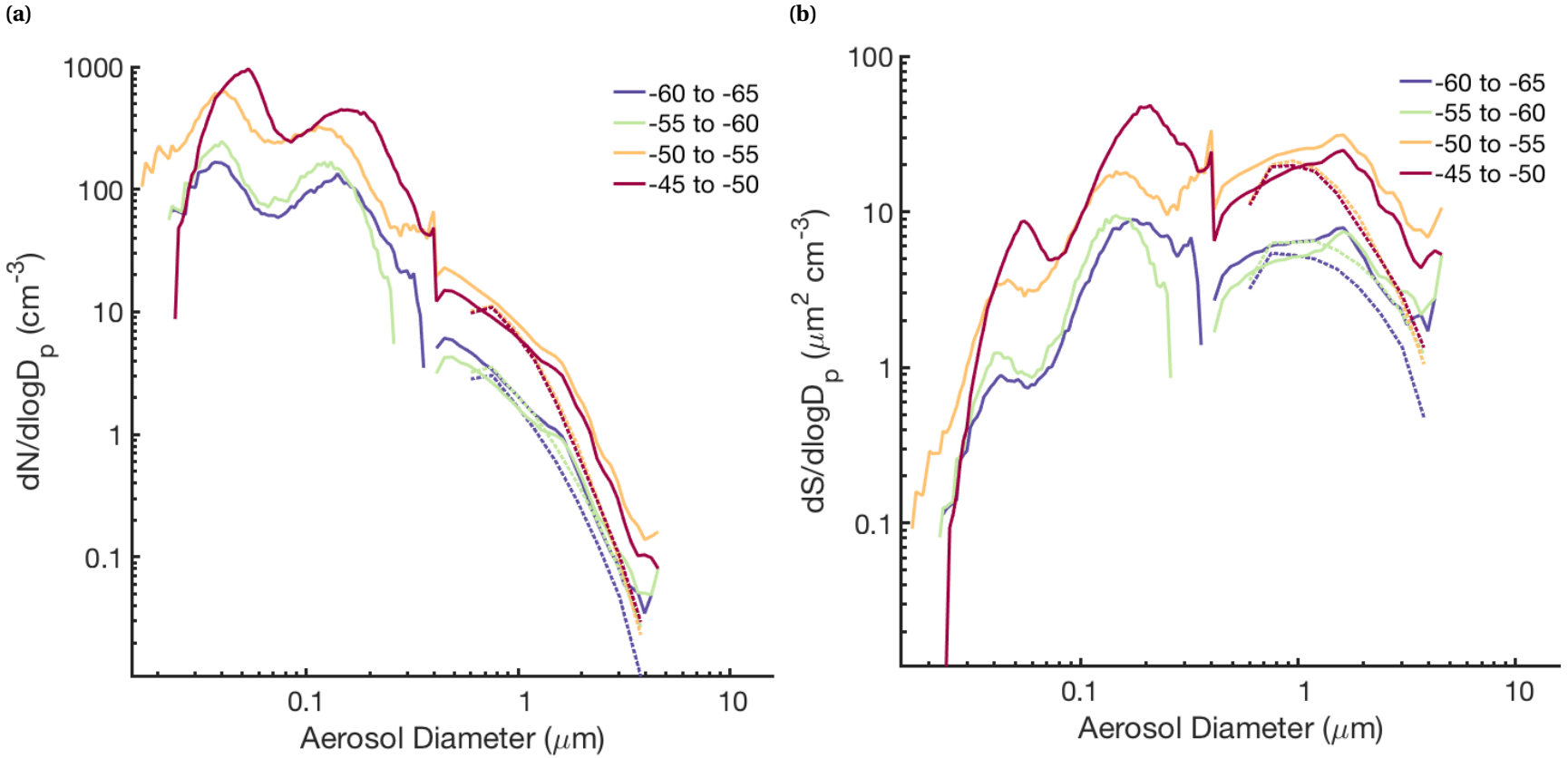

Figure 4.1: Median aerosol number (a) and surface area (b) distributions from CAPRICORN-2 in 5° latitude bins between -45° and -65° for the SMPS+APS (solid lines) and WIBS (dashed lines).

4.2 AEROSOL SURFACE AREA MEASUREMENTS FROM A NEPHELOMETER

Aerosol scattering measurements from the R/V *Investigator*'s nephelometer were also used to estimate particle surface area following DeMott et al. (2016) (Section 2.2.4.3), which requires the assumptions that particles are spherical, and they can be characterized as having a single effective scattering size. Measured scattering values at all three wavelengths are very similar (Figure 4.2), which is consistent with the scattering signal being dominated by supermicron particles. As a result, the calculated Ångstrom exponents are very small, with most of the values below 1, as is typical of SSA dominated by sea salt (Mulcahy et al. 2009). Some negative Ångstrom exponents were observed, which has been demonstrated previously for marine distributions dominated by supermicron sea salt under high wind speeds (Mulcahy et al. 2009). Due to this dominance of supermicron aerosols, the estimated scattering efficiency (Q) is almost always 2. Estimated aerosol surface area values range from 0.004 - 91.030 μm^2 cm^{-3}, with a mean of 22.928 μm^2 cm^{-3}.

4.3 AEROSOL SURFACE AREA MEASUREMENTS USING LIDAR

Following Mamouri and Ansmann (2016), Simon Alexander at the Australian Antarctic Division estimated vertical profiles of aerosol surface area from LIDAR backscatter coefficient measurements during CAPRICORN-2 (Section 2.2.4.4). Backscatter profiles were converted to aerosol extinction coefficients using the mean LIDAR ratio (S = 20 sr) observed during CAPRICORN-2 and the preceding CAPRICORN-1 voyage (Alexander and Protat 2019), and then to aerosol surface area using the marine aerosol conversion parameter presented in Mamouri and Ansmann (2016). This conversion parameter includes a correction for hygroscopic growth assuming $g_e(RH)$ ~2 at ~80% RH. LIDAR-estimated surface areas at 300 m are presented in Figure 4.3, as the LIDAR overlap function gives large uncertainites below this level. Profiles which include cloud cannot be used for this analysis, and were removed using Alexander and Protat's (2018) algorithm for detecting cloud boundaries using attenuated backscatter measurements.

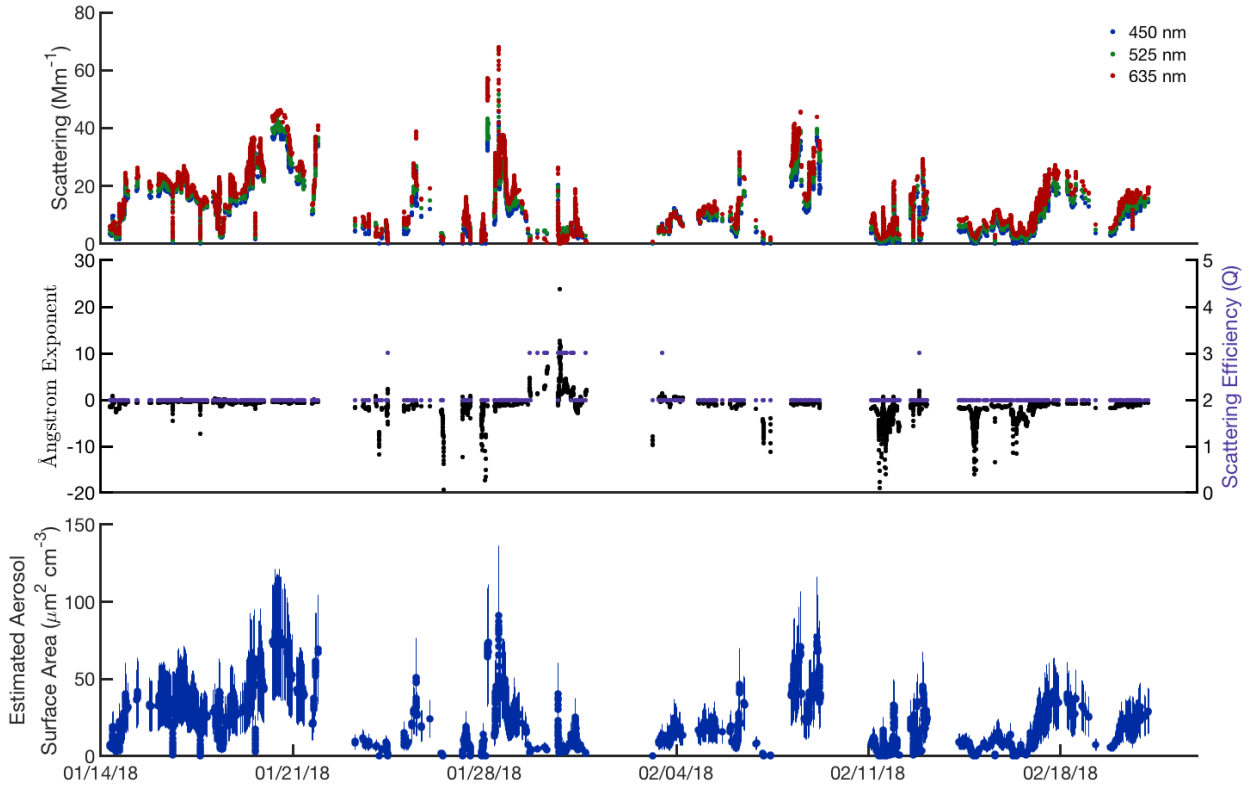

Figure 4.2: Timeseries of scattering (top), calculated Ångstrom exponents and scattering efficiency (middle) and estimated aerosol surface area (bottom) from the nephelometer. Periods identified as exhaust have been removed and are not shown.

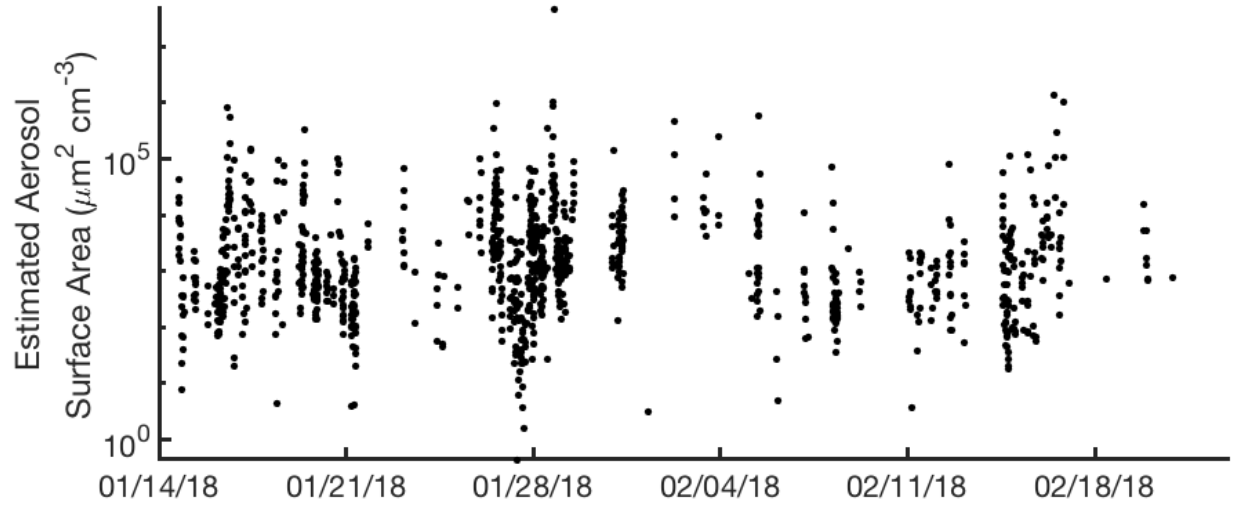

Figure 4.3: Timeseries of LIDAR-derived aerosol surface area at 300 m. Periods identified as being influenced by ship exhaust or clouds have been removed and are not shown.

A comparison of the LIDAR (Figure 4.3) and nephelometer-derived (Figure 4.2) shows the LIDAR estimates are generally 2-4 orders of magnitude higher than the nephelometer estimates, with a range of 4.4x10^{-1} - 4.7x10^{7} μm^{2} cm^{-3}, and a median of 1.1x10^{3} μm^{2} cm^{-3}. Based on the LIDAR attenuated backscatter profiles (Figure 4.4), it is likely that cloud-containing profiles remain in the dataset, and will require more careful filtering. Clear-sky profiles from Alexander and Protat (2019) during CAPRICORN-1 and CAPRICORN-2, using the same instrument, have a maximum $\log_{10}(\beta_{att})$ of -4.5, whereas Figure 4.4 indicates $\log_{10}(\beta_{att})$ values >-4 occur in supposedly cloud-free profiles in this dataset. The same study has a maximum of 300 Mm^{-1} for particle extinction coefficients in clear-sky profiles, in comparison to >10000 Mm^{-1} in this dataset (Figure 4.5).

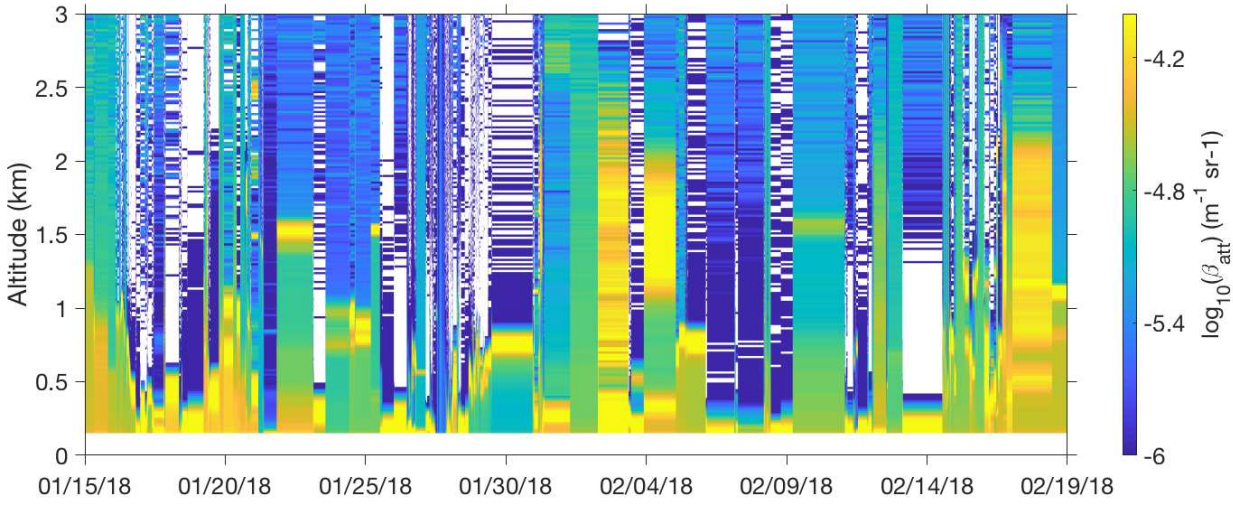

Figure 4.4: Timeseries of LIDAR attenuated backscatter profiles from CAPRICORN-2. Periods identified as being influenced by ship exhaust or clouds have been removed and are not shown.

Even excluding the very large LIDAR-estimated surface areas in Figure 4.3, the lower values are generally 1-2 orders of magnitude higher than the nephelometer estimates. This may be a result of the data used to derive the marine aerosol conversion parameter presented in Mamouri and Ansmann (2016). They used AERONET data from Ragged Point, Barbados, and limited their classification of marine aerosols to periods with Ångstrom exponents between 0.25 and 0.6, to eliminate periods that contained Saharan dust influences, which they determined

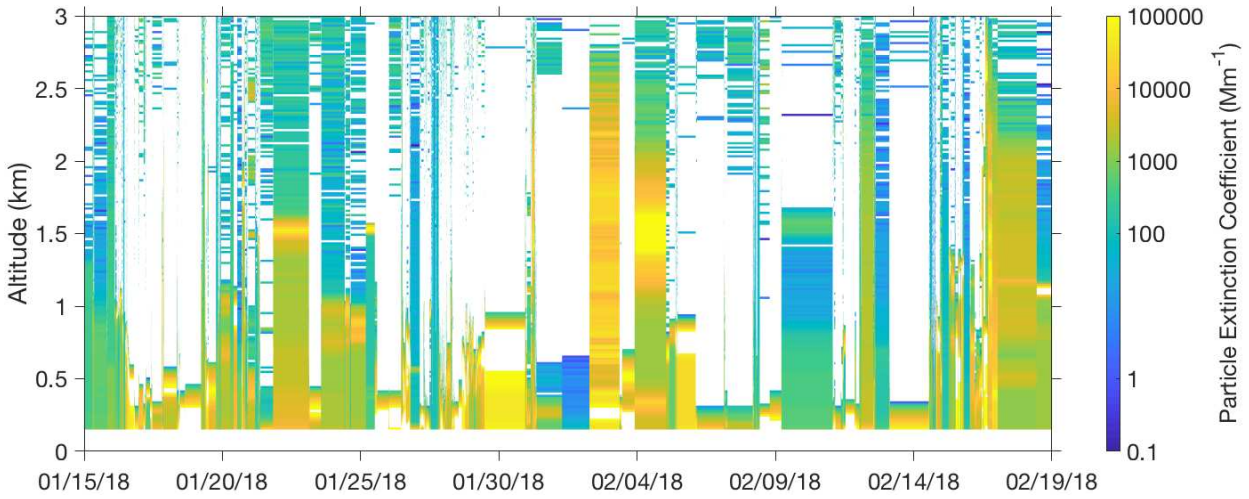

Figure 4.5: Timeseries of LIDAR particle extinction coefficient profiles from CAPRICORN-2. Periods identified as being influenced by ship exhaust or clouds have been removed and are not shown.

had Ångstrom exponents <0.2. However, Figure 4.2, along with other observations of marine aerosols (see Mulcahy et al. 2009), indicates SSA may exhibit Ångstrom exponents <0, particularly under high wind speed conditions, such as are common in the Southern Ocean. As a result, the marine aerosol conversion parameter derived in Mamouri and Ansmann (2016) may not be relevant for Southen Ocean primary SSA. These LIDAR results are preliminary, and additional filtering of profiles to remove cloudy periods, as well as determination of the optimal conversion factor between particle extinction and aerosol surface area, is required to improve agreement between LIDAR and other estimates of particle surface area.

4.4 COMPARISON OF AEROSOL SURFACE AREA MEASUREMENTS DURING CAPRICORN-2

A timeline of aerosol surface area measurements during CAPRICORN-2 from all methods is shown in Figure 4.6. As discussed in Section 4.3, the LIDAR estimates are 2-4 orders of magnitude larger than all the other observations, and don't appear to co-vary with the WIBS, nephelometer, or SMPS+APS. All the other measurements track well together, with the WIBS generally giving the lowest and the nephelometer the highest surface area concentrations. WIBS and nephelometer estimates have been plotted against the SMPS+APS-derived surface area values

in Figure 4.7, with the nephelometer measurements falling closest to the 1:1 line, though with a wide spread due to the large uncertainty in nephelometer-derived surface areas (DeMott et al. 2016). The WIBS and SMPS+APS have a very tight correlation, with a slope close to 0.3, indicating the WIBS is significantly underestimating aerosol surface area. This may be due to the observed undercounting of supermicron aerosol relative to the APS (Figure 4.1a), or to the contribution of accumulation mode aerosol to total surface area (Figure 4.1b), which are not detected by the WIBS. As seen in Figure 4.6, the LIDAR-derived surface area concentrations are much higher than the others, and exhibit no clear correlation with the SMPS+APS measurements.

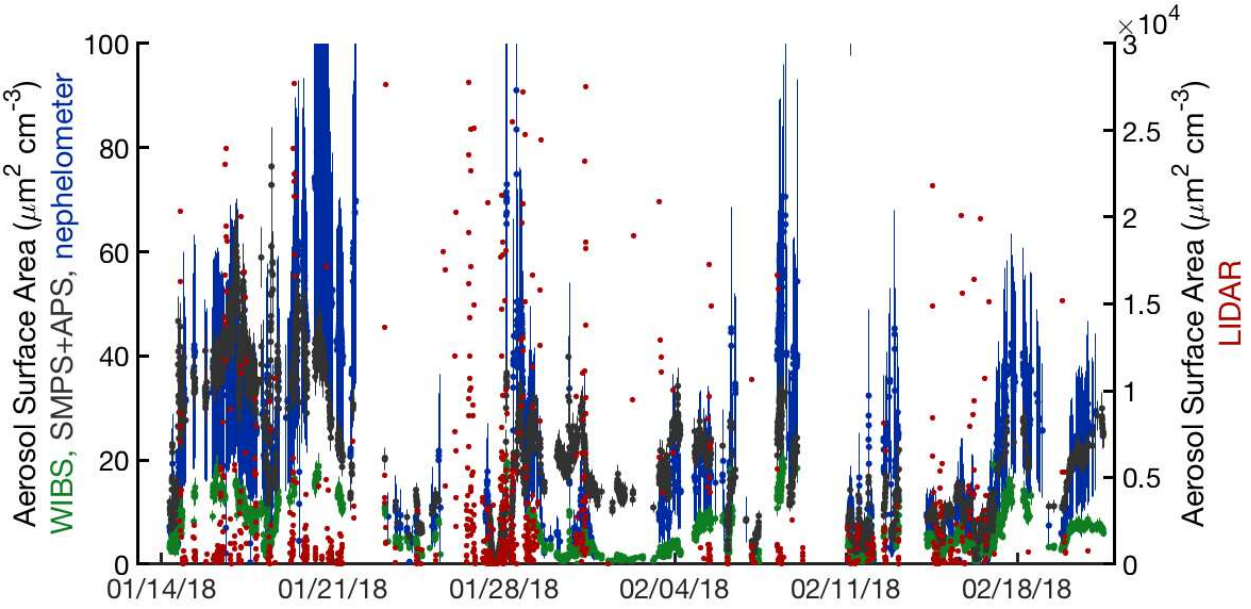

Figure 4.6: Timeseries of aerosol surface area derived from SMPS+APS, WIBS, nephelometer, and LIDAR measurements. Periods identified as being influenced by ship exhaust or clouds have been removed and are not shown.

Surface area concentrations from the SMPS+APS varied from 0.91-293.29 μm^2 cm^{-3}, with a mean of 21.28 μm^2 cm^{-3}. This is in good agreement with previous measurements (DeMott et al. 2016; McCluskey et al. 2018c) over the Southern Ocean and other ocean regions, as well as modeling results (McCluskey et al. 2019) from the Southern Ocean. The variability in surface area estimates from the WIBS, nephelometer, and SMPS+APS are shown in Figure 4.8 against

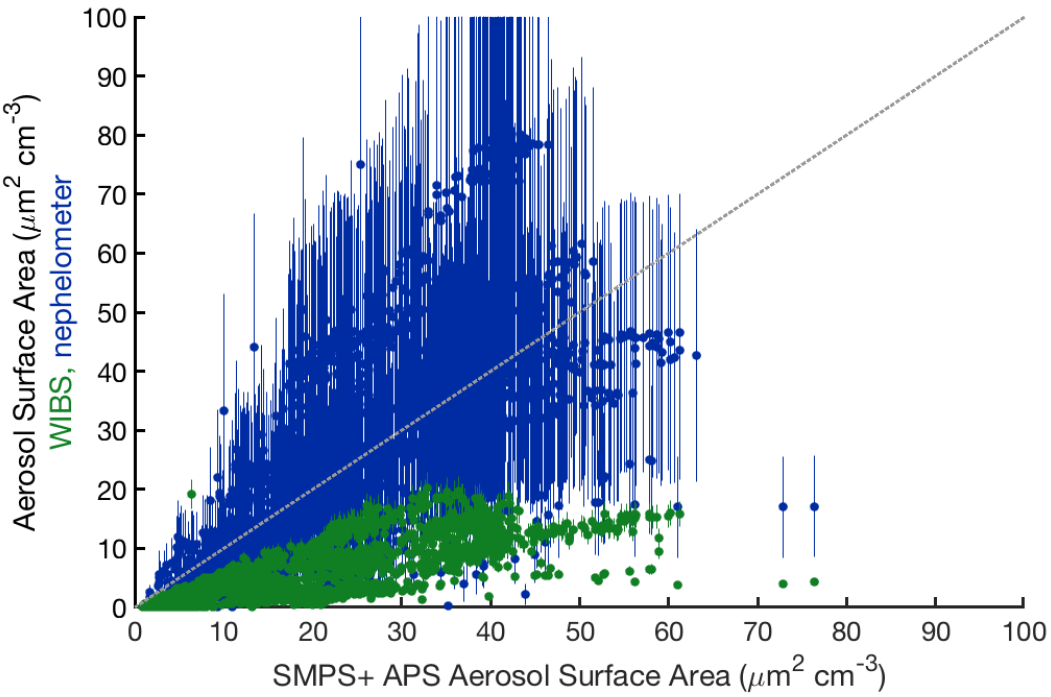

Figure 4.7: Comparison of WIBS and nephelometer- derived surface area with SMPS+APS measurements. The gray dashed line represents a 1:1 relationship.

latitude and wind speed. As expected if the surface area is dominated by primary SSA, aerosol surface area increases with wind speed just as coarse mode aerosol number does (Figure 3.3), although it plateaus above 15 m s^{-1}. Supermicron particle losses in the R/V *Investigator* aerosol inlet are significant above 3μm, and particle transmission efficiency is also influenced by ambient wind speed and direction. Preliminary calculations indicate modest enhancements in supermicron particle transmission of up to 5% when the ambient wind speed increases from 10 to 20 m s^{-1}, and reductions of 10-20% if the aerosol inlet is aligned more than 40° away from the prevailing wind direction. Such inlet losses may explain why aerosol surface area doesn't continue to increase with wind speed above 15 m s^{-1}. Alternatively, since accumulation mode aerosol is responsible for a significant fraction of aerosol surface area (Figure 4.1b), and has little or no correlation with wind speed (Figure 3.4), accumulation mode particle contribution to surface area may explain this flattening. LIDAR retrievals of aerosol surface area are not affected by inlet losses, and may be used to evaluate the relationship between particle number or surface area and wind speed in future studies. Enhancements in aerosol surface area are seen

around -47° to -49°, -50° to -53°, and -62° to -64°, which may be attributed to either wind-driven primary SSA (supermicron or accumulation mode) or increases in accumulation mode aerosol through either cloud processing or condensation of gases onto existing particles.

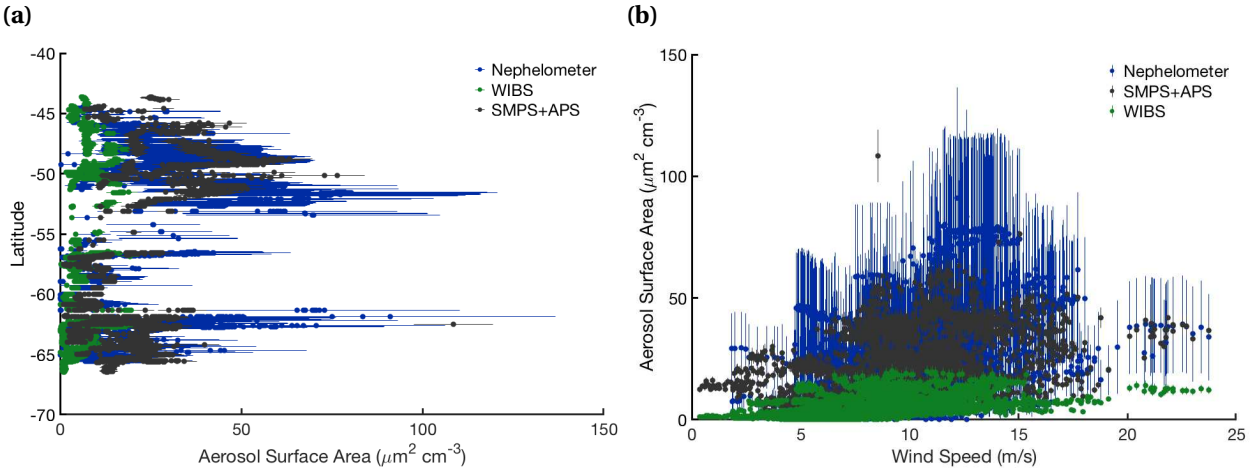

Figure 4.8: Variability in aerosol surface area measurements from the nephelometer (blue), WIBS (green), and SMPS+APS (gray) with latitude (a) and wind speed (b).

As indicated in Figure 4.7, particle surface area estimates derived from scattering measurements can be used in place of direct aerosol size distribution observations when those are unavailable. Single-particle scattering results from the WIBS had the tightest correlation with SMPS and APS-derived particle surface area, although undercounted by ~70%. Nephelometer measurements exhibited close to a 1:1 correlation with the SMPS and APS, but the large variability means up to a factor of 2 difference in surface areas derived using this method compared to an SMPS+APS. This correspondance between nephelometer and SMPS+APS derived surface areas validates the comparison made in Figure 3.8 between CAPRICORN-2 and CAPRICORN-1 n_s values, which used SMPS+APS and nephelometer derived surface areas, respectively. However, it does indicate larger uncertainties on n_s values derived from nephelometer measurements than size distributions. The LIDAR results presented here require further analysis before their general applicability can be assessed. This dataset may provide an opportunity to improve

existing conversion parameters (Mamouri and Ansmann 2016) using observations of remote marine aerosols.

5. Results: Ice Nucleating Particle Parameterization Methods

Particularly for global models, computational and memory constraints limit the number and complexity of processes that can be simulated. Ice nucleation is a complicated but important process affecting cloud phase, lifetime, and precipitation, and is often parameterized by normalizing INP concentrations with a more commonly measured value, such as particle surface area, number concentration, or composition as a function of activation temperature (Niemand et al. 2012; Ullrich et al. 2017; DeMott et al. 2010; 2015; McCluskey et al. 2018a; Hoose and Möhler 2012; Kanji et al. 2017; Wilson et al. 2015). Normalization with surface area gives the surface active site density (Section 2.5.5), n_s, and normalization with particle number gives activated fraction, n_N, which are the most commonly used parameterizations. Only two parameterizations have been published for marine INPs, one using n_s, and one relating INP concentration to particulate organic carbon. The marine n_s parameterization was developed using aerosol data collected at Mace Head Research Station in Western Ireland for periods identified as being influenced only by marine air masses (McCluskey et al. 2018a). Immersion freezing measurements of sea surface microlayer samples from the Arctic, North Atlantic, and North Pacific were used to develop the second parameterization, as a function of total organic carbon (Wilson et al. 2015). The TOC-based parameterization of Wilson et al. (2015) was evaluated in McCluskey et al. (2018a) for North Atlantic marine INPs and found to overpredict INP concentrations at -15 and -20 °C by a factor of 4 to 100, and will not be discussed further here.

INP measurements from CAPRICORN-2 were normalized using aerosol surface area and number concentration observations from the SMPS and APS (Section 4.1), which were averaged to the CFDC or filter sampling period. CAPRICORN-2 INP results are shown in Figure 5.1 for non-normalized INP concentrations (Figure 5.1a), n_s (Figure 5.1b), and n_N (Figure 5.1c), where coarse mode aerosol number concentrations (particles > 400 nm diameter) were used to calculate n_N and total particle surface area used to calculate n_s. The DeMott et al. (2010) parameterization (D10), which predicts INP concentrations based on number concentration of

aerosols larger than 500 nm, is shown in Figure 5.1a using the mean coarse mode aerosol number concentration measured during CAPRICORN-2 (4.3 cm^{-3}) for reference. D10 was developed primarily over continental regions, including free tropospheric measurements, under conditions relevant for mixed phase clouds, and was not intended to be applied to marine boundary layer aerosols. D10-predicted INP concentrations exceed measured SO concentrations at all temperatures by at least a factor of 10, with the largest discrepancies of four or more orders of magnitude at the warmest temperatures. It is shown here to illustrate that a different functional form, in addition to different constant values, may be needed to parameterize marine INPs, rather than using a global parameterization that includes all INP categories. This has been shown previously for mineral dust (DeMott et al. 2015) and biological INPs (Tobo et al. 2013).

The functional form of the n_s parameterizations used by Ullrich et al. (2017) and McCluskey et al. (2018a) agree much better with the CAPRICORN-2 data (Figure 5.1b), although both overestimate the observed n_s values. Reported INP concentrations from McCluskey et al. (2018a) are ~10 times higher than during CAPRICORN-2, while n_s values were ~5 times higher, implying twice as much aerosol surface area in the North Atlantic during McCluskey et al. (2018a) than in the Southern Ocean during CAPRICORN-2. Differences in inlet transmission efficiencies, assumed particle density and RH, and lower inlet height at Mace Head (Kleefeld et al. 2002) may all contribute to this. Mace Head Station is a coastal site, and despite precautions McCluskey et al. (2018a) results may also be influenced by local aerosol produced along the coastline. Unpublished results from the MARCUS and MICRE campaigns, concurrent with CAPRICORN-2, indicates higher INP concentrations from the island-based MICRE measurements than ship-based measurements (MARCUS) when the vessel was nearby, which may relate to coastal wave-breaking.

The gray shaded boxes in Figure 5.1 indicate two orders of magnitude on their respective y-axis scales for temperatures between -10 °C and -35 °C, which largely encapsulate the variability in INP concentrations, n_s, and n_N. This demonstrates that normalizing CAPRICORN-2 INP concentrations by aerosol surface area or coarse mode number concentration doesn't re-

(a)

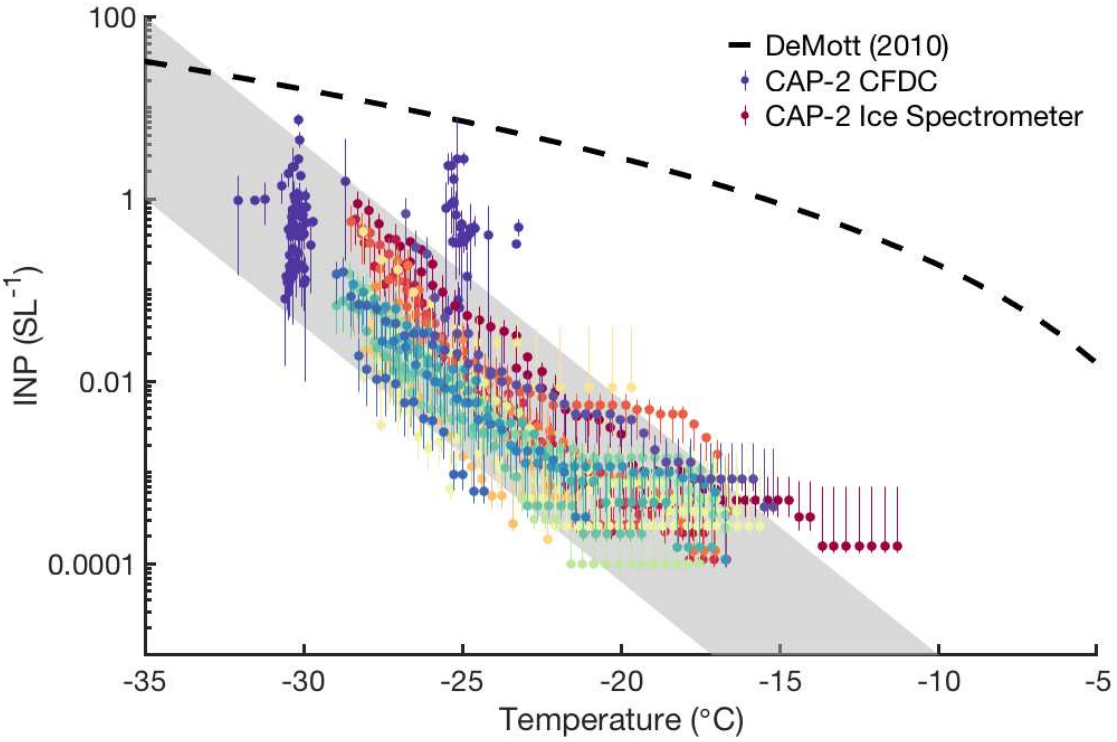
DeMott (2010)
CAP-2 CFDC
CAP-2 Ice Spectrometer
INP (SL^{-1})
100
1
0.01
0.0001
-35
-30
-25
-20
-15
-10
-5
Temperature (°C)

(b)

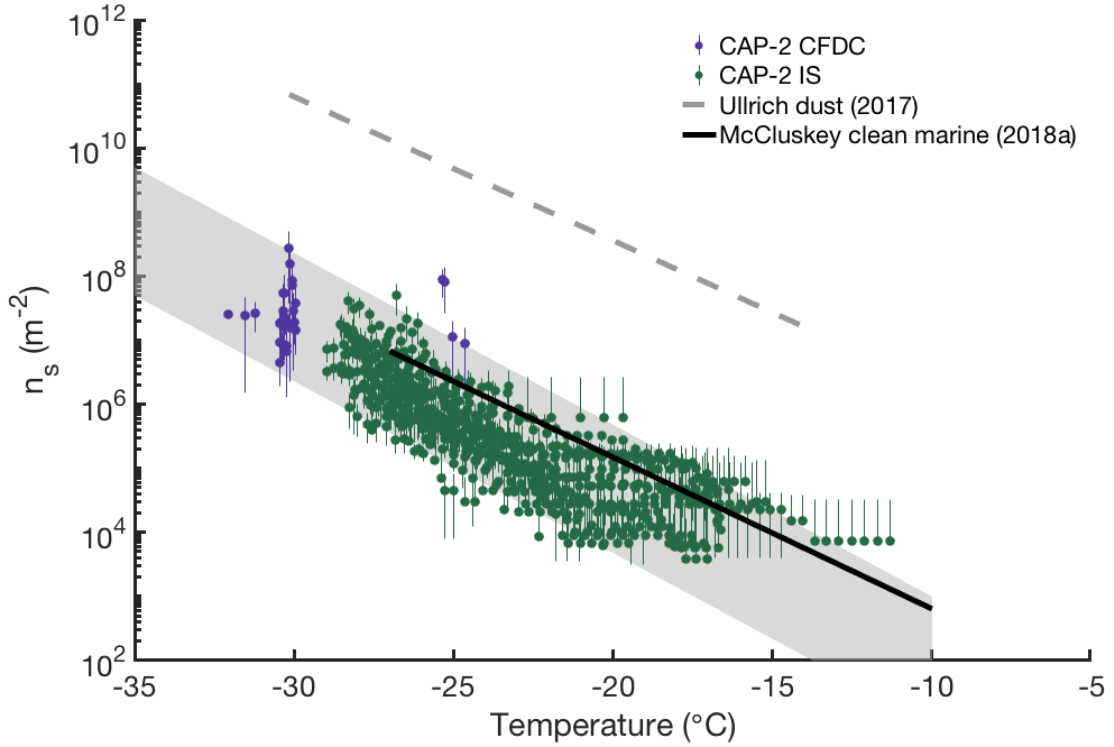
CAP-2 CFDC
CAP-2 IS
Ullrich dust (2017)
McCluskey clean marine (2018a)
n_s (m^{-2})
10^{12}
10^{10}
10^{8}
10^{6}
10^{4}
10^{2}
-35
-30
-25
-20
-15
-10
-5
Temperature (°C)

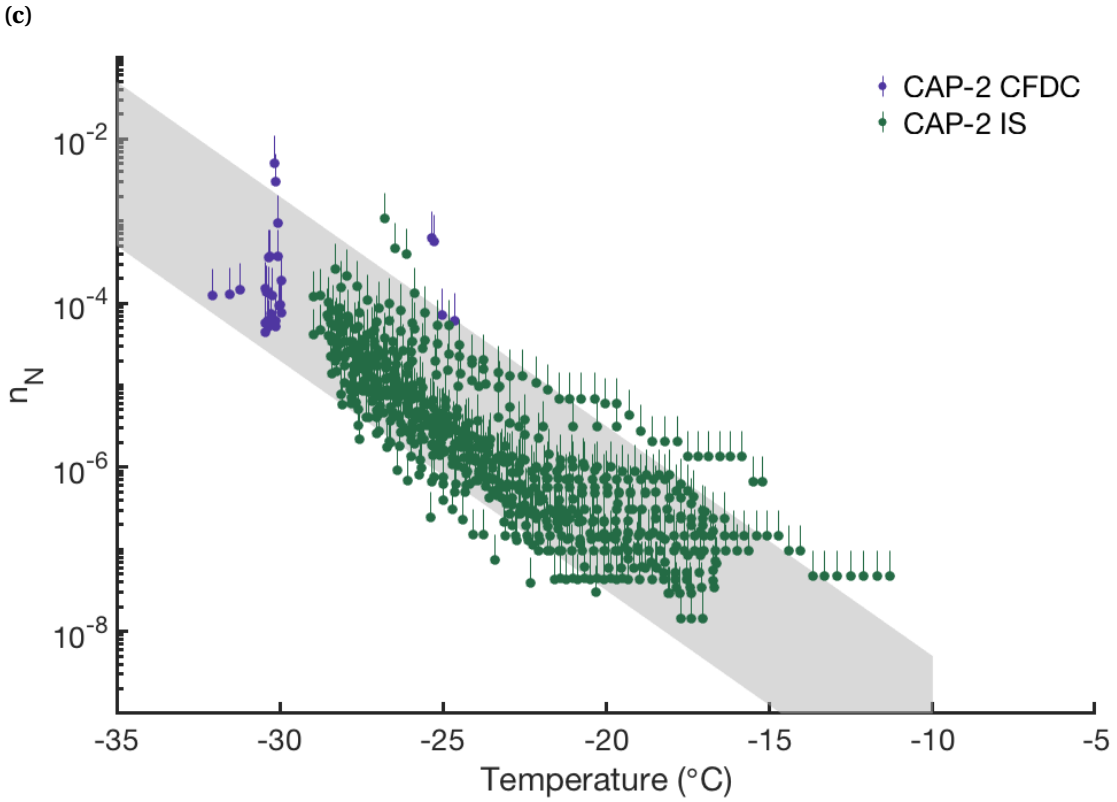

Figure 5.1: Comparison between CAPRICORN-2 INP concentration (a), n_s (b), and n_N (c) temperature spectra. Gray shaded regions denote 2 orders of magnitude on vertical axes. The black dashed line in (a) is the parameterization from DeMott et al. (2010) based on number concentration of aerosols larger than 500 nm. Aerosol surface area-based parameterizations for clean marine aerosols (McCluskey et al. 2018a) and mineral dust (Ullrich et al. 2017) are shown in (b) as solid black and gray dashed lines.

duce the observed variability in the data, as has been shown for other aerosol types (see DeMott et al. 2010). The relationships between INP concentration, aerosol surface area, and particle number concentration were explored using CFDC data at -30±1 °C. CFDC, rather than filter data, was chosen for this analysis because the higher time resolution of the CFDC allows variability in particle distributions to be seen more clearly. CFDC INP concentrations at -30 °C are shown in Figure 5.2 as a function of accumulation mode (70-400 nm), coarse mode (>400 nm), and total particle surface area and number concentration. Significant correlations (α=0.1) exist between INP concentration and accumulation mode number and surface area and total surface area, but the largest correlation coefficient is 0.56 (Table 5.1). The influence of wind speed on INP concentration and n_s is shown in Figure 5.3. Neither relationship is significant (α=0.1), and both correlation coefficients are <0.22 (Table 5.1). A simple regression model including wind speed and aerosol surface area and number concentration indicated only accumulation mode particle surface area was significant (p=0.05) in predicting INP concentrations at -30 °C. This may explain why normalizing INP concentrations to total particle surface area and coarse mode number concentration (Figure 5.1) did not clearly reduce the variability in observed INP concentrations.

Table 5.1: Correlation coeffients and p-values of relationships between INP concentrations (n_{INP}), particle surface area (SA) and number (N), and wind speed.

Relationship	Correlation Coefficient	p-value
n_s & wind speed	0.0135	0.9514
n_{INP} & wind speed	0.2134	0.1015
n_{INP} & accumulation N	0.5194	0.0111
n_{INP} & coarse N	-0.124	0.5729
n_{INP} & total N	-0.0461	0.8345
n_{INP} & accumulation SA	0.568	0.0047
n_{INP} & coarse SA	-0.1278	0.5613
n_{INP} & total SA	0.3706	0.0817

(a)

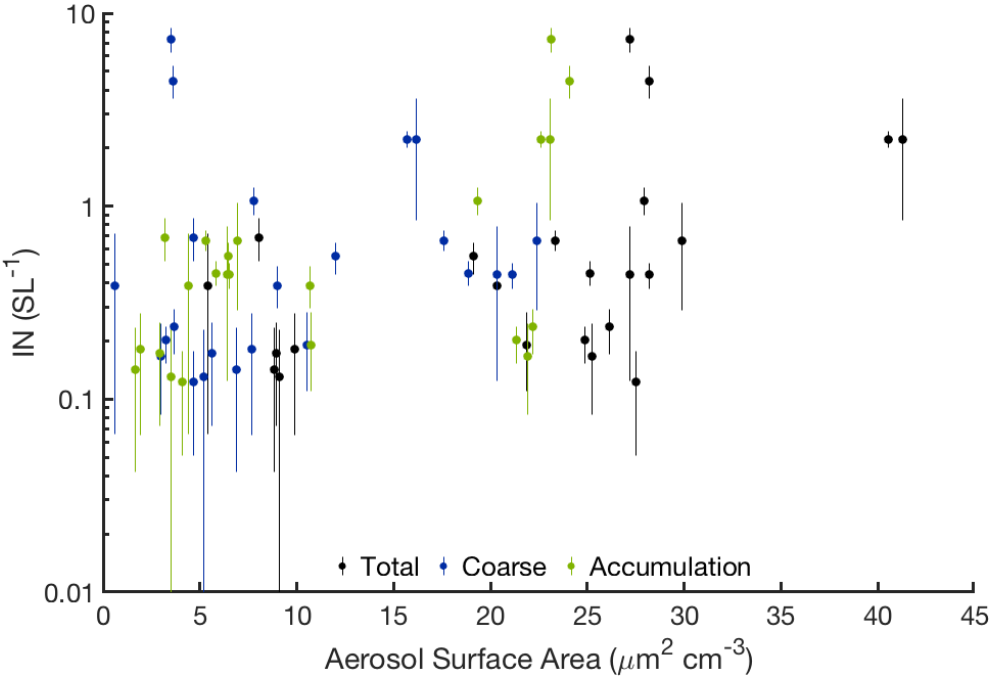

(b)

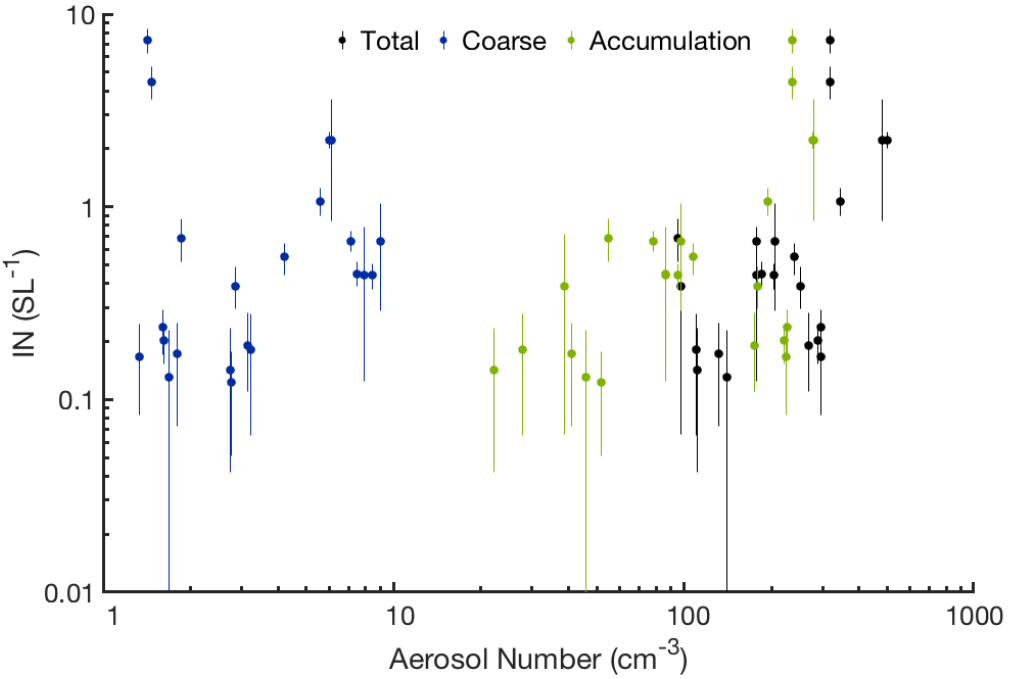

Figure 5.2: Relationship between INP concentrations at -30 °C and aerosol surface area (a) and number concentration (b) for the overall distribution, the accumulation mode, and the coarse mode.

(a)

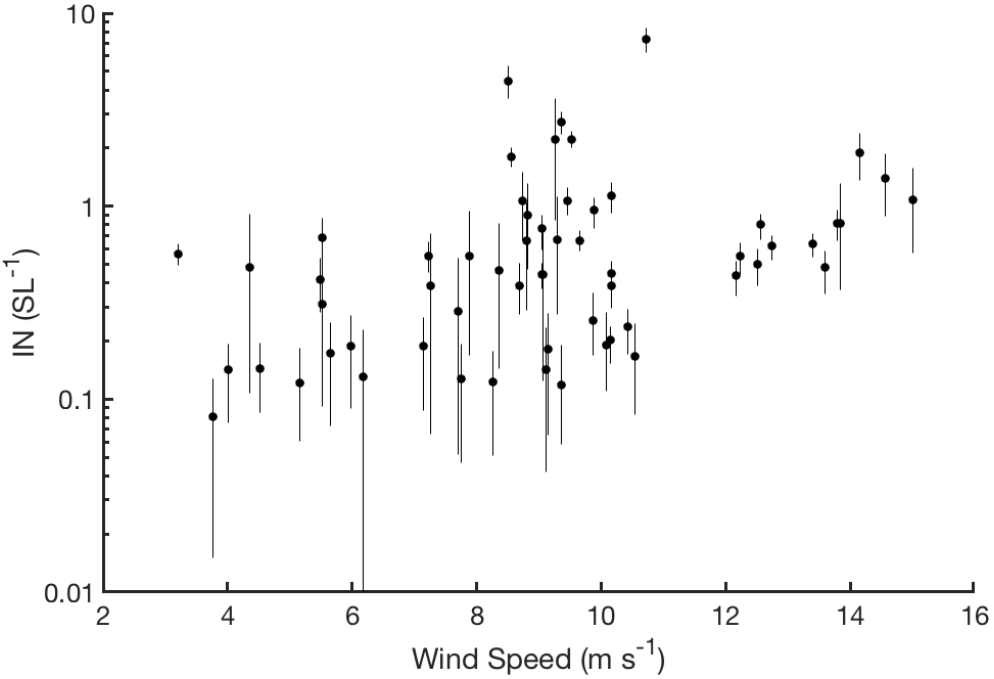

(b)

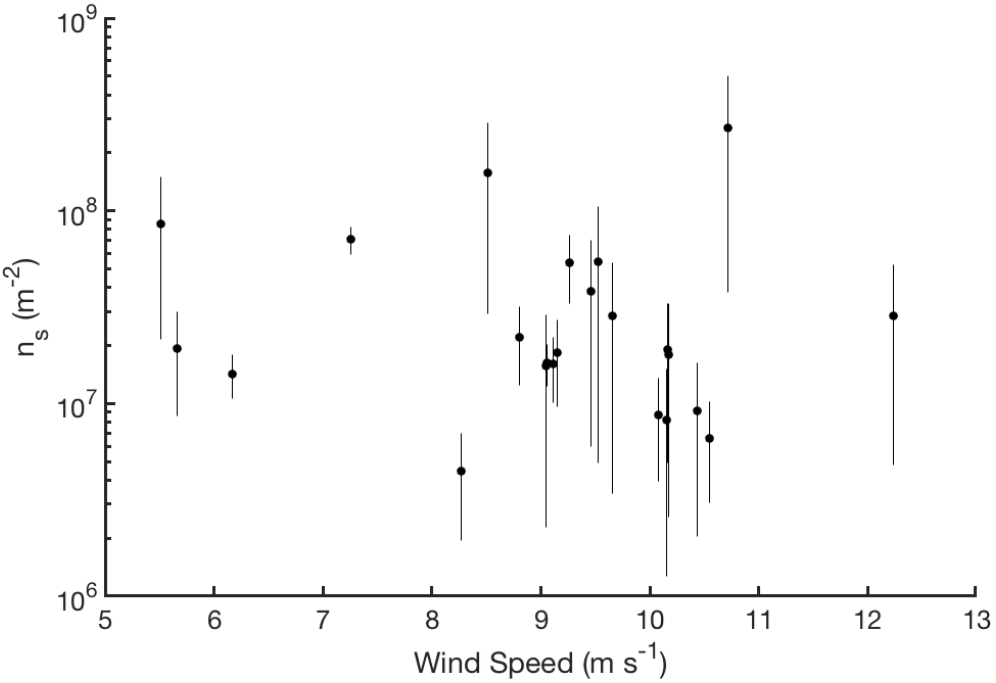

Figure 5.3: Variability of INP concentration (a) and n_s (b) at -30 °C with wind speed.

For marine INPs in particular, factors other than sea spray production may affect ambient concentrations. Mesocosm studies of SSA and *in situ* observations of seawater and sea surface microlayer have demonstrated correlations between INP concentrations and marine biological activity (DeMott et al. 2016; Irish et al. 2017; Wilson et al. 2015; McCluskey et al. 2018b; Schnell and Vali 1976). This appears to occur preferentially in the decay phase of a phytoplankton bloom (McCluskey et al. 2018b), coincident with enhanced organic aerosol production (O'Dowd et al. 2015; Wang et al. 2015). Specific diatom species and their exudates (Wilson et al. 2015), have been shown to be IN active, as well as marine macromolecules (McCluskey et al. 2018b), but otherwise little is known about the identity or release of INPs from the ocean. As proxies for biological activity, surface Chlorophyll *a* concentrations (Section 2.2.5) and fluorescent biological aerosol particles (FBAP) measured by the WIBS (Section 2.2.4.2) were compared to CFDC measurements at -30 °C. No significant correlations were found, as might be expected since no lag between biological activity and INP concentrations was accounted for (McCluskey et al. 2018b) in this simple analysis. Furthermore, biological marine INPs generally activate warmer than ~-22 °C (McCluskey et al. 2018b;c), and may not be emitted through the same mechanisms as those active at -30 °C. More detailed analysis will be conducted in future studies, including correlations of satellite-derived Chlorophyll *a* along backtrajectories released along the R/V *Investigator* voyage track.

One assumption made by both n_s and n_N parameterizations is that the particles responsible for ice nucleation do not come from the entire population but are confined to relatively larger sizes (e.g. diameters larger than 500 nm). Past studies of INPs in laboratory and continental areas (DeMott et al. 2010; Richardson et al. 2007; Stith et al. 2009; Phillips et al. 2008), have indicated strong linear or power law relationships between INP concentrations and aerosol surface area or number, especially when constrained to particles >0.5 μm. The predominance of mineral dust (DeMott et al. 2010; Hoose and Möhler 2012; Ullrich et al. 2017; Kanji et al. 2017) and biological particles (Hoose and Möhler 2012; Möhler et al. 2007; Kanji et al. 2017) as INPs supports this relationship with large aerosols. Few studies have explored the relationship be-

tween marine ice nucleating particles and aerosol characteristics, particularly for regions where terrestrial inputs of dust and biological aerosol are limited, such as the Southern Ocean. McCluskey et al. (2018b) identified two main types of marine INPs from mesocosm studies: (1) particulate organic carbon that is larger than 0.2 μm, and (2) refractory dissolved organic carbon that is smaller than 0.2 μm. Other studies in the equatorial Pacific (Rosinski et al. 1987) and North Atlantic (Wilson et al. 2015; Irish et al. 2017) concluded that particles acting as marine INPs were smaller than 0.3 μm and 0.2 μm, respectively.

INP measurements made using the aerosol concentrator (Section 2.2.2) were used to infer an upper bound on the size of marine INPs over the Southern Ocean (Figure 5.4). As seen in Figure 5.4a, there is no relationship between the concentration factor for INPs and for aerosols larger than 500 nm, and the mean INP concentration factor during CAPRICORN-2 was 4.84; much lower than expected based on past observations and the expected aerosol size distributions. The gray shaded regions on both figures show the range of average INP concentration factors that have been measured for past field campaigns in continental regions, using the same aerosol concentrator and similar CFDC instruments. Based on the aerosol concentrator calibration in Figure 5.4b, this implies that continental INP-active aerosols are ~1 μm, and could at times extend to much larger sizes, as the maximum particle size that can enter the CFDC is 1.5 or 2.4 μm due to the upstream impactors. The mean value for CAPRICORN-2, 4.84, indicates the Southern Ocean INP-active aerosols are predominately <0.5 μm, and possibly much smaller, though this comparison only provides an upper bound. It's possible, as seen in (McCluskey et al. 2018b), for there to be multiple populations of marine INPs, each with a different source. The good overlap and alignment between CFDC measurements, which only include particles <2.4 μm, and filter measurements, which include particles >10 μm, suggests the CFDC measurements are capturing most aerosol sizes relevant for ice nucleation (Figure 5.1a) in this region, and there are not significant contributions of INPs from a larger size mode. This agrees well with Figure 5.2a and the correlation analysis presented above, indicating SO INPs are associated with accumulation mode particles in the range of 70-400 nm.

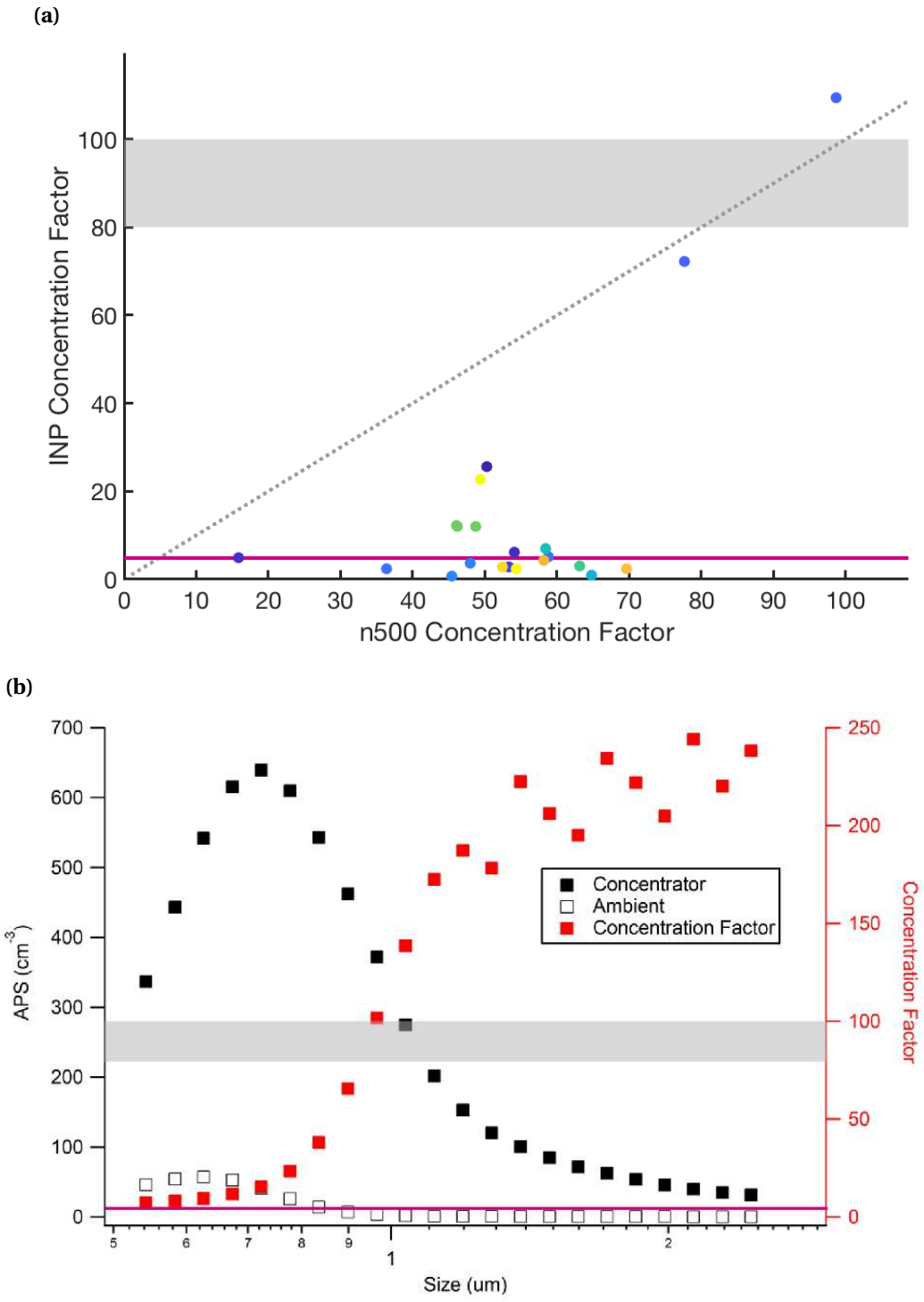

Figure 5.4: Relationship between INP concentration factor and concentration factor of particles larger than 500 nm (a) and aerosol concentration factor as a function of particle size (b). (b) replicates Figure 2.3. Gray shaded regions indicate the range of INP concentration factors measured in previous campaigns, and the purple solid lines indicate the median value for CAPRICORN-2. The gray dashed line in (a) is a 1:1 line shown for reference only. Data shown in (b) were collected in May 2016, in association with reported results in DeMott et al. (2017).

6. Conclusions

The Southern Ocean represents one of the few pristine aerosol environments left where preindustrial aerosol forcings may be estimated (Hamilton et al. 2014). Its remoteness from continental, as well as anthropogenic, sources, means it is likely dominated by marine aerosol, and may be a good test case for evaluating marine aerosol-cloud interactions in models, which are still not well understood (Carslaw et al. 2010; Quinn and Bates 2011). Due to the difficulty of reaching and working in an often cold and stormy environment, *in situ* observations of clouds and aerosols, particularly those relevant for cloud ice formation, are rare over the Southern Ocean. Satellite retrievals indicate a greater occurrence of mixed phase clouds containing supercooled liquid water in the SO than at high latitudes in the Northern Hemisphere (Morrison et al. 2011; Chubb et al. 2013), and that clouds are rarely glaciated at cloud top, even down to -25 °C (Morrison et al. 2011; Huang et al. 2012). Widespread occurrance of SLW in clouds, observed low INP number concentrations in this region (McCluskey et al. 2018c; Schmale et al. 2019), and recent modeling work (Burrows et al. 2013; Vergara-Temprado et al. 2018) suggest primary ice nucleation may play a large role in controlling cloud phase and precipitation over the Southern Ocean. Observations of SO aerosols, boundary layer processes, and clouds were made during four concurrent field campaigns in 2017-2018. Results presented here focused on the ship-board INP measurements collected during CAPRICORN-2, but observations from the other campaigns will be integrated in the future to provide information about spatial, seasonal, and vertical variability of INPs over the SO.

Marine boundary layer observations of particles and INPs were presented in Section 3. A trimodal aerosol size distribution was common, and was comprised of Aitken (20-70 nm), accumulation (70-400 nm) and coarse (>400 nm) modes (Figure 3.2). A ubiquitous hoppel minimum around 70 nm indicates widespread cloud processing in this region, consistent with recent measurements of Alroe et al. (2019) and Schmale et al. (2019). Number concentrations averaged 314 cm^{-3}, and were dominated by the Aitken and accumulation modes. Particle surface area was

dominated by the coarse mode, with a significant contribution from the accumulation mode at times. INP concentrations from CAPRICORN-2 (Figure 3.7) are consistent with other modern measurements in the region (McCluskey et al. 2018c; Schmale et al. 2019), but significantly lower than observations from the 1960s (Bigg 1973), which may be related to changes in dust inputs to this region (personal communication with P. Ginoux, NOAA GFDL, 2019). SO INP numbers fall at the lower bound of those reported for other ocean basins (DeMott et al. 2016), which may indicate less influence of mineral dust in this sector of the SO than in regions such as the Canadian Arctic (Irish et al. 2019). Through CAPRICORN-2 and the other concurrent field projects presented in this thesis, the range of INP observations in the SO has been expanded greatly from -53° to -66°.

A comparison of methods to estimate particle surface area was given in Section 4 using size distributions (SMPS+APS, WIBS), bulk particle scattering (nephelometer), and particle backscatter coefficients (LIDAR). Particle number and surface area distributions given by the WIBS instrument, which measures fluorescent biological aerosol particles, have not previously been evaluated against direct measurements using an SMPS+APS. A strong correlation was seen for particle surface area between the WIBS and SMPS+APS, although the WIBS undercounted by ~70% (Figure 4.7). Observed undercounting of particles ≥3 μm may account for some of this (Figure 4.1), in addition to the more limited size range of the WIBS (> 0.8 μm) compared to the SMPS. The amount to which the WIBS underestimates particle surface area will vary based on differences in aerosol particle distributions at different locations. Nephelometer-derived particle surface areas exhibited close to a 1:1 correlation with SMPS+APS measurements (Figure 4.7), but the large uncertainty may lead to up to a factor of 2 difference between the estimates. This provides some confidence in the past use of nephelometer data to parameterize INP concentrations (DeMott et al. 2016; McCluskey et al. 2018a), and updates the uncertainty bounds presented in those studies for n_s. LIDAR backscatter profiles have been previously shown to reproduce aerosol number and surface areas (Mamouri and Ansmann 2016), and the technique presented in Mamouri and Ansmann (2016) was applied for the first time to SO aerosols. Addi-

tional filtering to remove cloudy profiles not identified by the detection scheme from Alexander and Protat (2018) is still required, but even the lowest LIDAR estimates of aerosol surface area are 10-100 times larger than those derived from all other methods. The conversion parameter defined in Mamouri and Ansmann (2016) is suspected to be the cause of the remaining discrepancy, and will be investigated further. Overall, good agreement was seen between WIBS, nephelometer, and SMPS+APS surface areas, which can greatly increase the amount of such observations, when direct size distribution measurements are unavailable. This greatly enhances our ability to evaluate model parameterizations of ice nucleation at more times and locations globally, as aerosol surface area and number concentration are common normalization metrics (DeMott et al. 2010; 2015; Niemand et al. 2012; Ullrich et al. 2017; McCluskey et al. 2018a).

Parameterizations of atmospheric ice nucleation in models was the focus of Section 5, in particular those involving particle surface area (n_s) and number (n_N). Ice nucleation active site density calculated from CAPRICORN-2 was compared to both CAPRICORN-1 results from a similar region (McCluskey et al. 2018c) and the marine aerosol parameterization presented in McCluskey et al. (2018a) for the North Atlantic (Figure 3.8). The McCluskey et al. (2018a) parameterization was found to overpredict mean n_s from CAPRICORN-2 by about a factor of 5. Perhaps as a result of the much larger latitude range sampled during CAPRICORN-2 than CAPRICORN-1, n_s values from the more recent voyage agree well with previous measurements but extend to lower values at all temperatures for which comparisons were possible (down to -26 °C). Significant correlations (α=0.1) were observed between CFDC measurements of INPs at -30 °C and accumulation mode number and surface area and total surface area, although the largest correlation coefficient was 0.56 (Table 5.1). No significant relationship was found between either INP concentrations or n_s at -30 °C and wind speed. These results, along with inferences about INP size made using the aerosol concentrator (Figure 5.4), support previous observations from other ocean regions that marine INPs are dominated by small particles, <500 nm (McCluskey et al. 2018b; Rosinski et al. 1987; Wilson et al. 2015; Irish et al. 2017). This is in contrast to continental INPs, where strong relationships between INP concentration and large

particles (e.g. diameters larger than 500 nm) have been observed (DeMott et al. 2010; Richardson et al. 2007; Stith et al. 2009; Phillips et al. 2008). The small sizes of marine INPs inferred here is consistent with observed low n_s values calculated from total particle surface area, since the number of surface active sites scales with surface area, which is dominated by supermicron particles. The multiple sources and sinks of accumulation mode aerosol, including primary emission, condensational growth, oxidation, coagulation, and cloud processes complicate the relationship between INP number concentration and accumulation mode particles. As a result, a different functional form or different independent variable may be needed to accurately parameterize marine INPs in models. Connections between ocean biogeochemistry and aerosol-cloud interactions are complex and will require further observational and modeling studies.

7. Future Work

In addition to the SOCRATES and CAPRICORN-2 campaigns, there were two other field studies our group participated in, also focused on ocean-aerosol-cloud interactions in the Southern Ocean during 2017-2018, with complementary and duplicate measurements. Aerosol filters collected during MICRE (Macquarie Island Cloud and Radiation Experiment) at the Australian Antarctic Division's (AAD) Macquarie Island Station (54.62 °S, 158.86 °E) from March 2017-March 2018 will provide the first annual cycle of INP measurements at a fixed site in the Southern Ocean region, yielding information about seasonal and intra-seasonal variability in the concentration and composition of SO INPs. The DOE-ARM Measurements of Aerosols, Radiation and CloUds over the Southern Oceans (MARCUS) campaign on the R/V *Aurora Australis* from November 2017-March 2018 also included aerosol filter collections for IS measurements, in addition to a DOE-ARM Aerosol Observation Suite for aerosol and remote sensing observations and a WIBS instrument (Martin Schnaiter, Karlsruhe Institute of Technology). A main focus in the upcoming months will be to integrate observations from MARCUS, MICRE, SOCRATES, and CAPRICORN-2, to provide a holistic view of Southern Ocean INPs and their spatial and temporal variation. A selection of planned future analyses are presented below, which fall into the following categories:

1. Improved understanding of marine INP composition, using inferences from heat and peroxide treatments of IS filters and seawater samples (Section 2.2.3.1), as well as TEM and STXM-NEXAFS analysis of ice crystal residuals collected using the CFDC (Section 2.2.1.1).

2. TEM size measurements of collected INPs (Section 2.2.1.1) to support the inference that SO INPs are <0.5 μm (Section 5). Additionally, size fractionation of particles collected onto filters, as well as seawater samples, followed by immersion freezing measurements, to probe the sizes of the ice nucleation active entities in SSA.

3. Further analysis of the factors that explain variability in INP concentrations, including comparison to FBAP concentrations measured using the WIBS (Section 2.2.4.2) and DNA results from CAPRICORN-2 (Uetake et al. 2020).

4. Comparison of the G-V and R/V *Investigator* measurements during CAPRICORN-2 to understand the vertical structure of INP concentration and composition below, in, and above clouds in the Southern Ocean.

5. Collaboration with observational and modeling groups investigating secondary ice production during SOCRATES to determine the relative importance of primary versus secondary ice production in controlling cloud phase.

6. Improvement of LIDAR-derived aerosol surface area estimates for the Southern Ocean (Section 4.3) and comparison of the additional parameterizations for INP concentration profiles presented in Mamouri and Ansmann (2016) with observations.

Preliminary results addressing 1 and 4 from G-V measurements during SOCRATES are shown here, which will be built on in future publications. A comparison of INP concentration temperature spectra from the G-V (SOCRATES) and R/V *Investigator* (CAPRICORN-2) for measurements made in the marine boundary layer are presented in Figure 7.1. It should be noted that this figure represents all measurements made from the G-V in the MBL and all R/V *Investigator* observations, which cover different spatial ranges, and were not collected simultaneously except in a few cases. G-V MBL measurements shown here may not always be from within the directly coupled section, although most are from ~ 500 asl. INP number concentrations <-28 °C are similar at the surface and aloft, but higher concentrations were observed from the G-V at warmer temperatures. Average INP concentrations measured on the G-V are higher than those measured on the R/V *Investigator* by a factor of ~5. Interestingly, the G-V IS measurements at -25 °C agree well with the CAPRICORN-2 CFDC measurements at that temperature, which may reflect the much shorter filter collection times on the aircraft than the ship, allowing more temporal variability to be captured.

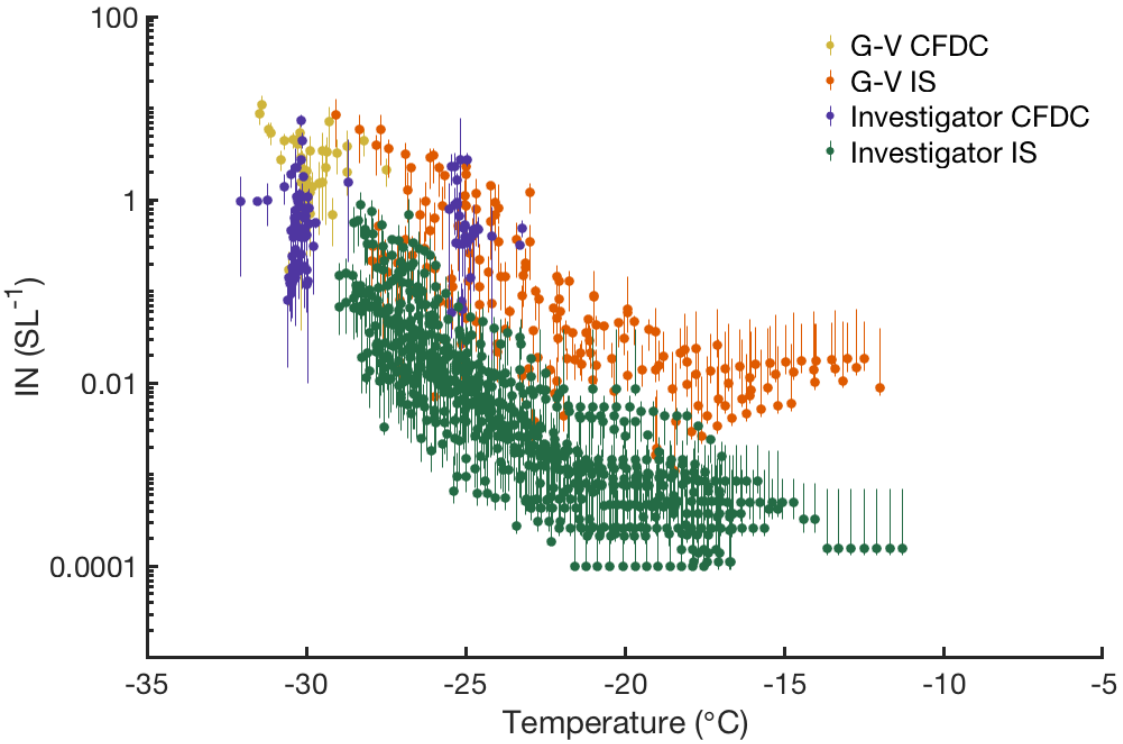

Figure 7.1: Comparison of INP temperature spectra measured during CAPRICORN-2 and SOCRATES. All measurements presented here were made in the marine boundary layer.

Figure 7.2 shows the entirety of INP measurements made from the G-V during SOCRATES in the MBL and above cloud top. INP number concentrations above and below cloud are similar, although normalizing the INP concentrations using the number concentration of particles larger than 500 nm to give n_N (Figure 7.3), indicates there may be different INP populations in the MBL and in cloud, versus above cloud. The similarity between the CFDC n_N for below-cloud and in-cloud measurements of cloud residuals may imply the INPs influencing low clouds over the Southern Ocean are primarily from the MBL and not the free troposphere, although analysis of more flights is needed. Figure 7.3 also suggests that while for marine boundary layer INPs (Figure 5.1) normalization by aerosol surface area or number concentration doesn't clearly separate measurements, these techniques may be useful in identifying different sources or types of INPs influencing clouds.

The hypothesis that INPs affecting Southern Ocean clouds are primarily from SSA is supported by TEM analysis of aerosol grids collected using the G-V CVI inlet during SOCRATES for

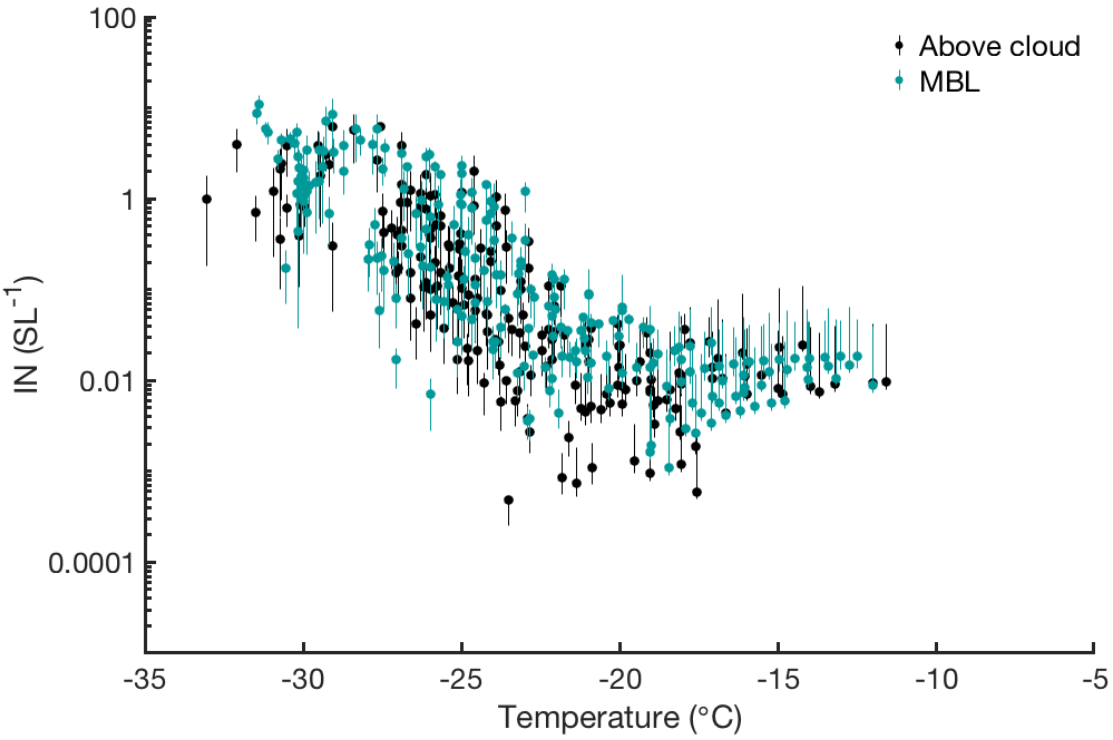

Figure 7.2: Comparison of INP temperature spectra measured during SOCRATES in the MBL and above cloud.

below, in, and above cloud passes (Figure 7.4). For both the small (Figure 7.4a) and large (Figure 7.4b) particles, sea spray is abundant below and in cloud, but only contributes to a small fraction of particles above cloud. Tracers for dust (crustal, metals) and biomass burning (combustion), were only seen in significant numbers above cloud and in larger particles. Dust only representing a significant fraction of particles above cloud, and the inferred small size of marine INPs (Section 5) may mean dust is a small fraction of the INPs influencing Southern Ocean boundary layer clouds. However, since mineral dust is a very efficient ice nucleator compared to sea spray (Niemand et al. 2012; Ullrich et al. 2017; DeMott et al. 2015; Figure 3.8), even very small amounts can affect cloud glaciation. Modeling studies explicitly targeting the relative contributions of dust and marine INPs to SO clouds are needed to corroborate this observation, as well as the low n_s values and small INP sizes inferred in Section 5.

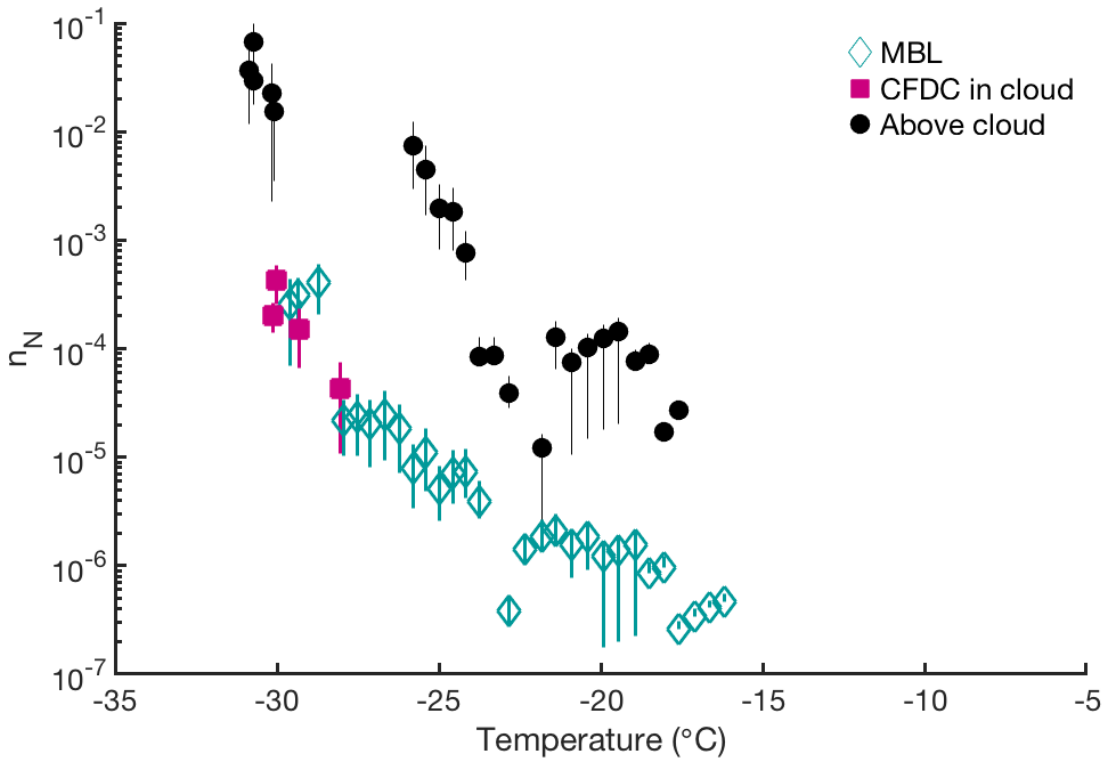

Figure 7.3: SOCRATES RF08 n_N temperature spectra measured in the MBL, in cloud (CFDC only, from the CVI inlet) and above cloud.

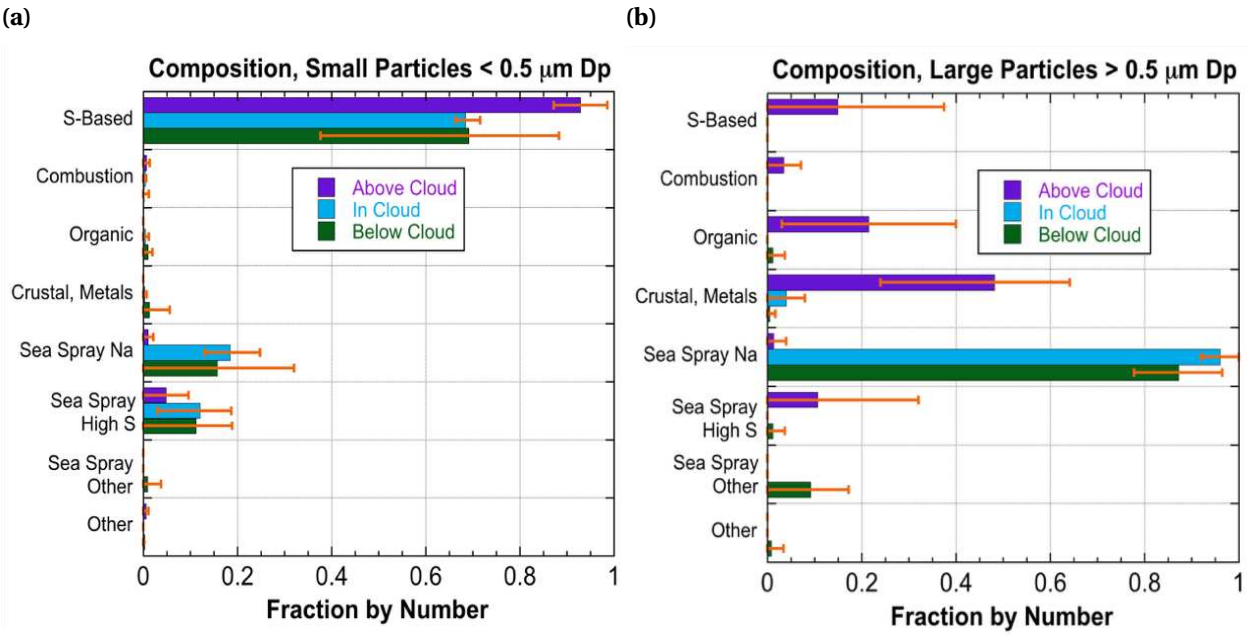

Figure 7.4: Preliminary TEM results from aerosol grids collected from the G-V CVI inlet during SOCRATES for particles smaller than (a) and larger than (b) 0.5 μm.

Bibliography

Agresti, A. and B. A. Coull, 1998: Approximate Is Better than "Exact" for Interval Estimation of Binomial Proportions. *The American Statistician*, **52 (2)**, 119, doi:10.2307/2685469.

Alexander, S. P. and A. Protat, 2018: Cloud Properties Observed From the Surface and by Satellite at the Northern Edge of the Southern Ocean: SOUTHERN OCEAN CLOUDS. *Journal of Geophysical Research: Atmospheres*, **123 (1)**, 443–456, doi:10.1002/2017JD026552.

Alexander, S. P. and A. Protat, 2019: Vertical Profiling of Aerosols With a Combined Raman-Elastic Backscatter Lidar in the Remote Southern Ocean Marine Boundary Layer (43–66°S, 132–150°E). *Journal of Geophysical Research: Atmospheres*, **124 (22)**, 12 107–12 125, doi:10.1029/2019JD030628.

Alroe, J., et al., 2019: Marine productivity and synoptic meteorology drive summertime variability in Southern Ocean aerosols. Preprint, Aerosols/Field Measurements/Troposphere/Physics (physical properties and processes). doi:10.5194/acp-2019-1081.

Andreae, M. O., 2007: Aerosols Before Pollution. *Science*, **315 (5808)**, 50–51, doi:10.1126/science.1136529.

Astle, M. J., 1980: *CRC Handbook of Chemistry and Physics: A Ready-Reference Book of Chemical and Physical Data*. 61st ed., CRC Press, Boca Raton, FL, USA.

Berezinski, N. A., G. V. Stepanov, and V. G. Khorguani, 1988: Ice-forming activity of atmospheric aerosol particles of different sizes. *Atmospheric Aerosols and Nucleation*, P. E. Wagner and G. Vali, Eds., Springer, Berlin, Heidelberg, 709–712, Lecture Notes in Physics, doi:10.1007/3-540-50108-8_1167.

Bigg, E., 1990: Long-term trends in ice nucleus concentrations. *Atmospheric Research*, **25 (5)**, 409–415, doi:10.1016/0169-8095(90)90025-8.

Bigg, E. K., 1973: Ice Nucleus Concentrations in Remote Areas. *Journal of the Atmospheric Sciences*, **30 (6)**, 1153–1157, doi:10.1175/1520-0469(1973)030<1153:INCIRA>2.0.CO;2.

Bodas-Salcedo, A., et al., 2013: Origins of the Solar Radiation Biases over the Southern Ocean in CFMIP2 Models. *Journal of Climate*, **27 (1)**, 41–56, doi:10.1175/JCLI-D-13-00169.1.

Brockmann, J. E., 2011: Aerosol Transport in Sampling Lines and Inlets. *Aerosol Measurement*, John Wiley & Sons, Ltd, 68–105, doi:10.1002/9781118001684.ch6.

Bromwich, D. H., et al., 2012: Tropospheric clouds in Antarctica. *Reviews of Geophysics*, **50 (1)**, doi:10.1029/2011RG000363.

Burrows, S. M., C. Hoose, U. Pöschl, and M. G. Lawrence, 2013: Ice nuclei in marine air: Biogenic particles or dust? *Atmospheric Chemistry and Physics*, **13 (1)**, 245–267, doi:10.5194/acp-13-245-2013.

Carslaw, K. S., O. Boucher, D. V. Spracklen, G. W. Mann, J. G. L. Rae, S. Woodward, and M. Kulmala, 2010: A review of natural aerosol interactions and feedbacks within the Earth system. *Atmospheric Chemistry and Physics*, **10 (4)**, 1701–1737, doi: https://doi.org/10.5194/acp-10-1701-2010.

Carslaw, K. S., et al., 2013: Large contribution of natural aerosols to uncertainty in indirect forcing. *Nature*, **503 (7474)**, 67–71, doi:10.1038/nature12674.

Ceppi, P., Y.-T. Hwang, D. M. W. Frierson, and D. L. Hartmann, 2012: Southern Hemisphere jet latitude biases in CMIP5 models linked to shortwave cloud forcing. *Geophysical Research Letters*, **39 (19)**, doi:10.1029/2012GL053115.

Ceppi, P., M. D. Zelinka, and D. L. Hartmann, 2014: The response of the Southern Hemispheric eddy-driven jet to future changes in shortwave radiation in CMIP5. *Geophysical Research Letters*, **41 (9)**, 3244–3250, doi:10.1002/2014GL060043.

Chubb, T. H., J. B. Jensen, S. T. Siems, and M. J. Manton, 2013: In situ observations of supercooled liquid clouds over the Southern Ocean during the HIAPER Pole-to-Pole Observation campaigns. *Geophysical Research Letters*, **40 (19)**, 5280–5285, doi:10.1002/grl.50986.

DeCarlo, P. F., J. G. Slowik, D. R. Worsnop, P. Davidovits, and J. L. Jimenez, 2004: Particle Morphology and Density Characterization by Combined Mobility and Aerodynamic Diameter Measurements. Part 1: Theory. *Aerosol Science and Technology*, **38 (12)**, 1185–1205, doi:10.1080/027868290903907.

DeMott, P. J., D. J. Cziczo, A. J. Prenni, D. M. Murphy, S. M. Kreidenweis, D. S. Thomson, R. Borys, and D. C. Rogers, 2003: Measurements of the concentration and composition of nuclei for cirrus formation. *Proceedings of the National Academy of Sciences*, **100 (25)**, 14 655–14 660, doi:10.1073/pnas.2532677100.

DeMott, P. J., et al., 2010: Predicting global atmospheric ice nuclei distributions and their impacts on climate. *Proceedings of the National Academy of Sciences*, **107 (25)**, 11 217–11 222, doi:10.1073/pnas.0910818107.

DeMott, P. J., et al., 2015: Integrating laboratory and field data to quantify the immersion freezing ice nucleation activity of mineral dust particles. *Atmospheric Chemistry and Physics*, **15 (1)**, 393–409, doi:10.5194/acp-15-393-2015.

DeMott, P. J., et al., 2016: Sea spray aerosol as a unique source of ice nucleating particles. *Proceedings of the National Academy of Sciences*, **113 (21)**, 5797–5803, doi:10.1073/pnas.1514034112.

DeMott, P. J., et al., 2017: Comparative measurements of ambient atmospheric concentrations of ice nucleating particles using multiple immersion freezing methods and a continuous flow diffusion chamber. *Atmospheric Chemistry and Physics*, **17 (18)**, 11 227–11 245, doi:https://doi.org/10.5194/acp-17-11227-2017.

Engel, A., et al., 2017: The Ocean's Vital Skin: Toward an Integrated Understanding of the Sea Surface Microlayer. *Frontiers in Marine Science*, **4**, 165, doi:10.3389/fmars.2017.00165.

Garcia, E., T. C. J. Hill, A. J. Prenni, P. J. DeMott, G. D. Franc, and S. M. Kreidenweis, 2012: Biogenic ice nuclei in boundary layer air over two U.S. High Plains agricultural regions. *Journal of Geophysical Research: Atmospheres*, **117 (D18)**, doi:10.1029/2012JD018343.

Georgii, H. and E. Kleinjung, 1967: Relations between the chemical composition of atmospheric aerosol particles and the concentration of natural ice nuclei. *Journal de Recherches Atmospheriques*, **1**, 145:156.

Ginoux, P., J. M. Prospero, T. E. Gill, N. C. Hsu, and M. Zhao, 2012: Global-scale attribution of anthropogenic and natural dust sources and their emission rates based on MODIS Deep Blue aerosol products. *Reviews of Geophysics*, **50 (3)**, doi:10.1029/2012RG000388.

Hamilton, D. S., L. A. Lee, K. J. Pringle, C. L. Reddington, D. V. Spracklen, and K. S. Carslaw, 2014: Occurrence of pristine aerosol environments on a polluted planet. *Proceedings of the National Academy of Sciences*, **111 (52)**, 18 466–18 471, doi:10.1073/pnas.1415440111.

Hill, T. C. J., P. J. DeMott, Y. Tobo, J. Fröhlich-Nowoisky, B. F. Moffett, G. D. Franc, and S. M. Kreidenweis, 2016: Sources of organic ice nucleating particles in soils. *Atmospheric Chemistry and Physics*, **16 (11)**, 7195–7211, doi:10.5194/acp-16-7195-2016.

Hill, T. C. J., B. F. Moffett, P. J. DeMott, D. G. Georgakopoulos, W. L. Stump, and G. D. Franc, 2014: Measurement of Ice Nucleation-Active Bacteria on Plants and in Precipitation by Quantitative PCR. *Applied and Environmental Microbiology*, **80 (4)**, 1256–1267, doi:10.1128/AEM.02967-13.

Hiranuma, N., et al., 2015: A comprehensive laboratory study on the immersion freezing behavior of illite NX particles: A comparison of 17 ice nucleation measurement techniques. *Atmospheric Chemistry and Physics*, **15 (5)**, 2489–2518, doi: https://doi.org/10.5194/acp-15-2489-2015.

Hoose, C. and O. Möhler, 2012: Heterogeneous ice nucleation on atmospheric aerosols: A review of results from laboratory experiments. *Atmospheric Chemistry and Physics*, **12 (20)**, 9817–9854, doi:10.5194/acp-12-9817-2012.

Hoppel, W. A., J. W. Fitzgerald, G. M. Frick, R. E. Larson, and E. J. Mack, 1990: Aerosol size distributions and optical properties found in the marine boundary layer over the Atlantic Ocean. *Journal of Geophysical Research: Atmospheres*, **95 (D4)**, 3659–3686, doi: 10.1029/JD095iD04p03659.

Hoppel, W. A., G. M. Frick, J. W. Fitzgerald, and R. E. Larson, 1994: Marine boundary layer measurements of new particle formation and the effects nonprecipitating clouds have on aerosol size distribution. *Journal of Geophysical Research: Atmospheres*, **99 (D7)**, 14 443–14 459, doi:10.1029/94JD00797.

Huang, Y., S. T. Siems, M. J. Manton, A. Protat, and J. Delanoë, 2012: A study on the low-altitude clouds over the Southern Ocean using the DARDAR-MASK. *Journal of Geophysical Research: Atmospheres*, **117 (D18)**, doi:10.1029/2012JD017800.

Humphries, R. S., I. M. McRobert, W. A. Ponsonby, J. P. Ward, M. D. Keywood, Z. M. Loh, P. B. Krummel, and J. Harnwell, 2019: Identification of platform exhaust on the RV *Investigator*.

Atmospheric Measurement Techniques, **12 (6)**, 3019–3038, doi:10.5194/amt-12-3019-2019.

Irish, V. E., et al., 2017: Ice-nucleating particles in Canadian Arctic sea-surface microlayer and bulk seawater. *Atmospheric Chemistry and Physics*, **17 (17)**, 10 583–10 595, doi:https://doi.org/10.5194/acp-17-10583-2017.

Irish, V. E., et al., 2019: Ice nucleating particles in the marine boundary layer in the Canadian Arctic during summer 2014. *Atmospheric Chemistry and Physics*, **19 (2)**, 1027–1039, doi:https://doi.org/10.5194/acp-19-1027-2019.

Jickells, T. D., et al., 2005: Global Iron Connections Between Desert Dust, Ocean Biogeochemistry, and Climate. *Science*, **308 (5718)**, 67–71, doi:10.1126/science.1105959.

Kanji, Z. A. and J. P. D. Abbatt, 2010: Ice nucleation onto Arizona test dust at cirrus temperatures: Effect of temperature and aerosol size on onset relative humidity. *The Journal of Physical Chemistry. A*, **114 (2)**, 935–941, doi:10.1021/jp908661m.

Kanji, Z. A., L. A. Ladino, H. Wex, Y. Boose, M. Burkert-Kohn, D. J. Cziczo, and M. Krämer, 2017: Overview of Ice Nucleating Particles. *Meteorological Monographs*, **58**, 1.1–1.33, doi:10.1175/AMSMONOGRAPHS-D-16-0006.1.

Kiehl, J. T., 2007: Twentieth century climate model response and climate sensitivity. *Geophysical Research Letters*, **34 (22)**, doi:10.1029/2007GL031383.

Kleefeld, C., C. D. O'Dowd, S. O'Reilly, S. G. Jennings, P. Aalto, E. Becker, G. Kunz, and G. de Leeuw, 2002: Relative contribution of submicron and supermicron particles to aerosol light scattering in the marine boundary layer. *Journal of Geophysical Research: Atmospheres*, **107 (D19)**, PAR 8–1–PAR 8–13, doi:10.1029/2000JD000262.

Krishnamoorthy, K. and M. Lee, 2013: New approximate confidence intervals for the difference between two Poisson means and comparison. *Journal of Statistical Computation and Simulation*, **83 (12)**, 2232–2243, doi:10.1080/00949655.2012.686616.

Lewis, E. R. and S. E. Schwartz, 2004: Sea Salt Aerosol Production: Mechanisms, Methods, Measurements and Models—A Critical Review. *Washington DC American Geophysical Union Geophysical Monograph Series*, **152**, doi:10.1029/GM152.

Mace, G. G., 2010: Cloud properties and radiative forcing over the maritime storm tracks of the Southern Ocean and North Atlantic derived from A-Train. *Journal of Geophysical Research: Atmospheres*, **115 (D10)**, doi:10.1029/2009JD012517.

Mamouri, R.-E. and A. Ansmann, 2016: Potential of polarization lidar to provide profiles of CCN- and INP-relevant aerosol parameters. *Atmospheric Chemistry and Physics*, **16 (9)**, 5905–5931, doi:10.5194/acp-16-5905-2016.

Marchand, R., et al., 2014: The Southern Ocean CLouds, Radiation, Aerosol Transport Experimental Study. 40.

Maring, H., D. L. Savoie, M. A. Izaguirre, L. Custals, and J. S. Reid, 2003: Mineral dust aerosol size distribution change during atmospheric transport. *Journal of Geophysical Research: Atmospheres*, **108 (D19)**, doi:10.1029/2002JD002536.

Martel, A. R., 2015: The Detection of Outliers in Nondestructive Integrations with the Generalized Extreme Studentized Deviate Test. *Publications of the Astronomical Society of the Pacific*, **127 (949)**, 258, doi:10.1086/680382.

MATLAB, 2019: *MATLAB Version 9.6.0.1072779 (R2019a)*. The MathWorks Inc., Natick, Massachusetts, USA.

McCluskey, C. S., P. J. DeMott, P.-L. Ma, and S. M. Burrows, 2019: Numerical Representations of Marine Ice-Nucleating Particles in Remote Marine Environments Evaluated Against Observations. *Geophysical Research Letters*, **46 (13)**, 7838–7847, doi:10.1029/2018GL081861.

McCluskey, C. S., et al., 2014: Characteristics of atmospheric ice nucleating particles associated with biomass burning in the US: Prescribed burns and wildfires. *Journal of Geophysical Research: Atmospheres*, **119 (17)**, 10 458–10 470, doi:10.1002/2014JD021980.

McCluskey, C. S., et al., 2018a: Marine and Terrestrial Organic Ice-Nucleating Particles in Pristine Marine to Continentally Influenced Northeast Atlantic Air Masses. *Journal of Geophysical Research: Atmospheres*, **123 (11)**, 6196–6212, doi:10.1029/2017JD028033.

McCluskey, C. S., et al., 2018b: A Mesocosm Double Feature: Insights into the Chemical Makeup of Marine Ice Nucleating Particles. *Journal of the Atmospheric Sciences*, **75 (7)**, 2405–2423,

doi:10.1175/JAS-D-17-0155.1.

McCluskey, C. S., et al., 2018c: Observations of Ice Nucleating Particles Over Southern Ocean Waters. *Geophysical Research Letters*, **45 (21)**, 11,989–11,997, doi:10.1029/2018GL079981.

Möhler, O., P. J. DeMott, G. Vali, and Z. Levin, 2007: Microbiology and atmospheric processes: The role of biological particles in cloud physics. *Biogeosciences*, **4 (6)**, 1059–1071, doi:https://doi.org/10.5194/bg-4-1059-2007.

Morrison, A. E., S. T. Siems, and M. J. Manton, 2011: A Three-Year Climatology of Cloud-Top Phase over the Southern Ocean and North Pacific. *Journal of Climate*, **24 (9)**, 2405–2418, doi:10.1175/2010JCLI3842.1.

Mulcahy, J. P., C. D. O'Dowd, and S. G. Jennings, 2009: Aerosol optical depth in clean marine and continental northeast Atlantic air. *Journal of Geophysical Research*, **114 (D20)**, D20 204, doi:10.1029/2009JD011992.

Niemand, M., et al., 2012: A Particle-Surface-Area-Based Parameterization of Immersion Freezing on Desert Dust Particles. *Journal of the Atmospheric Sciences*, **69 (10)**, 3077–3092, doi:10.1175/JAS-D-11-0249.1.

Noone, K. J., J. A. Ogren, J. Heintzenberg, R. J. Charlson, and D. S. Covert, 1988: Design and Calibration of a Counterflow Virtual Impactor for Sampling of Atmospheric Fog and Cloud Droplets. *Aerosol Science and Technology*, **8 (3)**, 235–244, doi:10.1080/02786828808959186.

O'Dowd, C., et al., 2015: Connecting marine productivity to sea-spray via nanoscale biological processes: Phytoplankton Dance or Death Disco? *Scientific Reports*, **5 (1)**, 1–11, doi:10.1038/srep14883.

O'Dowd, C. D. and G. de Leeuw, 2007: Marine aerosol production: A review of the current knowledge. *Philosophical Transactions of the Royal Society A: Mathematical, Physical and Engineering Sciences*, **365 (1856)**, 1753–1774, doi:10.1098/rsta.2007.2043.

Perring, A. E., et al., 2015: Airborne observations of regional variation in fluorescent aerosol across the United States. *Journal of Geophysical Research: Atmospheres*, **120 (3)**, 1153–1170, doi:10.1002/2014JD022495.

Petters, M. D. and T. P. Wright, 2015: Revisiting ice nucleation from precipitation samples. *Geophysical Research Letters*, **42 (20)**, 8758–8766, doi:10.1002/2015GL065733.

Phillips, V. T. J., P. J. DeMott, and C. Andronache, 2008: An Empirical Parameterization of Heterogeneous Ice Nucleation for Multiple Chemical Species of Aerosol. *Journal of the Atmospheric Sciences*, **65 (9)**, 2757–2783, doi:10.1175/2007JAS2546.1.

Phillips, V. T. J., P. J. Demott, C. Andronache, K. A. Pratt, K. A. Prather, R. Subramanian, and C. Twohy, 2012: Improvements to an Empirical Parameterization of Heterogeneous Ice Nucleation and Its Comparison with Observations. *Journal of the Atmospheric Sciences*, **70 (2)**, 378–409, doi:10.1175/JAS-D-12-080.1.

Pöhlker, C., J. A. Huffman, and U. Pöschl, 2012: Autofluorescence of atmospheric bioaerosols – fluorescent biomolecules and potential interferences. *Atmospheric Measurement Techniques*, **5 (1)**, 37–71, doi:https://doi.org/10.5194/amt-5-37-2012.

Pruppacher, H. R. and J. D. Klett, 2010: *Microphysics of Clouds and Precipitation*. 2d ed., Atmospheric and Oceanographic Sciences Library, Springer Netherlands, doi:10.1007/978-0-306-48100-0.

Pummer, B. G., et al., 2015: Ice nucleation by water-soluble macromolecules. *Atmospheric Chemistry and Physics*, **15 (8)**, 4077–4091, doi:https://doi.org/10.5194/acp-15-4077-2015.

Quinn, P. K. and T. S. Bates, 2011: The case against climate regulation via oceanic phytoplankton sulphur emissions. *Nature*, **480 (7375)**, 51–56, doi:10.1038/nature10580.

Reed, B. E., R. G. Grainger, D. M. Peters, and A. J. A. Smith, 2016: Retrieving the real refractive index of mono- and polydisperse colloids from reflectance near the critical angle. *Optics Express*, **24 (3)**, 1953, doi:10.1364/OE.24.001953.

Richardson, M. S., et al., 2007: Measurements of heterogeneous ice nuclei in the western United States in springtime and their relation to aerosol characteristics. *Journal of Geophysical Research: Atmospheres*, **112 (D2)**, doi:10.1029/2006JD007500.

Rintoul, S. R., 2007: Rapid freshening of Antarctic Bottom Water formed in the Indian and Pacific oceans. *Geophysical Research Letters*, **34 (6)**, doi:10.1029/2006GL028550.

Rogers, D. C., 1988: Development of a continuous flow thermal gradient diffusion chamber for ice nucleation studies. *Atmospheric Research*, **22 (2)**, 149–181, doi: 10.1016/0169-8095(88)90005-1.

Rogers, D. C., P. J. Demott, S. M. Kreidenweis, and Y. Chen, 2001: A Continuous-Flow Diffusion Chamber for Airborne Measurements of Ice Nuclei. *Journal of Atmospheric and Oceanic Technology*, **18**, 17.

Rosenberg, M. and S. R. Rintoul, 2018: RV Investigator Marine Science Cruise IN1801 (CSIRO Voyage Designation IN2018_V01), SR3 Plus Additional Southern Transects, oceanographic field measurements and analysis.

Rosinski, J., P. L. Haagenson, C. T. Nagamoto, and F. Parungo, 1987: Nature of ice-forming nuclei in marine air masses. *Journal of Aerosol Science*, **18 (3)**, 291–309, doi: 10.1016/0021-8502(87)90024-3.

Russell, L. M., L. N. Hawkins, A. A. Frossard, P. K. Quinn, and T. S. Bates, 2010: Carbohydrate-like composition of submicron atmospheric particles and their production from ocean bubble bursting. *Proceedings of the National Academy of Sciences*, **107 (15)**, 6652–6657, doi:10.1073/pnas.0908905107.

Russell, L. M., S. F. Maria, and S. C. B. Myneni, 2002: Mapping organic coatings on atmospheric particles. *Geophysical Research Letters*, **29 (16)**, 26–1–26–4, doi:10.1029/2002GL014874.

Schill, G. P., et al., 2016: Ice-nucleating particle emissions from photochemically aged diesel and biodiesel exhaust. *Geophysical Research Letters*, **43 (10)**, 5524–5531, doi: 10.1002/2016GL069529.

Schmale, J., et al., 2019: Overview of the Antarctic Circumnavigation Expedition: Study of Preindustrial-like Aerosols and Their Climate Effects (ACE-SPACE). *Bulletin of the American Meteorological Society*, **100 (11)**, 2260–2283, doi:10.1175/BAMS-D-18-0187.1.

Schnell, R. C. and G. Vali, 1976: Biogenic Ice Nuclei: Part I. Terrestrial and Marine Sources. *Journal of the Atmospheric Sciences*, **33 (8)**, 1554–1564, doi:10.1175/1520-0469(1976)033<1554:BINPIT>2.0.CO;2.

Seinfeld, J. H. and S. N. Pandis, 2016: *Atmospheric Chemistry and Physics: From Air Pollution to Climate Change*. John Wiley & Sons.

Stith, J. L., et al., 2009: An overview of aircraft observations from the Pacific Dust Experiment campaign. *Journal of Geophysical Research: Atmospheres*, **114 (D5)**, doi: 10.1029/2008JD010924.

Suski, K. J., T. C. J. Hill, E. J. T. Levin, A. Miller, P. J. DeMott, and S. M. Kreidenweis, 2018: Agricultural harvesting emissions of ice-nucleating particles. *Atmospheric Chemistry and Physics*, **18 (18)**, 13 755–13 771, doi:https://doi.org/10.5194/acp-18-13755-2018.

Takahama, S., S. Gilardoni, L. M. Russell, and A. L. D. Kilcoyne, 2007: Classification of multiple types of organic carbon composition in atmospheric particles by scanning

transmission X-ray microscopy analysis. *Atmospheric Environment*, **41 (40)**, 9435–9451, doi:10.1016/j.atmosenv.2007.08.051.

Tan, I., T. Storelvmo, and M. D. Zelinka, 2016: Observational constraints on mixed-phase clouds imply higher climate sensitivity. *Science*, **352 (6282)**, 224–227, doi:10.1126/science.aad5300.

Tang, I. N., A. C. Tridico, and K. H. Fung, 1997: Thermodynamic and optical properties of sea salt aerosols. *Journal of Geophysical Research: Atmospheres*, **102 (D19)**, 23 269–23 275, doi:10.1029/97JD01806.

Tobo, Y., et al., 2013: Biological aerosol particles as a key determinant of ice nuclei populations in a forest ecosystem. *Journal of Geophysical Research: Atmospheres*, **118 (17)**, 10,100–10,110, doi:10.1002/jgrd.50801.

Trenberth, K. E. and J. T. Fasullo, 2010: Simulation of Present-Day and Twenty-First-Century Energy Budgets of the Southern Oceans. *Journal of Climate*, **23 (2)**, 440–454, doi:10.1175/2009JCLI3152.1.

Twohy, C. H., et al., 2010: Relationships of Biomass-Burning Aerosols to Ice in Orographic Wave Clouds. *Journal of the Atmospheric Sciences*, **67 (8)**, 2437–2450, doi:10.1175/2010JAS3310.1.

Twohy, C. H., et al., 2016: Abundance of fluorescent biological aerosol particles at temperaturesconducive to the formation of mixed-phase and cirrus clouds. *Atmospheric Chemistry and Physics*, **16 (13)**, 8205–8225, doi:10.5194/acp-16-8205-2016.

Uetake, J., T. C. J. Hill, K. A. Moore, P. J. DeMott, A. Protat, and S. M. Kreidenweis, 2020: Airborne bacteria confirm the pristine nature of the Southern Ocean boundary layer. *Submitted for publication*.

Ullrich, R., et al., 2017: A New Ice Nucleation Active Site Parameterization for Desert Dust and Soot. *Journal of the Atmospheric Sciences*, **74 (3)**, 699–717, doi:10.1175/JAS-D-16-0074.1.

Vali, G., 1971: Quantitative Evaluation of Experimental Results an the Heterogeneous Freezing Nucleation of Supercooled Liquids. *Journal of the Atmospheric Sciences*, **28 (3)**, 402–409, doi:10.1175/1520-0469(1971)028<0402:QEOERA>2.0.CO;2.

Vali, G., 1994: Freezing Rate Due to Heterogeneous Nucleation. *Journal of the Atmospheric Sciences*, **51 (13)**, 1843–1856, doi:10.1175/1520-0469(1994)051<1843:FRDTHN>2.0.CO;2.

van Pinxteren, M., S. Barthel, K. W. Fomba, K. Müller, W. von Tümpling, and H. Herrmann, 2017: The influence of environmental drivers on the enrichment of organic carbon in the sea surface microlayer and in submicron aerosol particles – measurements from the Atlantic Ocean. *Elem Sci Anth*, **5 (0)**, 35, doi:10.1525/elementa.225.

Vergara-Temprado, J., et al., 2017: Contribution of feldspar and marine organic aerosols to global ice nucleating particle concentrations. *Atmospheric Chemistry and Physics*, **17 (5)**, 3637–3658, doi:https://doi.org/10.5194/acp-17-3637-2017.

Vergara-Temprado, J., et al., 2018: Strong control of Southern Ocean cloud reflectivity by ice-nucleating particles. *Proceedings of the National Academy of Sciences*, **115 (11)**, 2687–2692,

doi:10.1073/pnas.1721627115.

von der Weiden, S.-L., F. Drewnick, and S. Borrmann, 2009: Particle Loss Calculator – a new software tool for the assessment of the performance of aerosol inlet systems. *Atmospheric Measurement Techniques*, **2 (2)**, 479–494, doi:https://doi.org/10.5194/amt-2-479-2009.

Wang, X., et al., 2015: Microbial Control of Sea Spray Aerosol Composition: A Tale of Two Blooms. *ACS Central Science*, **1 (3)**, 124–131, doi:10.1021/acscentsci.5b00148.

Wilson, T. W., et al., 2015: A marine biogenic source of atmospheric ice-nucleating particles. *Nature*, **525 (7568)**, 234–238, doi:10.1038/nature14986.

Zelenyuk, A., D. Imre, L. A. Cuadra-Rodriguez, and B. Ellison, 2007: Measurements and interpretation of the effect of a soluble organic surfactant on the density, shape and water uptake of hygroscopic particles. *Journal of Aerosol Science*, **38 (9)**, 903–923, doi:10.1016/j.jaerosci.2007.06.006.

Zieger, P., et al., 2017: Revising the hygroscopicity of inorganic sea salt particles. *Nature Communications*, **8 (1)**, 15 883, doi:10.1038/ncomms15883.